

POLITECNICO DI MILANO

Scuola di Ingegneria Industriale e dell'Informazione

**CORSO DI LAUREA MAGISTRALE IN INGEGNERIA
AERONAUTICA**



**Analytical study of the fully developed
spin of light aircraft exploiting preliminary
flight test data**

Relatore: Prof. Lorenzo Trainelli
Correlatore: Ing. Paolo Mezzanotte

Tesi di laurea di:
Riccardo Esposito
matr. 819598

Anno Accademico 2017-2018

Ringrazio il Professor Lorenzo Trainelli per aver stimolato il mio interesse per l'argomento e per la fiducia che mi ha dimostrato.

Ringrazio l'Ing. Paolo Mezzanotte per avermi seguito e consigliato egregiamente durante tutto il lavoro di tesi.

Ringrazio l'Ing. Luciano Belviso, l'Ing. Giuseppe Verde e Blackshape per avermi dato la possibilità di fare la prima esperienza in azienda.

Ringrazio l'Ing. Ernesto Valtorta per aver condiviso con me parte della sua grande conoscenza in materia.

Ringrazio la nonna per avermi ospitato e coccolato con amorevole dedizione e i miei genitori per avermi sostenuto in tutti questi anni di studi.

Infine ringrazio Biagio il rosso, Biagino, Umberto e Simone che con la loro amicizia hanno reso indimenticabile tutto il periodo di tirocinio.

Abstract

In the present thesis will be illustrated the work that was done as part of an internship program in order to predict the spin performance of two light general-aviation airplanes at different advancement in the design process.

The first part is dedicated to the application of two semi-empirical methods for spin prediction to an aircraft in early stage of design. The methods are based only on the geometric and inertial characteristics of the aircraft and their scope is to provide an estimation of the expected spin performance along with some guidelines for tail design.

The large majority of the work is oriented towards the realization of an analytical flight dynamic model and its implementation in a computer program capable of performing numerical simulations of the complete spin maneuver. The simulation program that was realized is based on the numerical integration of the equation of motion in six degrees of freedom that describe the dynamics of the aircraft. Great attention was given to the determination of a complete aerodynamic data-set up to high angles of attack, exploiting the results of flight tests of an aircraft for which a flying prototype was already developed. Through many numerical simulations it was possible to obtain a prediction of the aircraft performance in a developed spin and to verify compliance with the certification requirements prior to further flight tests. Additionally it was conducted a parametric study to be able to assess the effects of different control inputs and flight conditions on the most significant quantities that characterize the spin.

Keywords: Spin, Analytical Model, High Angle of Attack, Numerical Simulation, Flight Dynamics, Flight Test, Aerodynamic Data-Set, Semi-Empirical Methods.

Contents

List of symbols	xi
List of figures	xvii
List of tables	xxiii
1 Introduction	1
1.1 Structure of the work and applicable literature.....	1
1.2 Description of the spin phenomenon and classification	4
2 Description of the airplanes.....	9
2.1 BK115 general description	9
2.2 BK180 general description	12
3 Semi-empirical methods	15
3.1 Aircraft configurations	16
3.1.1 Load conditions	16
3.1.2 Tail design configurations	17
3.2 NACA-Bowman criterion	21
3.2.1 Main factors	22
3.2.2 Tail-damping power factor.....	23
3.2.3 Application of the criterion	27
3.2.4 Ventral strake	28
3.2.5 Anti-spin fillets.....	29
3.2.6 Comparison with the BK115.....	33
3.2.7 Discussion of the results.....	34
3.3 Kerr criterion.....	35
3.3.1 Description	35
3.3.2 Procedure.....	36
3.3.3 Application of the criterion	40
3.3.4 Ventral strake	43

3.3.5	Anti-spin fillets.....	45
3.3.6	Comparison with the BK115.....	46
3.3.7	Discussion of the results.....	47
3.4	Concluding remarks on the semi-empirical methods	47
4	Analytical spin model.....	49
4.1	Equations of motion	49
4.1.1	Conventions.....	49
4.1.2	Kinematic relations	51
4.1.3	Six degrees of freedom equations of motion.....	53
4.2	Numerical integration of the equations of motion	55
5	Aerodynamic data-set	59
5.1	Low angle of attack aerodynamic data	59
5.1.1	Aerodynamic data from flight tests.....	60
5.1.2	Aerodynamic data using the DATCOM method.....	69
5.1.3	Summary low angle of attack aerodynamic coefficients	72
5.2	High angle of attack aerodynamic data	73
5.2.1	Flight test data and simulations.....	74
5.3	Model validation.....	80
5.4	Spin susceptibility criteria	85
6	Simulations.....	89
6.1	Comparison with the dynamically scaled model.....	89
6.2	Spin maneuver prediction	95
7	Parametric study	103
7.1	Stalls	104
7.1.1	Wings level stall.....	104
7.1.2	Turning flight stall.....	106
7.1.3	Accelerated turning stall.....	108
7.2	Spins	110
7.2.1	Incipient spin.....	111
7.2.2	Developed spin.....	113
7.2.3	Fully developed spin	115

7.3 Recovery procedures.....	118
7.3.1 Standard recovery.....	118
7.3.2 Modified recovery.....	120
7.3.3 Neutral recovery.....	122
7.4 Other parameters.....	124
7.4.1 Increased weight.....	124
7.4.2 Increased yawing moment of inertia.....	127
7.4.3 Lower altitude.....	129
8 Conclusions.....	131
8.1 Discussion of the results of the simulations.....	132
References.....	135

List of symbols

Roman symbols

b	Wing span	[m]
b_a	Aileron span	[m]
b_r	Rudder span	[m]
b_s	Ventral strake span	[m]
b_t	Horizontal tail span	[m]
b_v	Vertical tail span	[m]
\bar{c}	Mean aerodynamic chord	[m]
c_a	Aileron mean chord	[m]
c_e	Elevator mean chord	[m]
C_{l_p}	Derivative of rolling-moment coeff. with respect to roll rate	[1/rad]
C_{l_q}	Derivative of rolling-moment coeff. with respect to pitch rate	[1/rad]
$C_{l_{tot}}$	Total moment coefficient about the x axis	[-]
C_{l_β}	Rolling-moment coefficient due to sideslip angle	[1/rad]
$C_{l_{\delta_a}}$	Rolling-moment coefficient due to aileron deflection	[1/rad]
$C_{l_{\delta_r}}$	Rolling-moment coefficient due to rudder deflection	[1/rad]
C_L	Aircraft lift coefficient	[-]
C_{L0}	Lift coefficient for zero angle of attack	[-]
$C_{L_{eq}}$	Equilibrium lift coefficient	[-]
C_{L_t}	Lift coefficient of the horizontal tail	[-]
C_{L_α}	Lift curve slope	[1/rad]
$C_{L_{\delta_e}}$	Lift coefficient due to elevator deflection	[1/rad]
C_{m0}	Pitching moment coefficient for zero angle of attack	[-]
C_m	Pitching-moment coefficient	[-]
C_{m_q}	Derivative of pitching-moment coeff. with respect to pitch rate	[1/rad]
$C_{m_{tot}}$	Total moment coefficient about the y axis	[-]
C_{m_α}	Pitching-moment derivative with respect to angle of attack	[1/rad]

$C_{m\delta_e}$	Pitching-moment coefficient due to elevator deflection	[1/rad]
C_{np}	Derivative of yawing-moment coeff. with respect to roll rate	[1/rad]
C_{nr}	Derivative of yawing-moment coeff. with respect to yaw rate	[1/rad]
C_{ntot}	Total moment coefficient about the z axis	[-]
$C_{n\beta}$	Yawing-moment coefficient due to sideslip angle	[1/rad]
$C_{n\beta_{dyn}}$	Directional stability parameter	[1/°]
$C_{n\delta_a}$	Yawing-moment coefficient due to aileron deflection	[1/rad]
$C_{n\delta_r}$	Yawing-moment coefficient due to rudder deflection	[1/rad]
c_r	Rudder mean chord	[m]
c_{root}	Wing root chord	[m]
\bar{c}_t	Horizontal tail mean aerodynamic chord	[m]
c_{tip}	Wing tip chord	[m]
\bar{c}_v	Vertical tail mean aerodynamic chord	[m]
c_{vroot}	Vertical tail root chord	[m]
c_{vtip}	Vertical tail tip chord	[m]
C_x	Longitudinal force coefficient	[-]
C_{xtot}	Total force coefficient along the x axis	[-]
$C_{x\delta_e}$	Longitudinal force coefficient due to elevator deflection	[1/rad]
C_{yp}	Derivative of side force coefficient with respect to roll rate	[1/rad]
C_{yr}	Derivative of side force coefficient with respect to yaw rate	[1/rad]
C_{ytot}	Total force coefficient along the y axis	[-]
$C_{y\beta}$	Side force coefficient due to sideslip angle	[1/rad]
$C_{y\delta_a}$	Side force coefficient due to aileron deflection	[1/rad]
$C_{y\delta_r}$	Side force coefficient due to rudder deflection	[1/rad]
C_z	Normal force coefficient	[-]
C_{ztot}	Total force coefficient along the z axis	[-]
$C_{z\delta_e}$	Normal force coefficient due to elevator deflection	[1/rad]
d	Distance of the axis of thrust from the x body axis	[m]
F_x	Total force acting along x body axis	[N]
F_{xA}	Aerodynamic force acting along x body axis	[N]

F_y	Total force acting along y body axis	[N]
F_{yA}	Aerodynamic force acting along y body axis	[N]
F_z	Total force acting along z body axis	[N]
F_{zA}	Aerodynamic force acting along z body axis	[N]
g	Acceleration of gravity	[m/s ²]
h	Height of fuselage sections	[m]
h_{\max}	Fuselage maximum height	[m]
I_x	Rolling moment of inertia	[kgm ²]
I_{xz}	Product of inertia in the xz plane	[kgm ²]
I_y	Pitching moment of inertia	[kgm ²]
I_z	Yawing moment of inertia	[kgm ²]
J_m	Moment of inertia of the propeller	[kgm ²]
l_1	Distance of the nose of the aircraft from CG	[m]
l_2	Distance of the tail of the aircraft from CG	[m]
l_f	Fuselage length	[m]
l_r	Distance of centroid of S_R from CG	[m]
l_s	Ventral strake arm	[m]
l_t	Horizontal tail arm	[m]
l_v	Vertical tail arm	[m]
L_1	Distance of centroid of S_{R1} from CG	[m]
L_2	Distance of centroid of S_{R2} from CG	[m]
L_F	Distance of centroid of S_F from CG	[m]
\bar{l}_{pb}	Body damping coefficient	[-]
\bar{l}_{pw}	Wing rolling moment coefficient	[-]
\bar{l}_ζ	Anti-spin moment coefficient due to rudder deflection	[-]
m	Mass of the aircraft	[kg]
M_x	Rolling moment about the x body axis	[Nm]
M_{xA}	Aerodynamic moment about the x body axis	[Nm]
M_y	Pitching moment about the y body axis	[Nm]
M_{yA}	Aerodynamic moment about the y body axis	[Nm]
M_{yG}	Gyroscopic moment about the y body axis	[Nm]

M_z	Yawing moment about the z body axis	[Nm]
M_{zA}	Aerodynamic moment about the z body axis	[Nm]
M_{zG}	Gyroscopic moment about the z body axis	[Nm]
n_z	Load factor	[-]
p	Roll rate	[rad/s]
q	Pitch rate	[rad/s]
r	Yaw rate	[rad/s]
R	Spin radius	[m]
S	Wing area	[m ²]
S_a	Aileron area	[m ²]
S_B	Fuselage side area	[m ²]
S_e	Elevator area	[m ²]
S_F	Fuselage side area below horizontal tail	[m ²]
$S_{f_{ave}}$	Fuselage mean cross-section area	[m ²]
S_h	Horizontal tail area	[m ²]
S_r	Rudder area	[m ²]
S_R	Unshielded rudder area	[m ²]
S_{R1}	Unshielded rudder area above horizontal tail	[m ²]
S_{R2}	Unshielded rudder area below horizontal tail	[m ²]
S_s	Ventral strake area	[m ²]
S_v	Vertical tail area	[m ²]
t	Time	[s]
t/c	Wing thickness-chord ratio	[-]
T	Thrust of the engine	[N]
T_{fb}	Rotation matrix from fixed to body frame	[-]
u	Velocity component along the x body axis	[m/s]
v	Velocity component along the y body axis	[m/s]
V	Flight velocity	[m/s]
\bar{V}	Tail volume coefficient	[-]
V_D	Velocity of descent	[m/s]
V_{EAS}	Equivalent air-speed	[m/s]
V_{eq}	Flight velocity for longitudinal equilibrium	[m/s]

V_s	Stall speed	[m/s]
V_{TAS}	True air-speed	[m/s]
w	Velocity component along the z body axis	[m/s]
w_{max}	Fuselage maximum width	[m]
x_{AC}	Longitudinal position of the aerodynamic center in % MAC	[-]
x_{CG}	Longitudinal position of the CG in % MAC	[-]
X, Y, Z	Coordinates of the CG in the fixed reference frame	[m]
x	Longitudinal body axis	[m]
y	Lateral body axis	[m]
z	Vertical body axis	[m]
Z_s	Distance from strake center of pressure to fuselage axis	[m]
Z_v	Distance from VT center of pressure to fuselage axis	[m]

Greek symbols

α	Angle of attack	[°, rad]
α_{eq}	Angle of attack for longitudinal equilibrium	[°, rad]
α_s	Stall angle of attack	[°, rad]
α_t	Angle of attack of the horizontal tail	[°, rad]
β	Sideslip angle	[°, rad]
γ	Helix angle	[°, rad]
Γ	Dihedral angle	[°]
δ_a	Aileron deflection	[°, rad]
δ_e	Elevator deflection	[°, rad]
δ_{eq}	Elevator deflection for longitudinal equilibrium	[°, rad]
δ_r	Rudder deflection	[°, rad]
ε	Body damping coefficient	[-]
ε_t	Wing twist angle	[°]
θ_y	Wing tilt angle	[°, rad]
θ	Pitch angle	[°, rad]
λ	Non-dimensional rotation rate	[-]

$\Lambda_{c/2}$	Sweep angle at $\frac{1}{2} c$	[°]
$\Lambda_{c/4}$	Sweep angle at $\frac{1}{4} c$	[°]
μ	Relative density factor	[-]
ρ	Air density	
	[kg/m ³]	
ϕ	Bank angle	[°, rad]
ψ	Heading angle	[°, rad]
ω_m	Angular velocity of the propeller	[rad/s]
Ω	Spin rate of rotation	[rad/s]

Abbreviations

AR	Aspect ratio
AR _t	Horizontal tail aspect ratio
AR _v	Vertical tail aspect ratio
CAS	Calibrated airspeed
CG	Center of gravity
HT	Horizontal tail
IYMP	Inertia yawing moment parameter
LCDP	Lateral control departure parameter
MAC	Mean aerodynamic chord
TAS	True airspeed
TDPF	Tail-damping power factor
TDR	Tail-damping ratio
URMC	Unshielded rudder moment coefficient
URVC	Unshielded rudder volume coefficient
VT	Vertical tail

List of figures

Figure 1.1: Schematic illustration of a spin and the equilibrium of forces7

Figure 1.2: Condition of autorotation due to the stalled wing8

Figure 1.3: Aerodynamic and inertia moments in the spin equilibrium.....8

Figure 2.1: BK115 three-view..... 11

Figure 2.2: BK180 three-view..... 14

Figure 3.1: CG envelope and the 3 load case conditions considered.....17

Figure 3.2: Clean configuration tail design and area below the horizontal tail18

Figure 3.3: Ventral strake designs.....19

Figure 3.4: Anti-spin fillets20

Figure 3.5: Extended effective area below the horizontal tail due to the presence of anti-spin fillets21

Figure 3.6: Fixed area below the horizontal tail and its distance to the center of gravity24

Figure 3.7: Unshielded rudder area and its distance from the center of gravity for two different values of angle of attack25

Figure 3.8: Spin recovery requirements for airplanes of relative density of 15 or less ..26

Figure 3.9: NACA criterion for spin recovery for aircraft of relative density between 6 and 3526

Figure 3.10: Horizontal tail wake shielding the entire surface of the rudder.....28

Figure 3.11: Unshielded rudder area and its centroid for wake boundaries at 45° and 15°30

Figure 3.12: NACA spin recovery requirements for two configurations with fillets and strakes.....32

Figure 3.13: NACA method, comparison between the results for the BK180 and the BK11533

Figure 3.14: The criterion for the prediction of recovery characteristics of a spinning aircraft36

Figure 3.15: Values of body damping coefficient for different portions of the vertical tail surface	37
Figure 3.16: Dimensions needed for the calculation of the body rolling moment coefficient.....	38
Figure 3.17: Unshielded rudder area and distance from the center of gravity	39
Figure 3.18: Estimation of wing rolling moment coefficient.....	39
Figure 3.19: Height of fuselage sections and their distance from the CG at 28%	40
Figure 3.20: Shielded and unshielded areas of fin and rudder	41
Figure 3.21: Unbalanced rolling moment coefficient for the clean configuration.....	42
Figure 3.22: Kerr criterion with the addition of ventral strakes, comparison with the clean configuration.....	44
Figure 3.23: Kerr criterion with the addition of anti-spin fillets.....	45
Figure 3.24: Kerr criterion, comparison between the BK180 and the BK115.....	46
Figure 4.1: Body axes and sign conventions used	50
Figure 4.2: Euler angles and sequence of rotation	52
Figure 4.3: Angle of attack and sideslip angle	57
Figure 5.1: Graph of equilibrium lift coefficient against elevator deflection for two positions of center of gravity.....	62
Figure 5.2: Determination of the position of the aerodynamic center	63
Figure 5.3: Trim curve for CG 18.2%. Comparison between experimental data and theoretical calculation	66
Figure 5.4: Trim curve for CG 30%. Comparison between experimental data and theoretical calculation	67
Figure 5.5: Example of aerodynamic coefficients curves up to high α [19].....	74
Figure 5.6: Time histories of controls deflection, spin 1	75
Figure 5.7: Time histories of aircraft attitudes, spin 1	75
Figure 5.8: Time history of angle of attack, spin 1	76
Figure 5.9: Time history of flight speed, spin 1	76
Figure 5.10: Control deflection inputs used in the simulation, comparison with the time histories from flight test, spin 1	77
Figure 5.11: Bank angle, comparison between flight test and simulation output.....	78
Figure 5.12: Elevation angle, comparison between flight test and simulation output	78

Figure 5.13: Azimuth angle, comparison between flight test and simulation output.....	78
Figure 5.14: Angle of attack, comparison between flight test and simulation output.....	79
Figure 5.15: Load factor, comparison between flight test and simulation output.....	79
Figure 5.16: Flight speed, comparison between flight test and simulation output.....	79
Figure 5.17: Control deflection, comparison between flight test and simulation input, spin 2	80
Figure 5.18: Aircraft attitudes, comparison between flight test and simulation output, spin 2	81
Figure 5.19: Angle of attack, comparison between flight test and simulation output, spin 2.....	81
Figure 5.20: Load factor, comparison between flight test and simulation output, spin 2	82
Figure 5.21: Flight speed, comparison between flight test and simulation output, spin 2	82
Figure 5.22: Control deflection, comparison between flight test and simulation input, spin 3	83
Figure 5.23: Aircraft attitudes, comparison between flight test and simulation output, spin 3	83
Figure 5.24: Angle of attack, comparison between flight test and simulation output, spin 3	84
Figure 5.25: Load factor, comparison between flight test and simulation output, spin 3	84
Figure 5.26: Flight speed, comparison between flight test and simulation output, spin 3	84
Figure 5.27: Directional stability parameter	86
Figure 5.28: Lateral control departure parameter.....	87
Figure 5.29: Bihrlé - Weissman chart	88
Figure 6.1: Bank angle, comparison between scaled model and simulation.....	90
Figure 6.2: Elevation angle, comparison between scaled model and simulation.....	90
Figure 6.3: Azimuth angle, comparison between scaled model and simulation	91
Figure 6.4: Roll rate, comparison between scaled model and simulation.....	91
Figure 6.5: Pitch rate, comparison between scaled model and simulation	91

Figure 6.6: Yaw rate, comparison between scaled model and simulation	92
Figure 6.7: Non-dimensional spin rate of rotation, comparison between scaled model and simulation	92
Figure 6.8: Flight speed, comparison between scaled model and simulation	92
Figure 6.9: Altitude loss, comparison between scaled model and simulation	93
Figure 6.10: The spin maneuver, graphic comparison between the simulation (left) and the scaled model (right, extracted from video files).....	94
Figure 6.11: Controls deflection, inputs for the simulation	95
Figure 6.12: Bank angle, simulated prediction	96
Figure 6.13: Elevation angle, simulated prediction.....	96
Figure 6.14: Azimuth angle, simulated prediction.....	97
Figure 6.15: Roll rate, simulated prediction.....	97
Figure 6.16: Pitch rate, simulated prediction	98
Figure 6.17: Yaw rate, simulated prediction	98
Figure 6.18: Angle of attack, simulated prediction.....	99
Figure 6.19: Angle of sideslip, simulated prediction	99
Figure 6.20: Equivalent air speed speed, simulated prediction.....	100
Figure 6.21: Spin rate of rotation, simulated prediction	100
Figure 6.22: Non-dimensional spin rate of rotation, simulated prediction	100
Figure 6.23: Load factor, simulated prediction	101
Figure 6.24: Altitude, simulated prediction	101
Figure 7.1: Time histories for simulated wing level stall.....	105
Figure 7.2: Time histories for simulated turning flight stall	107
Figure 7.3: Simulated time histories of accelerated turning stall.....	109
Figure 7.4: Time histories of the simulated incipient spin.....	112
Figure 7.5: Time histories of the simulated developed spin	114
Figure 7.6: Time histories of the simulated fully developed spin.....	117
Figure 7.7: Time histories of the Standard recovery procedure.....	119
Figure 7.8: Time histories of the Modified recovery procedure	121
Figure 7.9: Time histories of the Neutral recovery procedure	123
Figure 7.10: Time histories of the spin maneuver with increased weight.....	126

Figure 7.11: Time histories of the spin maneuver with increased yawing moment of inertia.....	128
Figure 7.12: Time histories of the spin maneuver at lower altitude.....	130

List of tables

Table 2.1: BK115 geometric characteristics	10
Table 2.2: BK115 structural and aerodynamic limitations	10
Table 2.3: BK180 geometric characteristics	12
Table 2.4: BK180 structural and aerodynamic limitations	13
Table 3.1: Load case conditions considered for the semi-empirical methods	16
Table 3.2: Area below horizontal tail for clean configuration and distance from CG	18
Table 3.3: Ventral strakes surface areas.....	19
Table 3.4: Total effective area below the horizontal tail with anti-spin fillets	20
Table 3.5: Fixed area below the horizontal tail for the clean configuration	27
Table 3.6: Fixed area below the horizontal tail for the configuration with the ventral strake	28
Table 3.7: Fixed area below the horizontal tail and fillets for the three configurations .	29
Table 3.8: Tail-damping ratio with the anti-spin fillets	30
Table 3.9: Unshielded rudder area and its distance from the center of gravity.....	31
Table 3.10: Values of tail-damping power factor for the two configurations with strake and fillets.....	31
Table 3.11: Values of body damping coefficient for different cross-sections of the fuselage	37
Table 3.12: Area and distance from CG of vertical tail sections	40
Table 3.13: Anti-spin moment coefficient and unbalanced rolling moment coefficient with anti-spin fillets.....	45
Table 4.1: Sign conventions for the controls deflection.....	50
Table 5.1: Source of the aerodynamic derivatives at low angle of attack.....	60
Table 5.2: Trimmed flight experimental data 1.....	60
Table 5.3: Trimmed flight experimental data 2.....	61
Table 5.4: Slope of the interpolating curve $C_{Leq} - \delta_{eq}$	61
Table 5.5: Aerodynamic derivatives in the longitudinal plane for CG at 18.2% MAC..	66
Table 5.6: Stabilized sideslip and rudder deflection from flight tests.....	68

Table 5.7: Stabilized roll rates from flight tests	69
Table 5.8: Wing geometric data used with the DATCOM method	70
Table 5.9: Horizontal tail geometric data used with the DATCOM method	70
Table 5.10: Vertical tail geometric data used with the DATCOM method	71
Table 5.11: Fuselage geometric data used with the DATCOM method	71
Table 5.12: Ventral strake geometric data used with the DATCOM method.....	71
Table 5.13: Low α aerodynamic derivatives for CG at 25% MAC	72
Table 5.14: Inertial properties of the aircraft used in the simulations.....	77
Table 7.1: Significant values for the incipient spin simulation.....	111
Table 7.2: Significant values for the developed spin simulation	113
Table 7.3: Significant values for the fully developed spin simulation.....	116
Table 7.4: Significant values for the Standard recovery procedure	119
Table 7.5: Significant values for the Modified recovery procedure	120
Table 7.6: Significant values for the Neutral recovery procedure	122
Table 7.7: Significant values for the spin maneuver with increased weight.....	125
Table 7.8: Significant values for the spin maneuver with increased yawing moment of inertia.....	127
Table 7.9: Significant values for the spin maneuver at lower altitude.....	129

1 Introduction

Since the beginning of aviation history the spin has been the cause of many accidents in all categories of aircraft of either civil aviation or military. For this reason it is of great importance to study this phenomenon in order to predict the behavior of an airplane in a spin and guarantee a safe recovery from it.

In the present work will be illustrated and applied some of the many spin prediction techniques as part of a work of internship in Balckshape s.p.a., one of the leading Italian manufacturers of light full-composite aircraft.

The main focus of the work has been directed towards the implementation of a simulation program based on the numerical integration of the equations of motion in six degrees of freedom capable of predicting the behavior of the aircraft in a fully developed spin. One of the major advantages of the utilization the simulation program is the possibility to simulate the effects of many different parameters on the entire spin maneuver, such as different weight configurations and moments of inertia as well as different spin entry and recovery maneuvers.

The first part of the work was dedicated to the application of two semi-empirical methods for a preliminary assessment of the spin characteristics and the effectiveness of the tail design in the recovery procedure for different load conditions.

1.1 Structure of the work and applicable literature

In Chapter 2 are described the main characteristics of the two aircraft that were studied during the course of the thesis work. The BK115, for which a flying prototype and many flight tests were available, was taken as reference in the development of the analytical spin model and in particular for the determination of the aerodynamic data-set needed for the simulation program. The BK180, which is a heavier and more powerful version of the BK115 with a different tail design, is still under development and was the subject for the application of the semi-empirical methods based on its geometrical characteristics and load configurations.

The first part of the work, shown in Chapter 3, is dedicated to the semi-empirical methods. The NACA method, explained in Reference [11], was developed based on the results of the tests on approximately 100 free-spinning models in the NACA

vertical wind tunnel. The aim was to define the tail design requirements that would produce a satisfactory spin recovery based on the relative distribution of mass along the wing and fuselage and the relative density of the aircraft with respect to the air. In Reference [6] the same method is extended to light general-aviation aircraft with the addition of some improvements that take into account the effects of a steeper spin on the wake produced by the horizontal tail. In the same paper are also described the factors that were considered of greatest importance in the spin behavior, as well as the effects of different load distributions on the recommended recovery procedure.

The second of the semi-empirical methods, denominated Kerr criterion, is described in Reference [7]. The paper, published by the Royal Aircraft Establishment, identifies another set of parameters that affects the most the spin and spin recovery characteristics of an aircraft. The method is based on many spin tests performed on different full-scale airplanes in order to define a simple spin prediction criterion based only on the inertial and geometric characteristics. Differently from the previous method, the Kerr criterion takes into account the anti-spin effect of the fuselage side area, and the pro-spin-effect of the wing, while it does not considers the relative density of the aircraft with respect to the air.

Based on the first results of the application of the two methods to the BK180, it was considered the possibility of improving the predicted outcome by the employment of additional tail surfaces, namely a ventral fin (or strake) and leading edge extensions for the horizontal tail (fillets). The effect produced by these additional surfaces on the spin is described in Reference [6] and analyzed in further detail in Reference [10] for the application with the NACA method. The same principles were also extended to the application of the Kerr criterion in order to obtain comparable results.

The results obtained by the two methods for the BK180 were also compared with the results produced by the application of the same methods to the BK115 for which there is already some knowledge of the spin characteristics.

In Chapter 4 is explained the first part in the development of the computer simulation program for the spin prediction. The chapter is dedicated to the definition of equations of motion in six degrees of freedom that describe the movement of a rigid body in space. This set of equation can be found in most flight mechanics textbooks and for the present work were taken from Reference [13] and Reference [14].

Two reference frames are defined, one is fixed and the other one moves in space with the body. Six kinematic relations describe the position and rotation of the body frame with respect to the fixed one. Six additional equations define the forces and moments acting on the body that produce angular and linear accelerations. These last six equations are then specialized for the aircraft by the definition of aerodynamic forces and moments as well as the gyroscopic moments produced by the propeller.

By rearranging all the twelve equations it is possible to obtain a complete set of differential equation that will be integrated numerically by the simulation software.

An example of the final set of equations is reported in Reference [16] and Reference [18].

Chapter 5 describes the procedure that was adopted in order to obtain a complete aerodynamic data set of the aircraft BK115 to be employed in the simulation program. The difficulty of such task is mainly due to the necessity to extend the values of aerodynamic coefficients to the non-linear region beyond the stall angle of attack. Conventionally the data set is obtained in wind tunnel tests with the use of a rotary balance [20].

For the present work it was identified a linear data set based on the results of flight tests on the full scale BK115 prototype. However it was not possible to determine experimentally all the aerodynamic coefficients and for this reason part of the aerodynamic data was calculated by means of a simplified DATCOM method that can be obtained from Reference [12] and Reference [13].

Due to the impossibility to employ a wind tunnel facility, the non-linear part of the aerodynamic data set was estimated by first gathering complete data sets belonging to other aircrafts with traditional wing and tail geometry, mainly the Aermacchi MB339 and the Hongdu JL-8. By applying similar trends of the coefficients from the gathered data to the linear derivatives of the BK115 it was possible to extend the aerodynamic data set to the non-linear region. By comparing the simulation outputs with the time histories of the flight tests and applying minor changes to the coefficients in an iterative process, it was possible to obtain an estimation of the complete aerodynamic data set for the BK115. An example of the graphs of a complete aerodynamic set for another aircraft can be found in Reference [19].

Once the process of estimation of the aerodynamic characteristics of the aircraft was completed, the computer program was finalized and ready to be used in the simulations for spin behavior prediction.

The first simulations of the spin maneuver beyond the first turn are described in Chapter 6. In the first part is shown a comparison between the experimental data from spin tests performed on a dynamically scaled model of the BK115 and the time histories as output of the simulation program. The experimental data was already available since the spin tests on the model were completed in 2016 and the comparison with the simulation outputs gave confirmation of the good approximation of the overall maneuver that can be obtained from the numerical simulations.

In the second part of the chapter is illustrated the six turns spin simulation that the aircraft would need to be able to perform in order to be compliant with the spin requirements of the CS-23 certification under the ‘Aerobatic’ category [24]. From the time histories can be identified all the phases of the spin, from the stall and spin entry to the developed spin phase and finally the recovery maneuver. Many variables were plotted from which can be obtained the most important factors that characterize the

spin, such as the altitude lost throughout the entire maneuver, the stabilized angle of attack, the rate of rotation, the air speed and the load factor.

Chapter 7 is dedicated to a more in depth analysis of the spin maneuver and the evaluation of the effects of different parameters on the overall performance.

First were simulated the stall maneuvers as required by CS-23 [24] in order to assess whether departure from controlled flight would occur, which would possibly lead to an accidental spin entry. Increasingly more critical maneuvers were tested from the wing level stall to the accelerated turning stall without any signs of lateral or directional instability.

The spin tests were performed for increasing number of turns from 1 to 6 to be able to better understand the characteristics of the spin phases from incipient to fully developed, and to confirm the ability to safely recover from any point in the spin. Similar test procedures can be found in Reference [22]. It is possible to note the oscillatory nature of the incipient phase, which almost disappears after the third turn in the fully developed phase. Predictably the recovery procedure took less time and additional rotation in the incipient spin than in the developed phase, which however remained very prompt in all the tested conditions.

Additionally three of the most common recovery procedures were simulated to determine the most suitable for the aircraft [23]. All the maneuvers produced a positive outcome denoted by a quick arrest of the rotation followed by the regain of level flight. The limitations for the flight speed and the load factor were never exceeded and the entire maneuver required only about one half additional turn before completing the recovery.

The last part of the chapter is dedicated to the study of the effects of different initial conditions on the spin maneuver. The conditions tested were the increase in weight, the increase in yawing moment of inertia and a lower starting altitude. The main effects of such modifications are tabulated in form of relative percent difference with respect to the basic spin configuration.

1.2 Description of the spin phenomenon and classification

The spin is defined as a motion in which the airplane in flight at angles of attack beyond the stall descends rapidly towards the ground, while its center of gravity describes a helical path around a vertical or near vertical axis. The spinning motion is very complicated and involves simultaneous rolling, yawing and pitching while the airplane remains at high angles of attack and sideslip.

A spin can be entered intentionally, for example as an aerobatic maneuver or as part of a pilot's training program. In this case the pilot reaches the stall and applies pro-spin controls and holds them until the recovery.

In other cases the spinning motion can be the result of an unintentional stall, if lateral and directional instability are developed. For light propeller driven airplanes this instability can be caused by an asymmetric stall, in which one wing stalls before the other. One of the possible causes for an asymmetric stall is the propeller sidewash effect. After the asymmetric stall, one wing tends to fall and the airplane rolls in the direction of the stalled wing. As the stalled wing falls, due to its higher angle of attack it generates less lift and more drag with respect to the other wing (Figure 1.2). This unbalance of lift and drag on the two wings causes rolling and yawing moments in the same direction of the initial rotation, thus forcing the rotation instead of damping it. This condition is called autorotation and if not corrected immediately by the action of the pilot this could develop into a spin. In order to achieve a stable spin mode, the aerodynamic forces and moments must be in equilibrium with the inertia forces and moments. A schematic illustration of the equilibrium of forces in a spin is shown in Figure 1.1, while the equilibrium of moments is illustrated in Figure 1.3-a. It is important to note how different mass distributions affect differently the equilibrium in a spin. In particular if the majority of the mass is distributed along the wing the resulting inertia couple generates a pro-spin yawing moment. Conversely, if the mass is distributed mainly along the fuselage, the resulting inertia couple generates an anti-spin yawing moment. The effect of the mass distribution is illustrated in Figure 1.3-b.

The entire spin maneuver from the stall to the regain of level flight can be divided into three main phases:

- Incipient spin:

This is the initial phase, beginning after the stall of the aircraft and start of rotation. This phase is characterized by oscillatory motion in roll, pitch and yaw. The rate of rotation increases from zero to the developed spin rate.

- Developed spin:

After the initial phase, if no counteracting controls are applied, it is possible that the spin reaches a steady-state condition. In this phase the aerodynamic forces and moments acting on the airplane are in equilibrium with inertia forces and moments. All the motion parameters, attitude, rotation speed, velocity of descent are time invariant and the axis of rotation is approximately vertical. To reach this condition it usually takes 2 to 4 turns. An example of an aircraft spinning motion and the equilibrium of forces is shown in Figure 1.1. However it is possible that equilibrium between aerodynamic and inertial

moments cannot be reached. In this case the spin remains oscillatory and the motion parameter show cyclic variations.

- Recovery:

This is the final phase of the spin, in which the pilot applies the necessary controls to break the equilibrium between aerodynamic and inertia moments. The rotation motion is interrupted and the angle of attack is lowered below the stall. The pilot regains control of the aircraft and is able to arrest the descent.

The rotation in a spin may be in either direction. It is not uncommon that an aircraft would behave differently spinning in one direction from the other. For jet powered aircraft the cause of this difference is mainly due to the gyroscopic effect of the rotating parts of the engine, while for propeller-driven aircraft the gyroscopic effect is combined with the effects the asymmetrical wake of the propeller.

Typical values in a spin are around $120^\circ/\text{s}$ to $150^\circ/\text{s}$ for the rate of rotation and about one half of the wing span for the radius of gyration about the spin axis.

Spins can be either erect or inverted. The difference between the two is in the sign of the angle of attack and load factor, and more precisely positive angle of attack and load factor for erect spins and negative for inverted spins.

The main classification of a spin is based on the mean angle of attack of the wing:

- Steep spin:

In a steep spin the angle of attack is between 30° to 45° so that the nose of the aircraft is 45° to 60° below the horizon. This condition is the most desirable because it is much easier to recover due to the effectiveness of the rudder outside the stalled wake of the horizontal tail.

- Flat spin:

A flat spin is characterized by a higher angle of attack, typically from 60° up to 80° . The rate of rotation is higher than that of a steep spin and the radius about the spin axis is much smaller. This is the most dangerous of the spins as it is most difficult to recover from it.

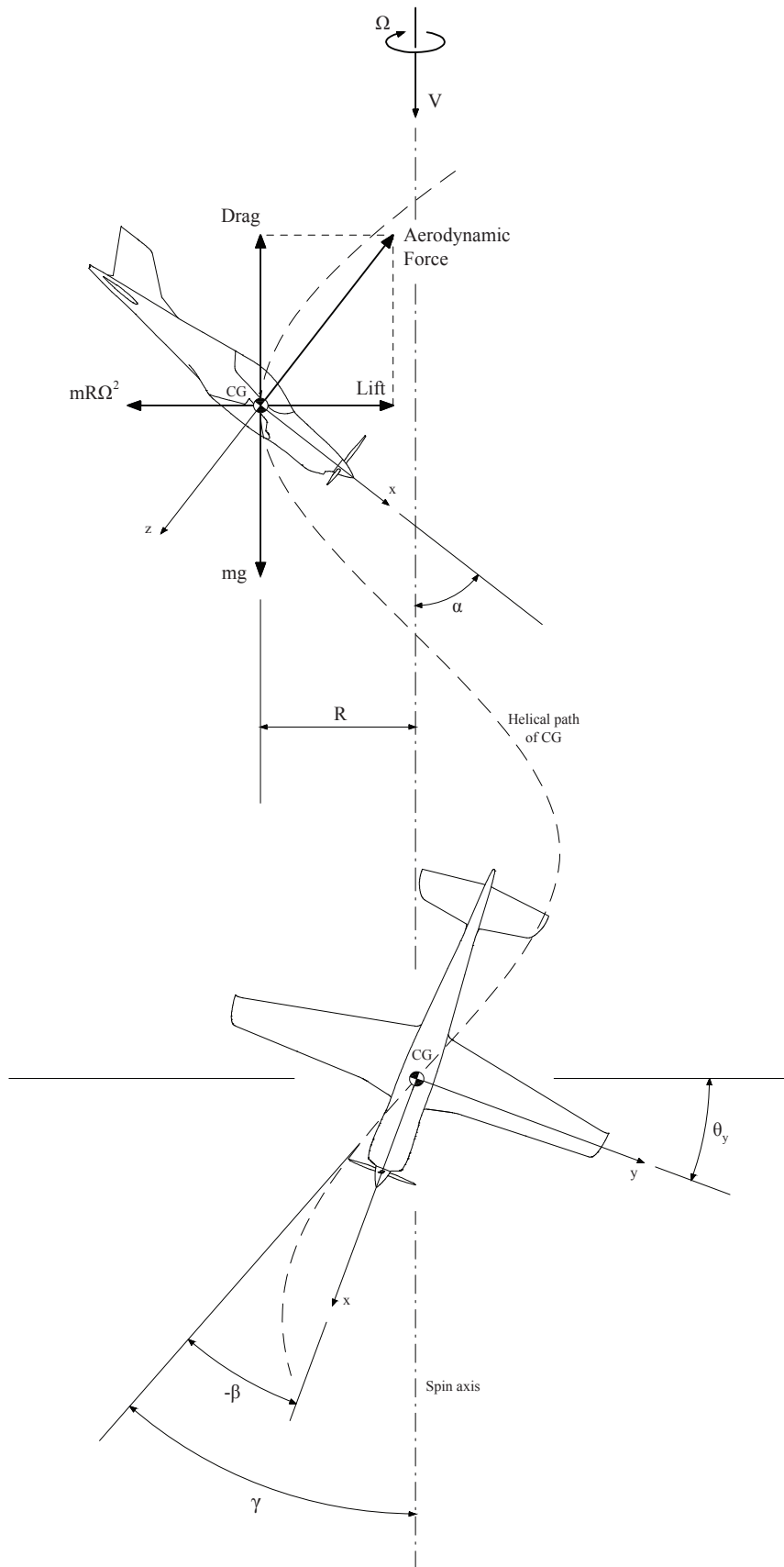


Figure 1.1: Schematic illustration of a spin and the equilibrium of forces

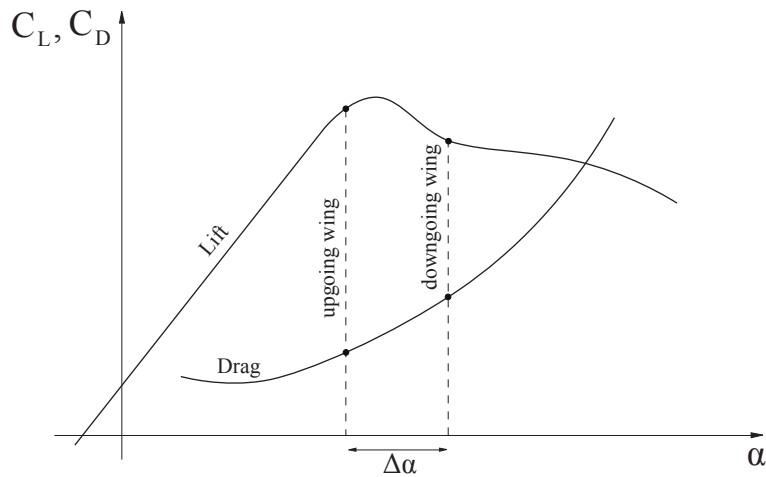
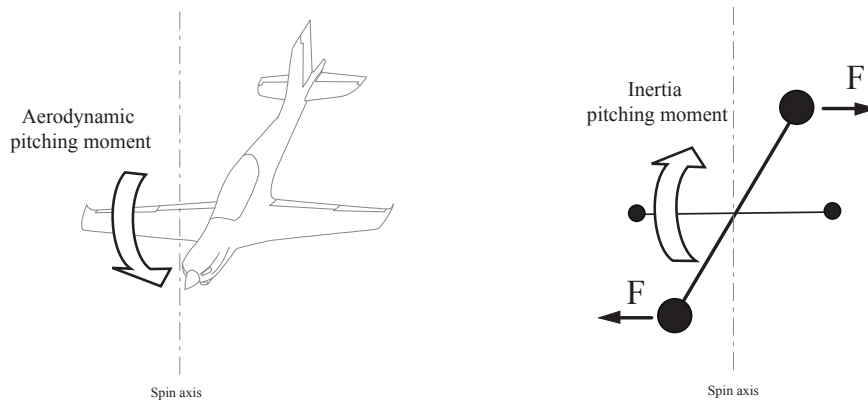
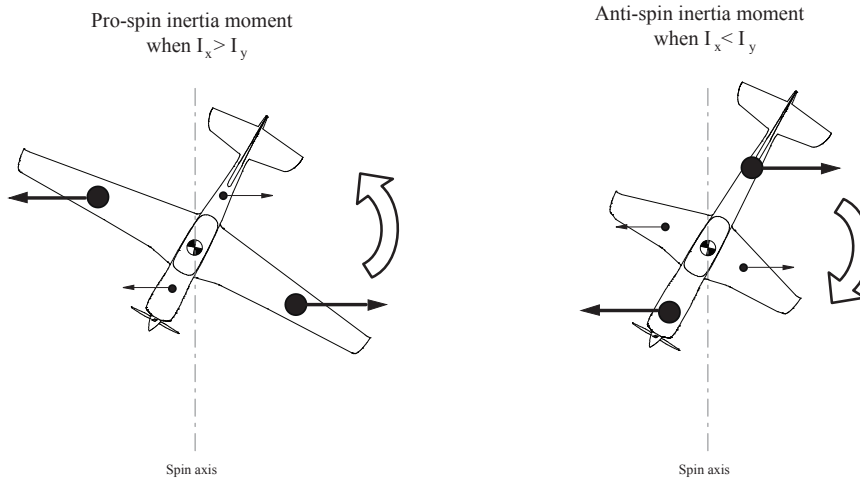


Figure 1.2: Condition of autorotation due to the stalled wing



a) Balance of aerodynamic and inertia pitching moments



b) Moments generated by different mass distributions

Figure 1.3: Aerodynamic and inertia moments in the spin equilibrium

2 Description of the airplanes

The work that was done during the period of internship that is presented in the following chapters, mainly focuses on two airplanes of the Blackshape family that are at different stages in their design process.

The first aircraft, denominated BK115, is in an advanced state of design in which the overall configuration is already finalized and only minor changes are expected. A flying prototype is already present and many flight tests have already been done. To better comprehend the spinning characteristics of the BK115, an analytical spin model was developed based on the results of the flight tests, as presented in chapter 4. Moreover, the results of preliminary spin design calculations for the same aircraft have been used as mean of comparison at the end of chapter 3.

The other aircraft, denominated BK180, is still in early design stage. An overall configuration is present but it could be subject to changes during the advancement in the design process. In chapter 3 is presented the work that was done in order to estimate its spinning behavior using semi-empirical methods for early assessment.

The two aircraft will be now presented in more detail.

2.1 BK115 general description

The BK115 is an unpressurized, single engine, light aircraft with retractable landing gear. Its airframe is mainly made of carbon fiber epoxy composite material. The cabin is able to receive a crew of up to two people, with seats in tandem configuration.

It has been certified CS-VLA for a maximum take-off weight of 750 kg, however previsions have been made to certify the aircraft in CS-23 category in order to bring the maximum take-off weight up to 850 kg.

The power plant is composed of a Lycoming IO-320-D1B internal combustion engine capable of developing a maximum continuous power of 160 hp at 2700 rpm. It mounts a three-bladed propeller with variable pitch and a diameter of 1.75 m, directly coupled to the crankshaft.

Other characteristics of the aircraft are expressed in the following tables.

Table 2.1: BK115 geometric characteristics

b	Wing span	9 m
S	Wing area	10.31 m ²
AR	Aspect ratio	7.86
\bar{c}	Mean aerodynamic chord	1.36 m
Γ	Dihedral angle	4°
ε_t	Wing twist	-3°
$\Lambda_{c/4}$	Quarter chord sweep	1°
c_{root}	Root chord	1.65 m
c_{tip}	Tip chord	0.66 m
S_h	Horizontal tail area	2.36 m ²
S_v	Vertical tail area	1.24 m ²
l_f	Fuselage length	7.36 m
	Overall length	7.437 m

Table 2.2: BK115 structural and aerodynamic limitations

Maximum take-off weight	750 kg
Maximum landing weight	750 kg
CG forward limit	23% MAC
CG rearward limit	31% MAC
Maximum positive load factor (flap up)	+5
Maximum negative load factor (flap up)	-2.5
Maximum positive load factor (flap down)	+2
Maximum negative load factor (flap down)	0
Maneuvering speed (CAS)	63 m/s (123 kts)
Never exceed speed (CAS)	88 m/s (172 kts)
Maximum flap extended speed (CAS)	46 m/s (90 kts)

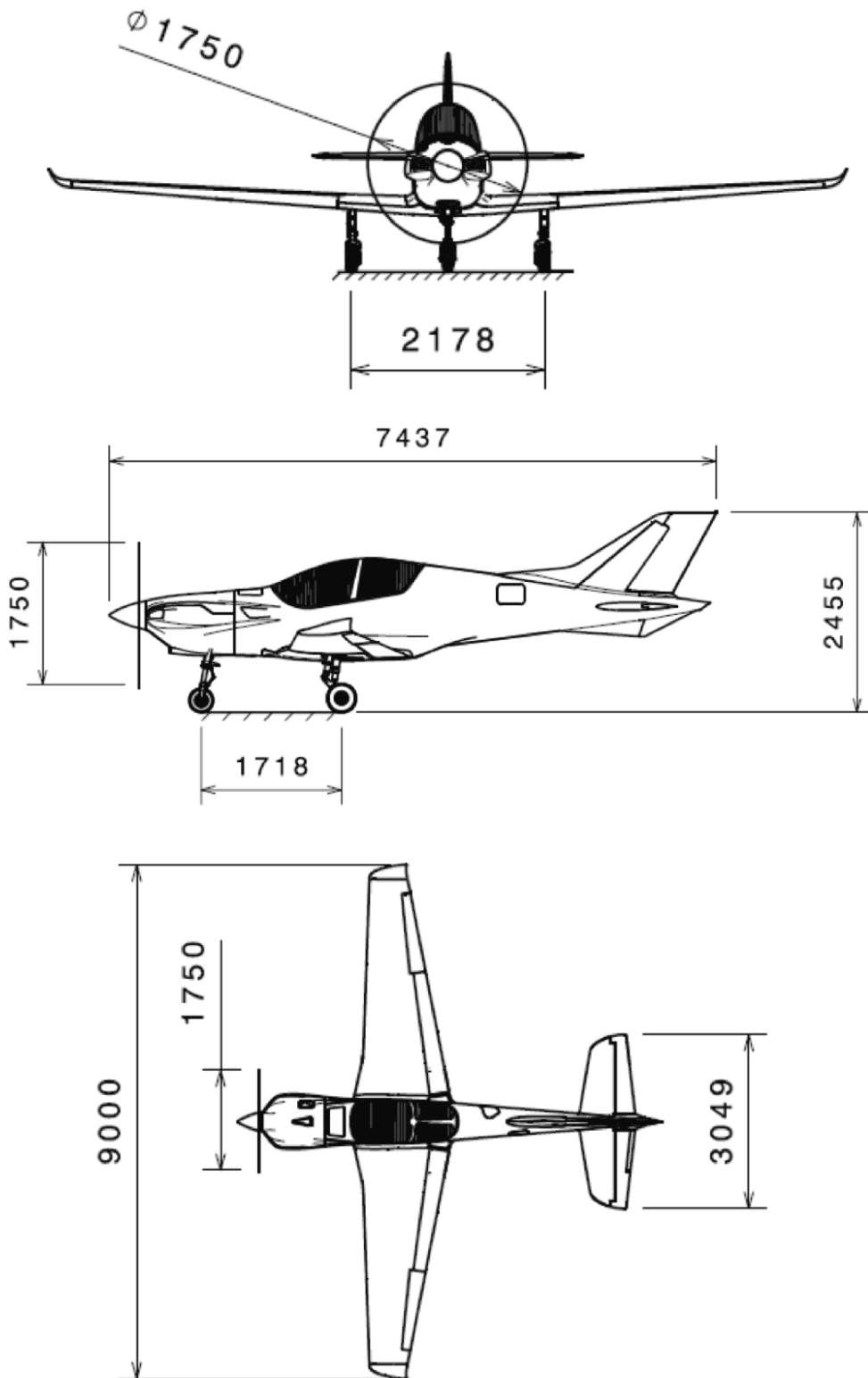


Figure 2.1: BK115 three-view

2.2 BK180 general description

The BK180 maintains most of the general characteristics of its predecessor. It is an unpressurized, single engine, light aircraft with retractable landing gear and full carbon composite airframe. The crew is composed of a maximum of two people in tandem configuration.

One of the main differences is the increased maximum take-off weight for which it will need to be certified CS-23. Two versions of the same aircraft are under development, one for the 'Utility' category with a maximum weight of 1050 kg and the other for the 'Aerobatic' category with a maximum weight of 900 kg.

Another difference is the more powerful engine installed consisting in a Lycoming IO-360-M1A capable of developing a maximum continuous power of 180 hp.

The need for the new design is to appeal to the military market, with a more powerful machine capable of carrying increased payload and providing overall better performances.

From the point of view of the aircraft geometries, the wing will remain mostly the same with the main difference being the increased aileron span for better lateral control authority. Another more significant difference is the tail design: the tail section has been lengthened by 300 mm; the vertical tail had its fixed part increased in size and had been brought forward with respect to the horizontal tail by 100 mm.

The ventral fin, present in the BK115, is not present in the first iteration of the design of the BK180.

Other characteristics of the aircraft are shown in the following tables.

Table 2.3: BK180 geometric characteristics

b	Wing span	9 m
S	Wing area	10.31 m ²
AR	Aspect ratio	7.86
\bar{c}	Mean aerodynamic chord	1.36 m
Γ	Dihedral angle	4°
ϵ_t	Wing twist	-3°
$\Lambda_{c/4}$	Quarter chord sweep	1°
c_{root}	Root chord	1.65 m
c_{tip}	Tip chord	0.66 m
S_h	Horizontal tail area	2.36 m ²
S_v	Vertical tail area	1.46 m ²
l_f	Fuselage length	7.66 m

Table 2.4: BK180 structural and aerodynamic limitations

Maximum take-off weight (utility)	1050 kg
Maximum take-off weight (aerobatic)	900 kg
Maximum landing weight (utility)	1000 kg
Maximum landing weight (aerobatic)	855 kg
CG forward limit	22% MAC
CG rearward limit	32% MAC
Maximum positive load factor (utility)	+4.4
Maximum negative load factor (utility)	-2
Maximum positive load factor (aerobatic)	+6
Maximum negative load factor (aerobatic)	-3
Maneuvering speed (CAS)	74 m/s (143 kts)
Never exceed speed (CAS)	120 m/s (233 kts)

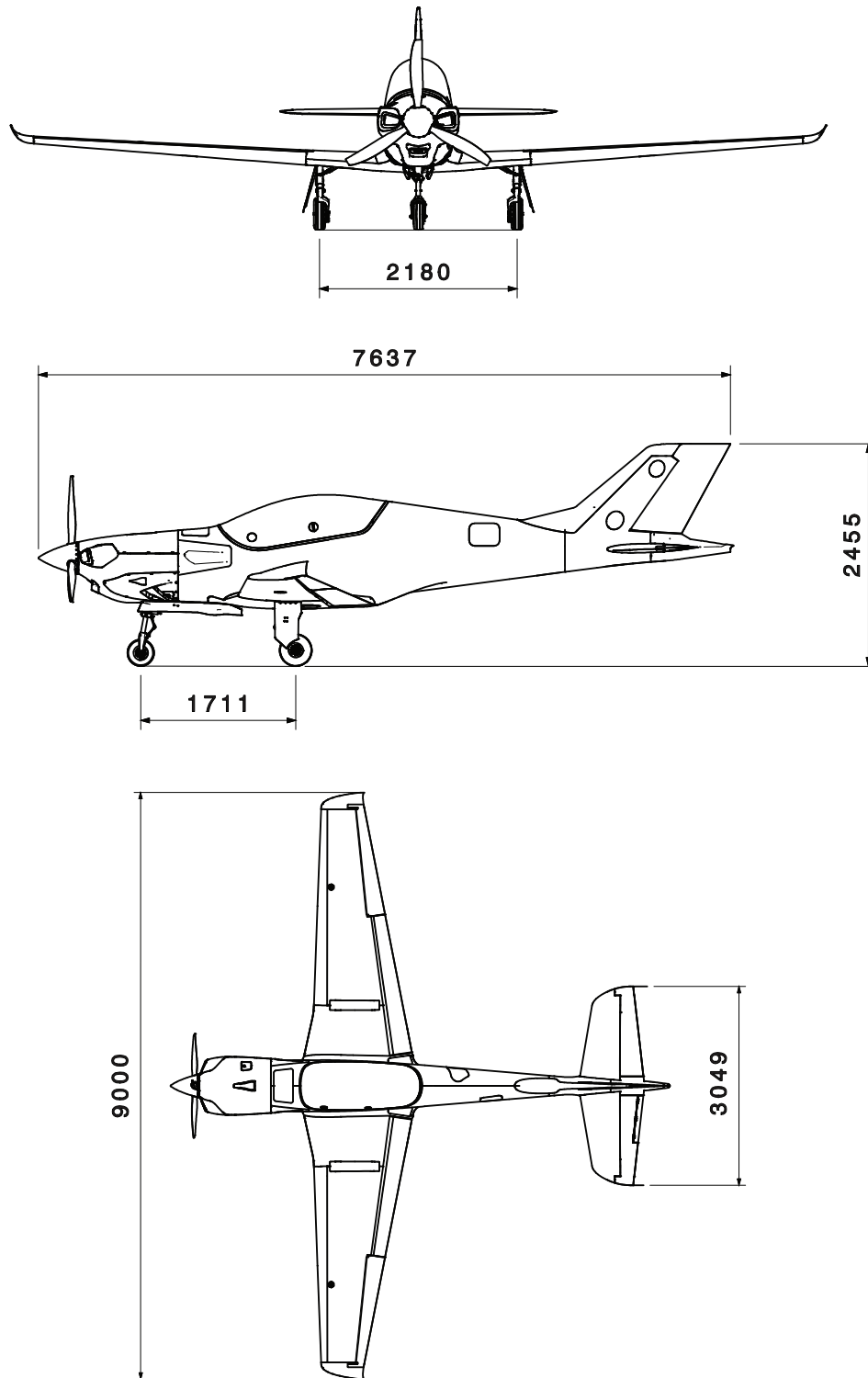


Figure 2.2: BK180 three-view

3 Semi-empirical methods

Many aircraft research facilities have made an attempt in the past to define simple criteria for the prediction of the spin and the recovery characteristics of an aircraft.

These semi-empirical methods are derived from the vast amount of data obtained from numerous experimental tests carried out over the course of many years of research on full-scale aircraft or on dynamically scaled models in free-spinning vertical wind tunnels. From the experience gained with all the experimental tests it was possible to formulate simplified criteria capable of predicting the spin recovery performance of an aircraft even in the early stage of its design.

The advantage of using these criteria is mainly due to their simplified nature, not requiring extensive tests but only simple calculations. In fact the only data required to be able to have an estimation of the spinning behavior are the geometric and inertial characteristics of the aircraft. By applying these methods it is possible to define the design requirements for satisfactory spin and spin recovery performance beginning from early design stages prior to further, more accurate investigations.

Even if it might seem they take an overly simplistic approach, the aim of the criteria presented is not an in-depth analysis on the spin problem but rather the definition of simple guidelines to aid in the design process and to be able to make corrections in a stage where it is inexpensive to do so.

In the present chapter will be illustrated the two most used methods that have been refined over the years and that are believed to be the most reliable in the early prediction of the spin.

These methods will be applied to the aircraft denominated BK180, which is still in early design stage and is required to be able to perform a safe and predictable spin maneuver, thus making it the perfect candidate for preliminary spin assessment.

The results of the application of the two methods will then be compared with the same results obtained for the BK115, which were already available. Such comparisons are of great significance because of the similarities between the two aircraft and even more so because the BK115, in its final design stage, exhibited good spinning characteristics during flight-testing.

3.1 Aircraft configurations

For the study of the spin behavior and the spin recovery of an aircraft it is of great importance to take into consideration the different configurations that the aircraft may assume. The characteristics that are found to be of greatest relevance by both the semi-empirical methods are the load conditions and the overall tail configuration.

3.1.1 Load conditions

The load conditions are defined by the different weight distributions of the aircraft, which would generate different values of moments of inertia. It is well known that the moments of inertia and the ratios between them greatly affect the spin behavior of the aircraft and the main control actions for the recovery.

Moreover the different positions of the center of gravity will affect the tail arm, which correlates with the anti-spin moment that the rudder would be able to generate during the recovery procedure.

In the following part of the work 3 different load conditions are considered in order to perform the study using the semi-empirical methods. These conditions were considered of greatest significance because they include the extreme values of the center of gravity envelope at maximum achievable take off weight for the Aerobatic configuration. The main characteristics of the 3 load conditions are expressed in Table 3.1 and their position in the envelope is shown in Figure 3.1.

Table 3.1: Load case conditions considered for the semi-empirical methods

	Load case A	Load case B	Load case C
Mass [kg]	850	900	900
CG position [%MAC]	22%	28%	32%
I_x [kgm ²]	930	933	846
I_y [kgm ²]	1332	1430	1476
I_z [kgm ²]	2193	2288	2252

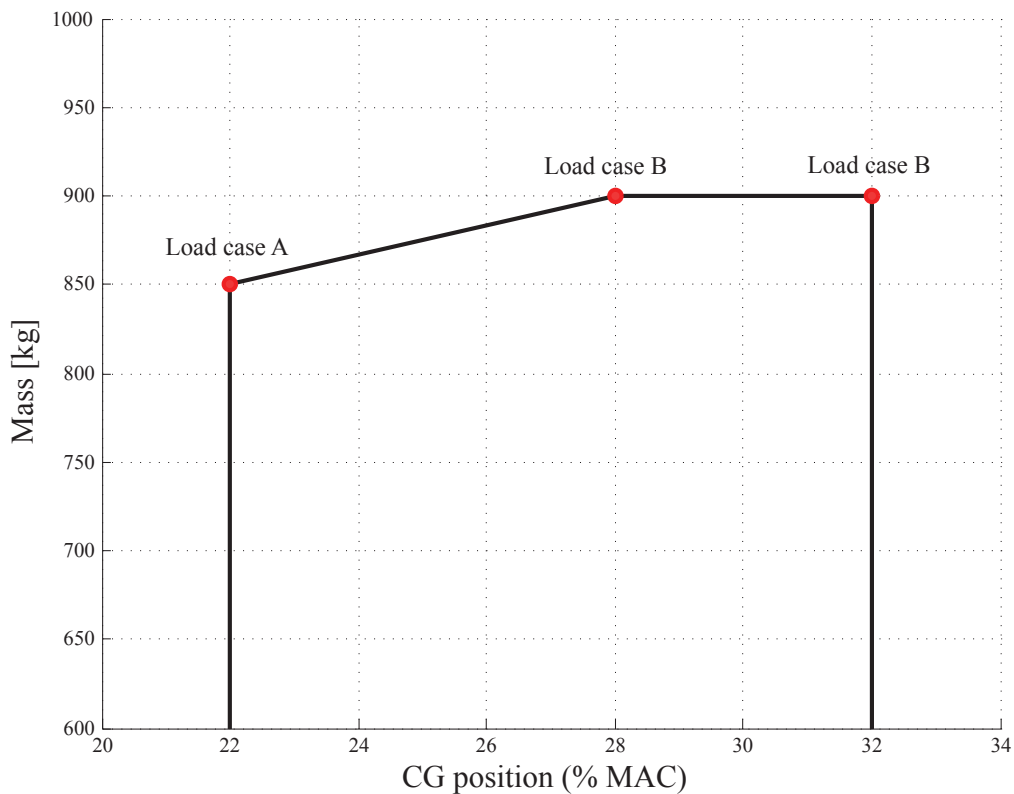


Figure 3.1: CG envelope and the 3 load case conditions considered

3.1.2 Tail design configurations

The other significant aspect that affects the most the spin recovery characteristics of the aircraft is the tail configuration. Since the main control for recovery from a spin is the deflection of the rudder against the rotation, it is important that it remains effective at the high angles of attack and angles of sideslip that characterize the spin. The characteristic of the tail configuration that is found to be the most effective in the damping of the spin rotation is the fixed area below the horizontal tail. To maximize the damping effect produced by the tail, for the semi-empirical calculations that will be shown in the following paragraphs, it was also considered the addition of anti-spin fillets and a ventral strake.

The main tail configurations that have been used are the following:

- Clean configuration

The tail design for the clean configuration is shown in Figure 3.2 and the area below the horizontal tail and its distance from the center of gravity are expressed in Table 3.2.

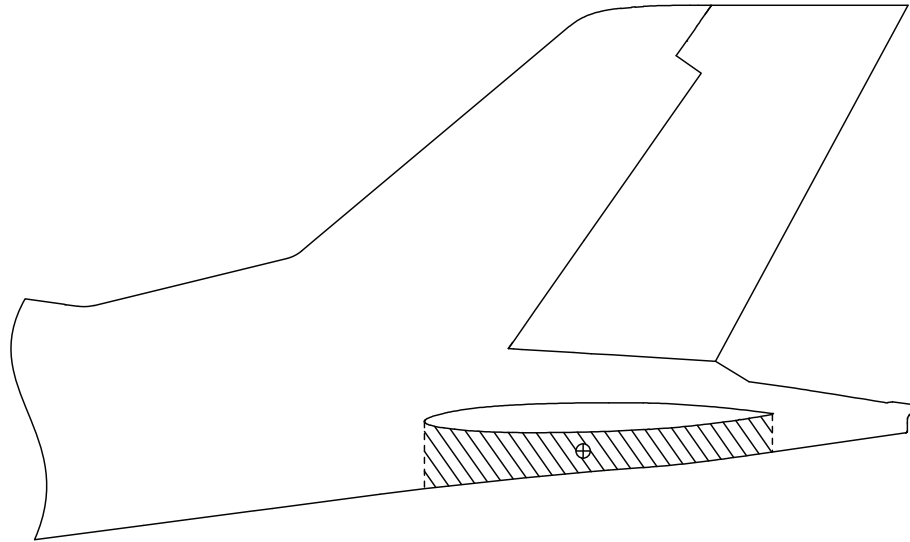


Figure 3.2: Clean configuration tail design and area below the horizontal tail

Table 3.2: Area below horizontal tail for clean configuration and distance from CG

	Area below HT [m ²]	Distance from CG [m]		
		22%	28%	32%
Clean configuration	0.1169	4.279	4.196	4.143

- Ventral strakes

Two different designs of ventral strake were considered for the computation of the semi-empirical spin recovery criteria. The main difference between the two is their surface area.

For the design it was taken into account the angle of clearance of 15° needed for take-off and the possibility to maximize the area most effective in the damping of the spin. The smaller strake maximizes the area below the horizontal tail alone, while the larger one is an extended version in order to maximize the area below the anti-spin fillets and horizontal tail combined.

The overall characteristics of the two strake designs are shown in Figure 3.3 and expressed in Table 3.3.

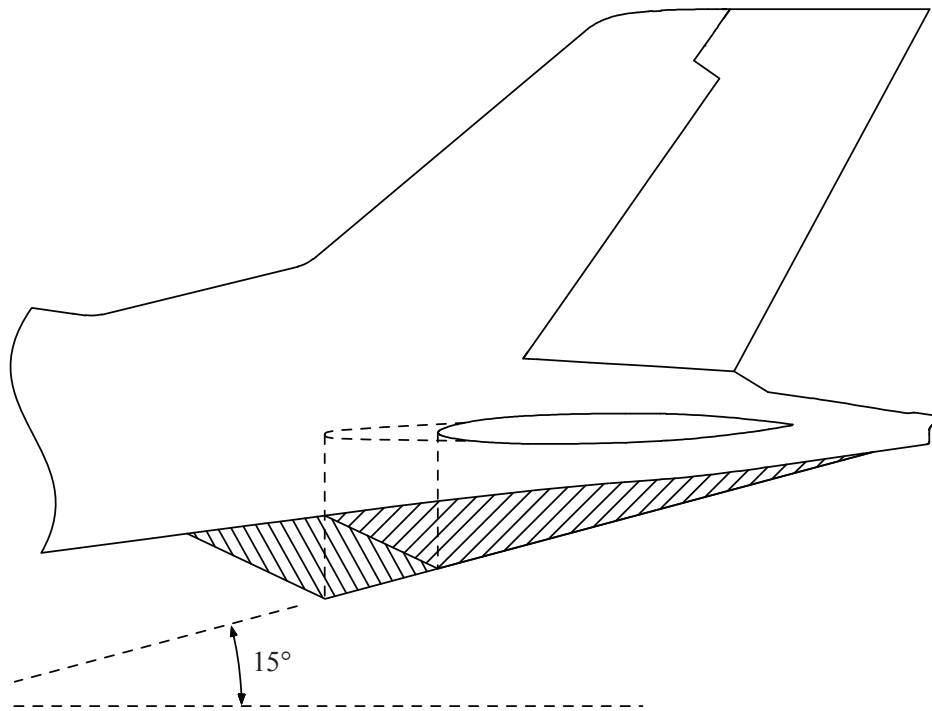


Figure 3.3: Ventral strake designs

Table 3.3: Ventral strakes surface areas

	Total area [m ²]	Area below HT [m ²]	Area below fillets [m ²]
Strake 1	0.1307	0.1020	0.0287
Strake 2	0.2094	0.1020	0.0641

- Anti-spin fillets

Anti-spin fillets are extensions of the leading edge of the horizontal tail. Their main function is to extend the area below the horizontal tail surface that can be considered the most effective in the damping of the spin rotation. However their overall dimension is small enough not to extend the stalled wake of the horizontal tail. Their effect is explained in greater detail in Reference [10].

The fillets that have been considered for the computation extend the leading edge of the horizontal tail for 300 mm and form an angle with the sides of the fuselage of 12°. (Figure 3.4)

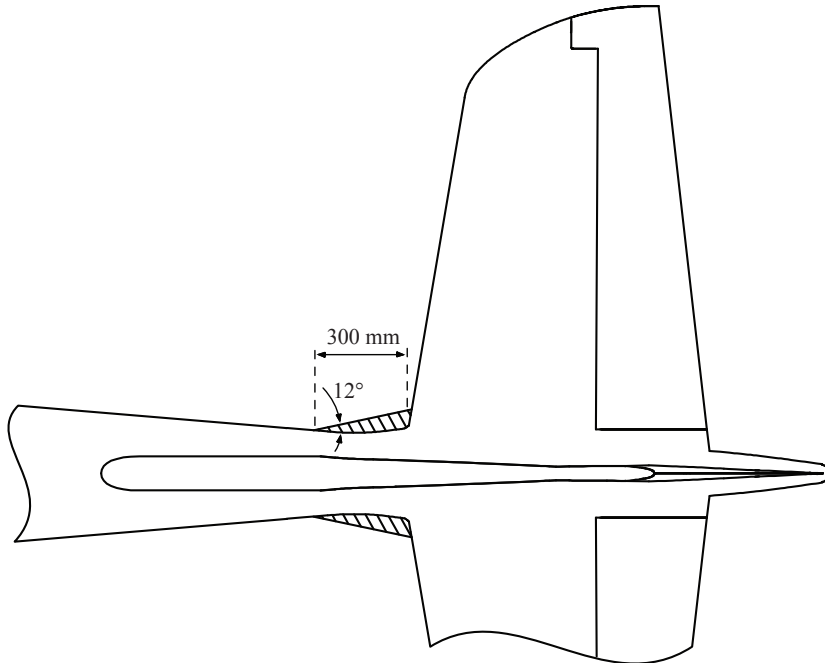


Figure 3.4: Anti-spin fillets

The effect of the anti-spin fillets has been considered for the clean configuration as well as for the two configurations with the ventral strakes.

The total effective area below the horizontal tail can be considered extended for the length of the fillets. In Figure 3.5 is shown the extended effective area below the horizontal tail and fillets for the clean configuration.

The new values for these areas for all the configurations are expressed in Table 3.4.

Table 3.4: Total effective area below the horizontal tail with anti-spin fillets

	Area below HT and fillets [m ²]	Total effective area [m ²]
Clean	0.1757	0.1757
Strake 1	0.1307	0.3064
Strake 2	0.1661	0.3418

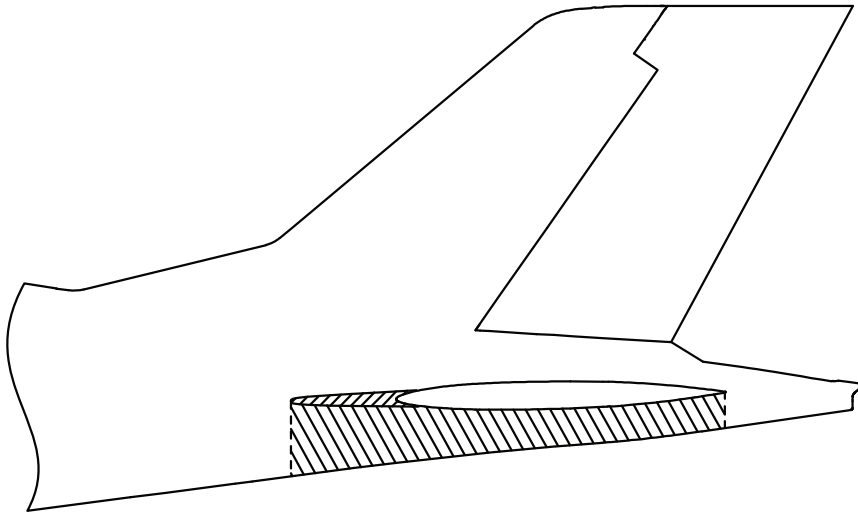


Figure 3.5: Extended effective area below the horizontal tail due to the presence of anti-spin fillets

3.2 NACA-Bowman criterion

The first of the two semi-empirical methods for spin prediction that is going to be presented has been illustrated by James Bowman in Reference [6].

The criterion has been developed by NACA in an attempt to predict the recovery from a spin knowing only the geometrical and inertial characteristics of the aircraft under development.

The foundation from which this method was formulated is the results of spin-tunnel tests of free-spinning dynamically scaled models of about 100 different types of aircraft, performed by NACA in the Langley research center.

The purpose of this method is to provide guidelines in the early stage of the design of a new general-aviation aircraft by defining boundaries for satisfactory and unsatisfactory recovery performance based on the results of previous experimental tests.

Three main factors are considered to be of greatest importance in the spinning characteristics by the present criterion. These factors are the relative distribution of mass between the fuselage and the wing, the relative density of the aircraft with respect to the density of the air, and the overall tail design configuration.

3.2.1 Main factors

The three main factors found to be of greatest relevance in a spin are here analyzed in more detail.

- Mass distribution

The way the mass is distributed between the fuselage and the wing greatly affects how it will respond to control movement while the aircraft is spinning. This will have an influence on the necessary controls to be applied during recovery.

Since there are angular rotations about all three axes of the aircraft, inertia moments are generated by the rotating masses.

The mass distribution is evaluated using the inertia yawing moment parameter (IYMP) as follows:

$$IYMP = \frac{I_x - I_y}{mb^2}$$

The parameter will be positive for wing-heavy loading of the aircraft, negative for fuselage-heavy loading and about zero for the so called zero loading.

To recover from a spin the main control applied by the pilot is the rudder deflected fully against the direction of rotation. However the type of loading of the aircraft affects the supplementary control action to aid in the recovery: elevator down for wing-heavy and ailerons deflected in the direction of rotation for fuselage-heavy loading.

- Relative density

The relative density factor is an indication of the density of the aircraft relative to the density of the air in which it is flying.

The relative density factor is expressed by the following formula:

$$\mu = \frac{m}{\rho S b}$$

Aircraft with higher relative density factors require more control effectiveness to recover from a spin and would need an increase in the number of additional turns in order to stop the rotation.

- Tail configuration

The tail configuration is a very important factor in a spin, being the rudder the primary control action for the recovery procedure.

A relatively large moment is needed to upset the balance between aerodynamic and inertia moments, therefore it is important that the rudder remains effective at spin attitudes where large angles of attack and sideslip are present. The main problem is that during a spin a large portion of the rudder is shielded by the wake produced by the horizontal tail, which would reduce its effectiveness.

From the experience gained from many years of spin-tunnel tests NACA developed a tail design criterion for spin recovery. The criterion is expressed through the tail-damping power factor (TDPF), an empirically determined parameter, based on various geometric properties of the horizontal and vertical tail, which gives an indication of the effectiveness of the overall tail configuration in terminating a spin.

3.2.2 Tail-damping power factor

For the computation of the tail-damping power factor it is necessary first to take into consideration the fixed area below the horizontal tail. As already mentioned, this particular section of the tail is considered to be the most effective in the damping of the spinning rotation and greatly affects the attitude assumed by the aircraft during the maneuver.

The effectiveness of the area below the horizontal tail is converted in coefficient form through the tail-damping ratio (TDR), which has the following expression:

$$\text{TDR} = \frac{S_F L_F^2}{S \left(\frac{b}{2}\right)^2}$$

In which S_F is the area of the fixed portion of the tail below the horizontal surface and L_F is the distance of its centroid from the center of gravity of the aircraft as shown in Figure 3.6.

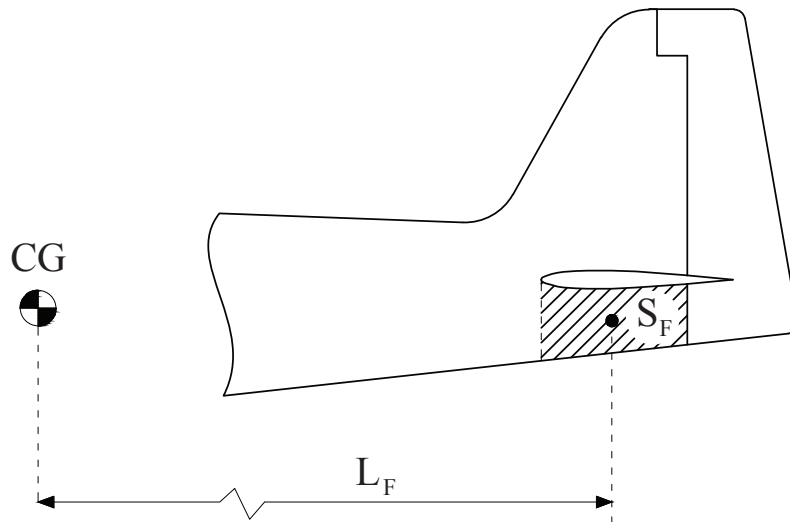


Figure 3.6: Fixed area below the horizontal tail and its distance to the center of gravity

Part of this criterion states that, as a result of the research, if the value of tail-damping ratio was found to be lower than the threshold value of 0.019, the angle of attack at spin attitudes should be assumed at 45° . Considering a wake spread of 15° per side, the wake boundaries would be defined by two lines at 60° and 30° starting respectively from the leading edge and trailing edge of the horizontal tail (Figure 3.7-a).

If instead the value of tail-damping ratio is greater than 0.019, the angle of attack should be assumed at 30° and the wake boundaries defined by 45° and 15° lines (Figure 3.7-b).

It can be seen clearly from the figure the importance of the aircraft attitude in terms of angle of attack, as defined by the tail-damping ratio. In fact a larger value of TDR would result in a steeper attitude and consequently a narrower wake of the horizontal tail. As a result, the relatively larger portion of the rudder exposed to the free stream of air would be most effective in the spin termination during the recovery procedure. On the contrary, a lower value of TDR could result in a flatter spin, for which most if not all of the rudder surface would be shielded by the horizontal tail, making it very difficult or even impossible to recover.

For these considerations and the ones that will follow during the practical application of the criterion, it is noticeable the great importance of the fixed portion of the tail below the horizontal surface, and the necessity to maximize this area in order to achieve a tail-damping ratio that will exceed the threshold value.

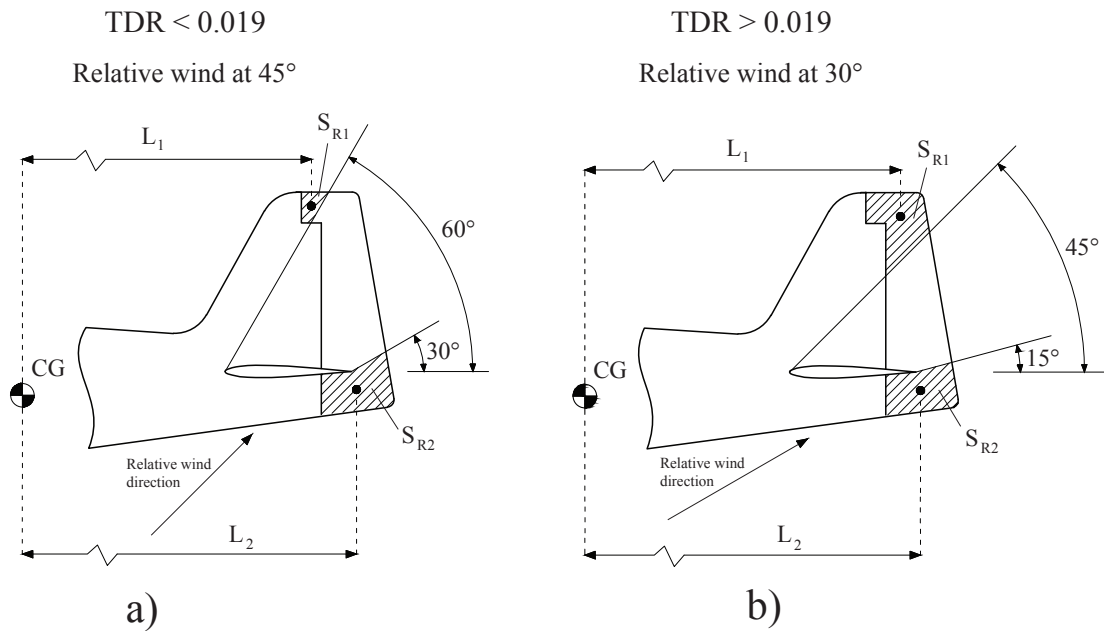


Figure 3.7: Unshielded rudder area and its distance from the center of gravity for two different values of angle of attack

The second parameter to be determined for the computation of the tail-damping power factor is the unshielded rudder volume coefficient (URVC), which evaluates the effectiveness of the area of the rudder outside the stalled wake to provide the necessary moment to stop the spinning rotation. Its expression is given in the formula below and the meaning of the symbols is shown in Figure 3.7.

$$\text{URVC} = \frac{S_{R1}L_1 + S_{R2}L_2}{S \frac{b}{2}}$$

The tail-damping power factor can be now computed simply by multiplying the tail-damping ratio coefficient by the unshielded rudder volume coefficient:

$$\text{TDPF} = \text{TDR} \times \text{URVC}$$

By plotting the tail-damping power factor as a function of inertia yawing-moment parameter for each dynamically scaled model it was possible to define boundaries between satisfactory and unsatisfactory recovery characteristics. This procedure was carried out by NASA for different ranges of relative density in order to define the criterion for spin recovery. An example of these plots is shown in Figure 3.8 [11] and the resultant criterion is shown in Figure 3.9 [6].

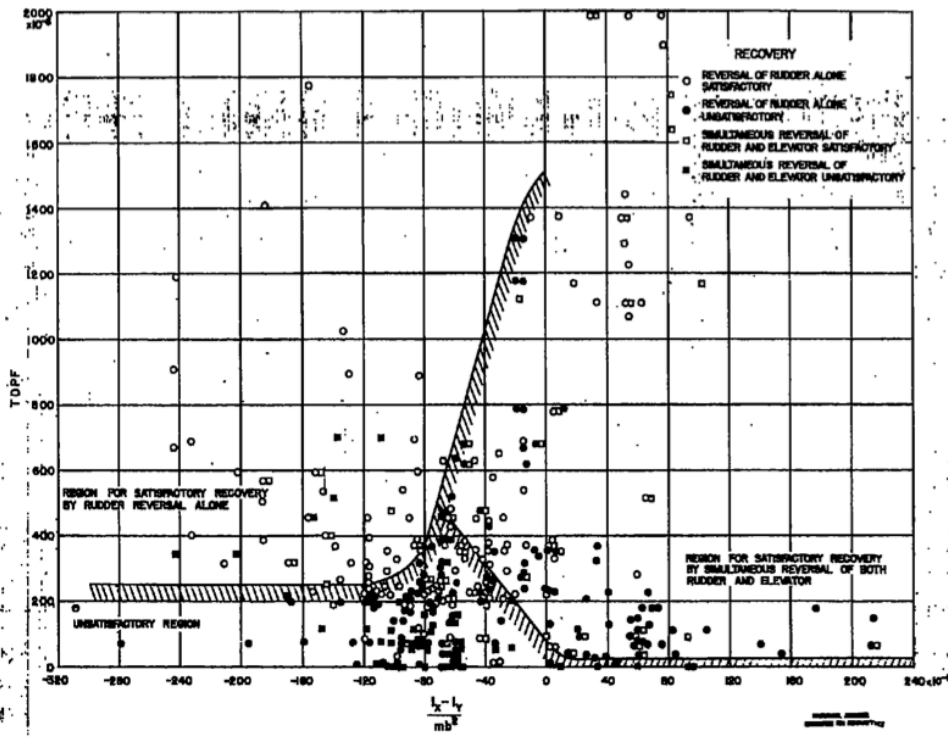


Figure 3.8: Spin recovery requirements for airplanes of relative density of 15 or less

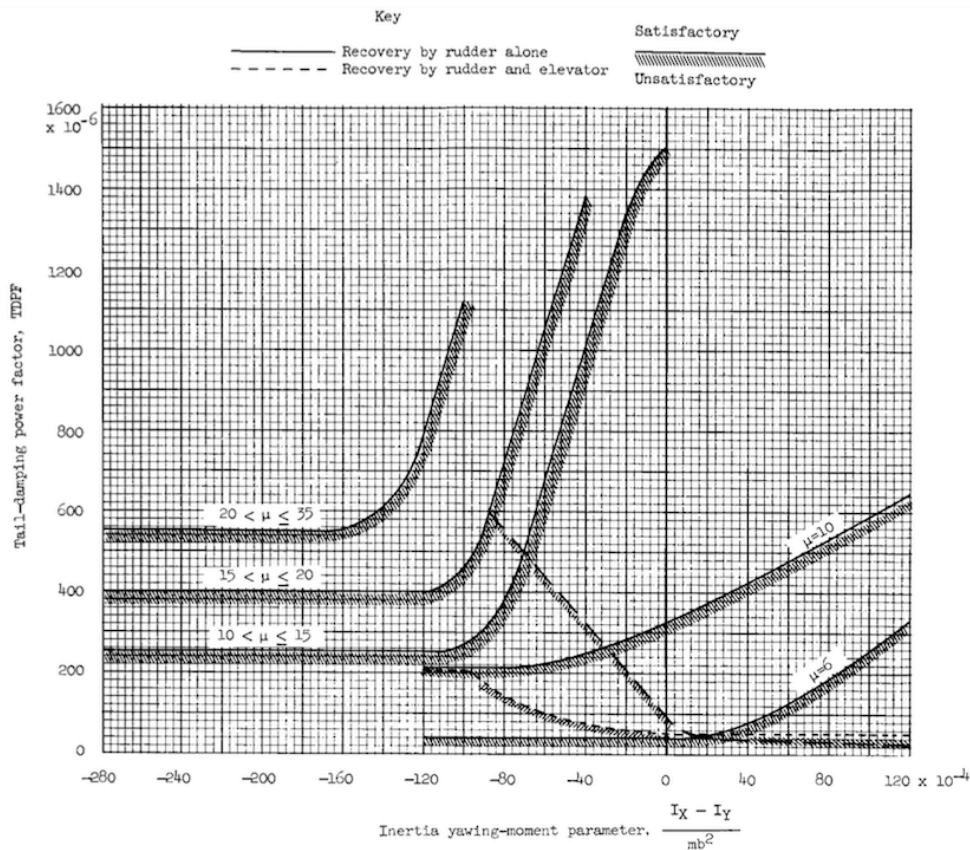


Figure 3.9: NACA criterion for spin recovery for aircraft of relative density between 6 and 35

3.2.3 Application of the criterion

To proceed to the calculation of the spin prediction criterion, the 3 load conditions described in the beginning of the chapter were considered.

The first step for the evaluation of the tail-damping power factor is to compute the value of tail-damping ratio to be able to define the boundaries of the wake of the horizontal tail.

The dimensions needed are the fixed area below the horizontal tail and the distance of its centroid from the center of gravity (Table 3.5):

Table 3.5: Fixed area below the horizontal tail for the clean configuration

	S_F , area below HT [m ²]	L_F , distance from CG [m]		
		Load A	Load B	Load C
Clean configuration	0.1169	4.279	4.196	4.143

The resulting values of tail-damping ratio calculated for the clean tail configuration and the three load conditions are shown below:

$$\text{TDR} = \frac{S_F L_F^2}{S \left(\frac{b}{2}\right)^2} = \begin{cases} 0.0103 & \text{(load case A)} \\ 0.0099 & \text{(load case B)} \\ 0.0096 & \text{(load case C)} \end{cases}$$

Since the value of tail-damping ratio is lower than 0.019 for every load condition, the angle of attack is considered at 45° and the horizontal tail wake boundaries defined by lines at 60° and 30°. As can be seen from Figure 3.10, having such a wide horizontal tail wake, would shield the entire surface of the rudder, meaning it would have no effect in the spin recovery procedure.

Trying to compute the unshielded rudder volume coefficient would give a null result, as well as the value of the overall tail-damping power factor.

The application of the criterion to the clean tail configuration would result in a failure to meet the recovery requirements.

It is clear that the NACA criterion for spin-recovery heavily relies on a large enough portion of the rudder not to be shielded by the wake of the horizontal tail to be able to satisfactorily recover from a spin. In order for the aircraft under study to achieve a positive recovery performance, it is necessary to apply measures to obtain a tail-damping ratio of 0.019 or greater, in which case a portion of the rudder would remain effective.

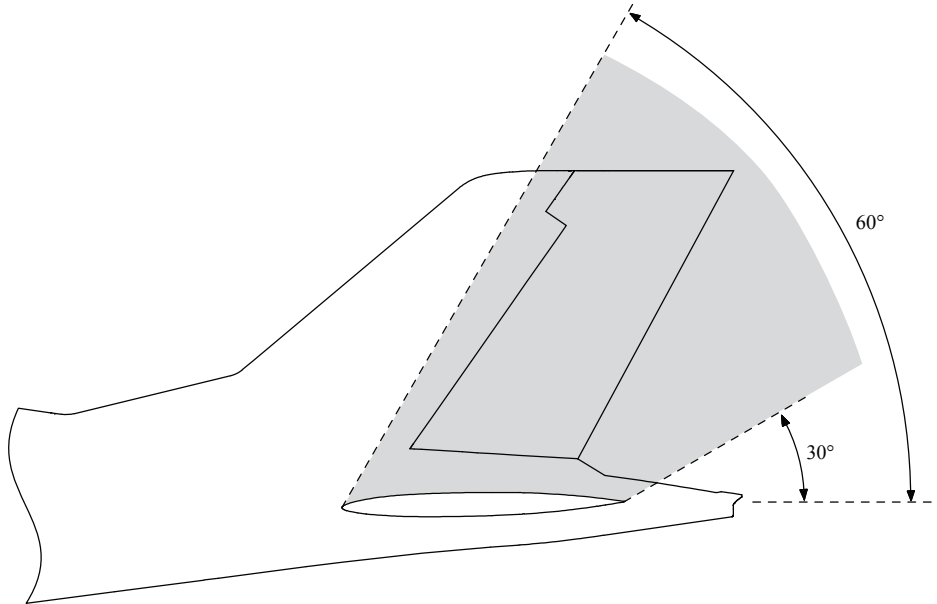


Figure 3.10: Horizontal tail wake shielding the entire surface of the rudder

The possibility to improve the outcome of the criterion by increasing the tail-damping ratio is discussed in Reference [10], which reports the use of ventral strakes and anti-spin fillets as being beneficial in the spin recovery performance.

The effects of the addition of such surfaces are presented in the following paragraphs.

3.2.4 Ventral strake

The first measure that was considered in order to obtain a larger value of TDR was to apply a ventral strake to the rear part of the tail section. The main effect of the addition of a ventral strake is to achieve a larger area below the horizontal tail surface. This section of the tail, which gives the most contribution to the damping of the spin rotation, in the original design is very small due to its slender shape.

The two strake designs considered were shown in 3.1.2.

For both the designs the area underneath the horizontal tail is the same, since there is the constraint given by the angle of clearance needed for take-off.

Table 3.6: Fixed area below the horizontal tail for the configuration with the ventral strake

	S_F , total area below HT [m ²]	L_F , distance from CG [m]		
		Load A	Load B	Load C
Strake 1 & 2	0.2189	4.239	4.156	4.102

The tail-damping ratio was calculated again for the tail configuration with the addition of the ventral strake and gave the following results:

$$\text{TDR} = \begin{cases} 0.0188 & \text{(load case A)} \\ 0.0181 & \text{(load case B)} \\ 0.0176 & \text{(load case C)} \end{cases}$$

The obtained values of TDR are still below the threshold value of 0.019, for all the load conditions. This means that the simple addition of these particular designs of ventral strake would not affect the result of the criterion, which would still produce a null outcome.

3.2.5 Anti-spin fillets

The other measure that is possible to adopt in order to increase the tail-damping ratio is the installation of anti-spin fillets. Their design has been shown already in 3.1.2.

In the presence of anti-spin fillets, the area that can be considered effective in the damping of the rotation is extended to the fixed portion of the tail below the horizontal surface and the fillets combined.

The computation of the tail-damping ratio was done both for anti-spin fillets alone and in combination with the effect of the ventral strake.

The values of increased effective area for the clean configuration and for the two configurations with strakes are expressed in Table 3.7 along with the distance from the center of gravity.

Table 3.7: Fixed area below the horizontal tail and fillets for the three configurations

	S_F , total effective area below HT and fillets [m ²]	L_F , distance from CG [m]		
		Load A	Load B	Load C
Clean	0.1757	4.078	3.995	3.942
Strake 1	0.3064	4.084	4.001	3.948
Strake 2	0.3418	4.037	3.954	3.901

The tail-damping ratio calculated with the anti-spin fillets for all the load conditions and tail configurations are shown in Table 3.8.

Table 3.8: Tail-damping ratio with the anti-spin fillets

	TDR		
	Load A	Load B	Load C
Clean + Fillets	0.0140	0.0134	0.0131
Strake 1 + Fillets	0.0245	0.0235	0.0229
Strake 2 + Fillets	0.0267	0.0256	0.0249

For the two tail configurations with both the anti-spin fillets and the ventral strakes, the value for tail-damping ratio exceeds the threshold value of 0.019, beyond which it is possible to assume the angle of attack at 30° . In this case the wake boundaries can be represented by lines at 45° and 15° .

It is now possible to calculate the unshielded rudder area when the angle of attack is considered at 30° as shown in Figure 3.11. The values of the unshielded rudder area and the distance of its centroid from the center of gravity are expressed in Table 3.9 for all the load conditions.

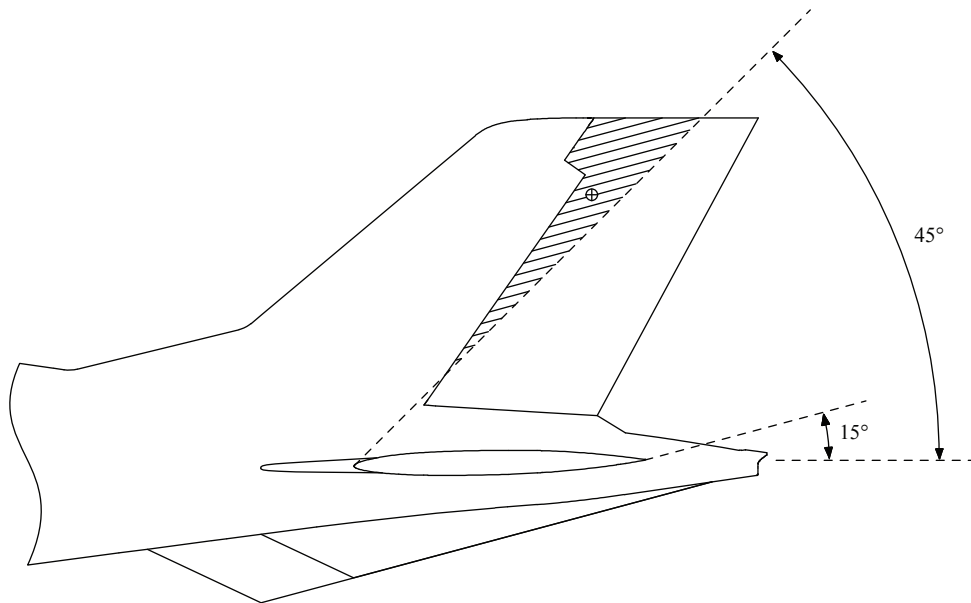


Figure 3.11: Unshielded rudder area and its centroid for wake boundaries at 45° and 15°

Table 3.9: Unshielded rudder area and its distance from the center of gravity

S_{R1} , unshielded rudder area [m ²]	L_1 , distance from CG [m]		
	Load A	Load B	Load C
0.1266	4.630	4.547	4.494

The unshielded rudder volume coefficient can be computed and the results for the three load conditions are as follows:

$$URVC = \frac{S_{R1}L_1}{S \frac{b}{2}} = \begin{cases} 0.0126 & \text{(load case A)} \\ 0.0124 & \text{(load case B)} \\ 0.0123 & \text{(load case C)} \end{cases}$$

The tail-damping power factor can finally be computed by multiplying the unshielded rudder volume coefficient by the tail-damping ratio for the two configurations with both the ventral strake and the anti-spin fillets combined.

The results are shown in Table 3.10:

Table 3.10: Values of tail-damping power factor for the two configurations with strake and fillets

	TDPF · 10 ⁶		
	Load A	Load B	Load C
Strake 1 + Fillets	309	291	280
Strake 2 + Fillets	337	317	305

To be able to plot the values of tail-damping power factor on the graph that defines this semi-empirical spin prediction criterion it is needed to compute the inertia yawing-moment parameter as follows:

$$IYMP = \frac{I_x - I_y}{mb^2} = \begin{cases} -58.2 \cdot 10^{-4} & \text{(load case A)} \\ -68.2 \cdot 10^{-4} & \text{(load case B)} \\ -86.4 \cdot 10^{-4} & \text{(load case C)} \end{cases}$$

The resulting graph is shown in Figure 3.12.

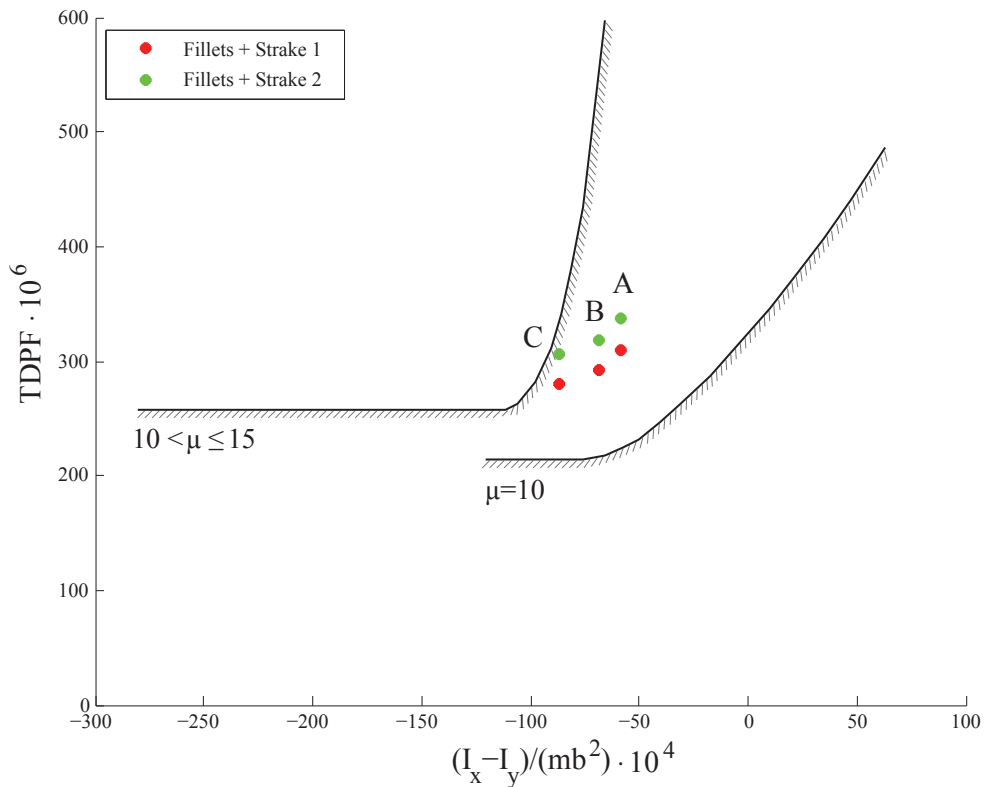


Figure 3.12: NACA spin recovery requirements for two configurations with fillets and strakes

The relative density factor computed at the altitude of 10000 ft. (~3000 m) gave the following results:

$$\mu = \frac{m}{\rho S b} = \begin{cases} 10.1 & \text{(load case A)} \\ 10.7 & \text{(load case B)} \\ 10.7 & \text{(load case C)} \end{cases}$$

The same factor has also been computed at a lower altitude of 5000 ft. (~1500m):

$$\mu = \frac{m}{\rho S b} = \begin{cases} 8.7 & \text{(load case A)} \\ 9.2 & \text{(load case B)} \\ 9.2 & \text{(load case C)} \end{cases}$$

In order for the criterion to give a positive result in terms of adequate spin recovery performance, the points on the graph, representative of the aircraft geometrical and

inertial characteristics, would need to lie above the curve corresponding to the calculated relative density factor.

Looking at the graph it can be seen that all the configurations, which gave a $TDPF \neq 0$, would produce a negative result at the altitude of 10000 ft. for which $\mu > 10$, and a positive result at 5000 ft. for which $\mu < 10$.

3.2.6 Comparison with the BK115

The same criterion for spin prediction had already been applied to the aircraft denominated BK115 for a preliminary assessment of its behavior, and was made available for a comparison. The BK115 is characterized by a lower weight and the presence of the ventral strake in its final design.

The large similarities between the two aircraft and the fact that the BK115 later exhibited a positive behavior in the incipient spin tests, makes the comparison of great interest.

In Figure 3.13 are reported the results obtained for two different load conditions of the BK115, along with the results obtained for the BK180 already shown.

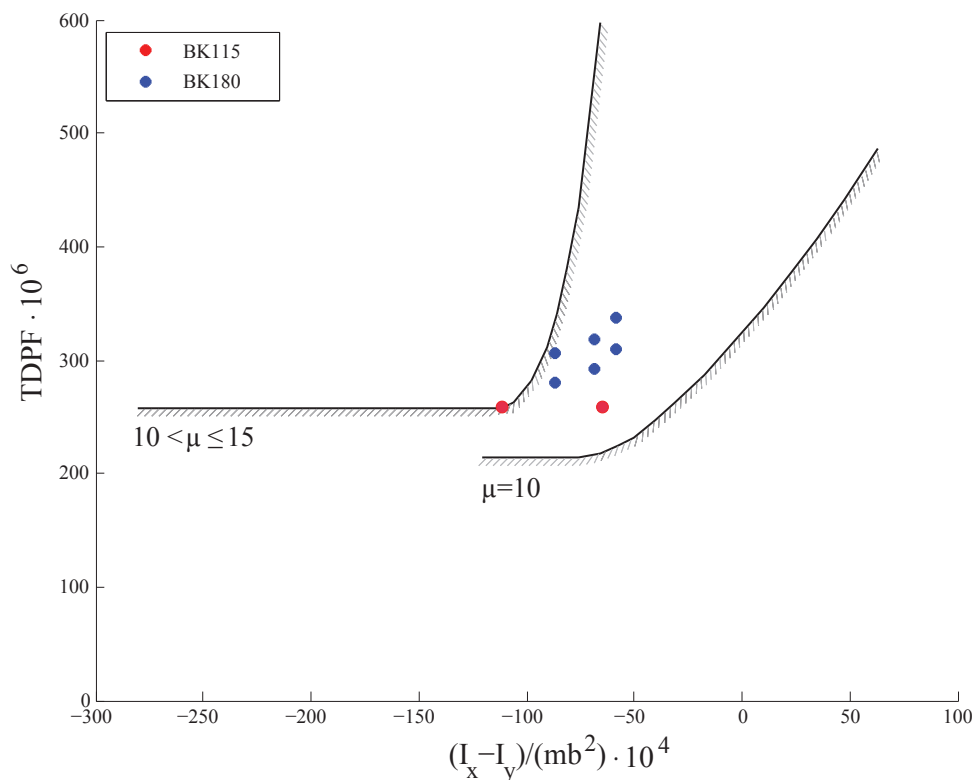


Figure 3.13: NACA method, comparison between the results for the BK180 and the BK115

The relative density factor for the BK115 was calculated for the two loading conditions shown at the two altitudes of 5000 ft. and 10000 ft.:

$$\mu = \begin{cases} 7.3 \\ 7.6 \end{cases} \quad \text{at 5000 ft.}$$

$$\mu = \begin{cases} 8.4 \\ 8.9 \end{cases} \quad \text{at 10000 ft.}$$

From the graph of the comparison it is possible to see the similarities between the two aircraft, both in terms of inertia yawing-moment and tail-damping power. Even though the TDPF for the BK115 is slightly lower, being lighter than the BK180 would mean a value of $\mu < 10$ even at 10000 ft., which would produce a satisfactory result at both altitudes considered.

3.2.7 Discussion of the results

The application of the first of the two semi-empirical methods for the evaluation of the spin behavior denoted a problem with the initial tail design. In fact the slender shape of the tail cone results in little surface area below the horizontal tail, which is considered by the criterion as being the area most effective in the damping of the spin rotation. Following the procedure, a small tail-damping ratio would produce a flatter spinning attitude, for which the whole surface of the rudder would be shielded by the stalled wake of the horizontal tail.

To improve this first negative result it was considered the installation of a ventral strake and anti-spin fillets, the combination of which produced a value of TDPF able to satisfy the requirements.

The comparison with the BK115 denoted good similarities between the two aircraft. The BK115, which is provided with a ventral strake in its final tail design, showed a good spinning behavior during the flight tests. Given this positive result and the similar outcome from this semi-empirical method, would probably mean an overall satisfactory spinning behavior also for the BK180 with a modified tail design.

3.3 Kerr criterion

3.3.1 Description

The second of the semi-empirical methods that will be illustrated and applied is defined by T. H. Kerr in Reference [7]. This method was defined on the basis of many experimental spin tests performed on full-scale aircraft in order to obtain a simplified criterion for the prediction of the spin recovery characteristics.

This criterion is based on the assumption that, for the equilibrium in a spin, the pro-spin moment due to the wing must be equal to the anti-spin moment due to the fuselage and the unshielded portion of the rudder when it is fully deflected. This equilibrium can be expressed by the following formula:

$$\bar{l}_{pb} + \bar{l}_{\zeta} + \bar{l}_{pw} = 0$$

where:

\bar{l}_{pb} is the anti-spin moment coefficient due to the body.

\bar{l}_{ζ} is the anti-spin moment coefficient due to the unshielded rudder when the rudder is deflected against the spin.

\bar{l}_{pw} is the pro-spin moment coefficient due to the wing.

If the sum of these coefficients is equal to zero there will be balance between the opposing moments and the aircraft will fail to recover from the spin. If instead their sum is positive there will be an unbalanced rolling moment coefficient (URMC) with anti-spin effect and thus the aircraft should be able to recover.

However the previous coefficients are not the only factors that determine the equilibrium in a spin and the recovery from it. The other fundamental factor taken into consideration by this method is the ratio between the pitching and the rolling moments of inertia expressed as I_y/I_x .

So the two most important parameters considered by this spin prediction method are:

$$\text{URMC} = \bar{l}_{pb} + \bar{l}_{\zeta} + \bar{l}_{pw}$$

$$1 - \frac{I_y}{I_x}$$

By plotting these two parameters one against the other it is possible to define boundaries between *pass*, *borderline* or *fail* in the recovery procedure from a spin, based on the data from spin tests on full-scale aircraft (Figure 3.14 [7]).

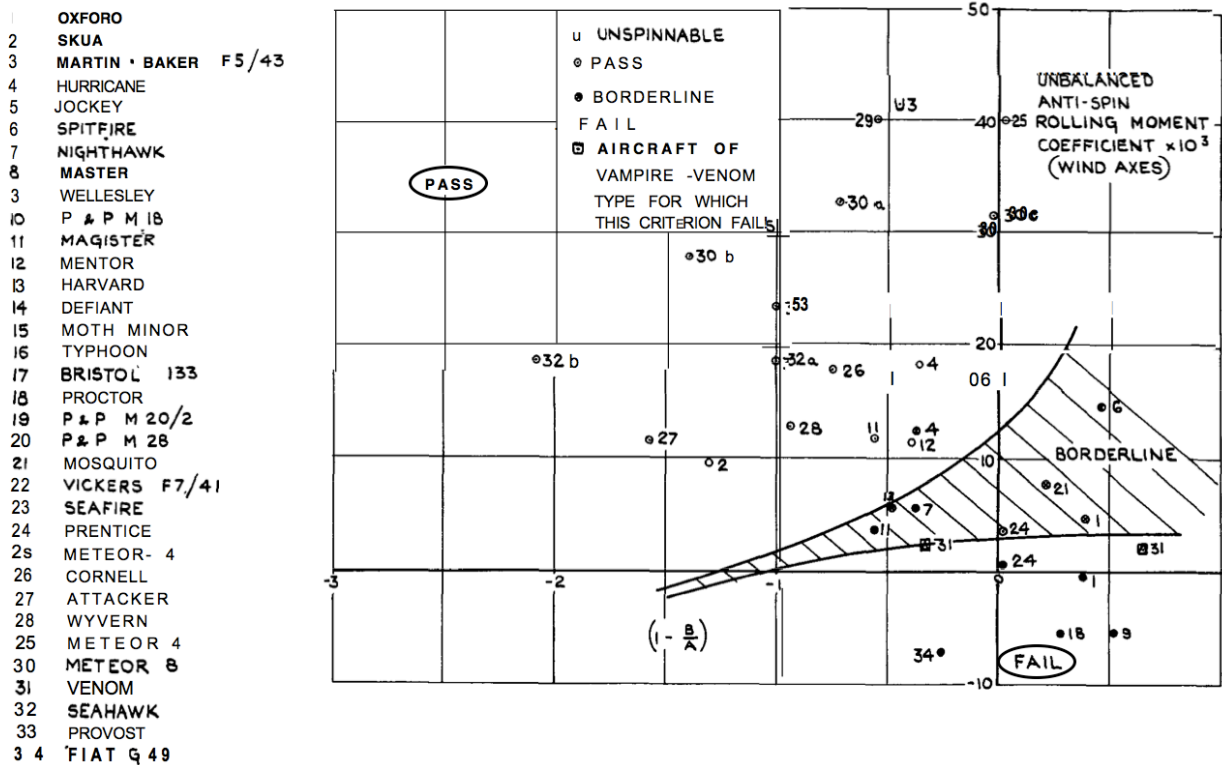


Figure 3.14: The criterion for the prediction of recovery characteristics of a spinning aircraft

To evaluate the spin recovery characteristics of a new aircraft it is only required to calculate the two parameters and compare the results with the empirical boundaries on the graph.

3.3.2 Procedure

Here will be explained in detail the complete procedure needed for the application of the method, knowing the general layout and loading of the aircraft under assessment.

The non-dimensional rotational term is estimated with the following equation:

$$\lambda = \frac{\Omega b}{2V} \approx \sqrt{\frac{1,3}{b_1 AR}}$$

in which:

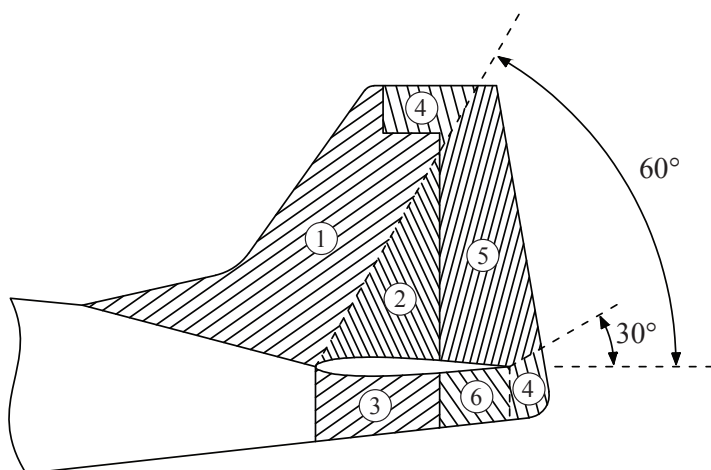
$$AR = \frac{b^2}{S}$$

$$b_1 = \frac{I_z - I_x}{\rho S \left(\frac{b}{2}\right)^3}$$

To calculate the anti-spin rolling moment coefficient due to the body, the fuselage and the vertical tail are divided into sections and the distance to the centroid of each section from the center of gravity is measured. A body damping coefficient (ϵ) is assigned to each section depending on fuselage cross-section (Table 3.11) or the portion of vertical tail considered (Figure 3.15).

Table 3.11: Values of body damping coefficient for different cross-sections of the fuselage

Body cross-section	ϵ
Circular	0.6
Rectangular	1.5
Elliptical	2.1
Round top, flat bottom	1.1
Round top, flat bottom + strakes	1.7
Round bottom, flat top	2.5
Round bottom, flat top + strakes	3.5



Tail section		ϵ
1	Fin free	+1.5
2	Fin shielded	- 0.4
3	Fin under tailplane	+3.0
4	Rudder free	+1.5
5	Rudder shielded	- 0.25
6	Rudder under tailplane	+2.0

Figure 3.15: Values of body damping coefficient for different portions of the vertical tail surface

The anti-spin rolling moment coefficient due to the body can then be calculated as follows:

$$\bar{l}_{pb} = \frac{\lambda}{Sb^2} \sum_{-l_1}^{l_2} (\epsilon h x^2 \Delta x)$$

where the terms h , x and Δx are defined in Figure.3.16.

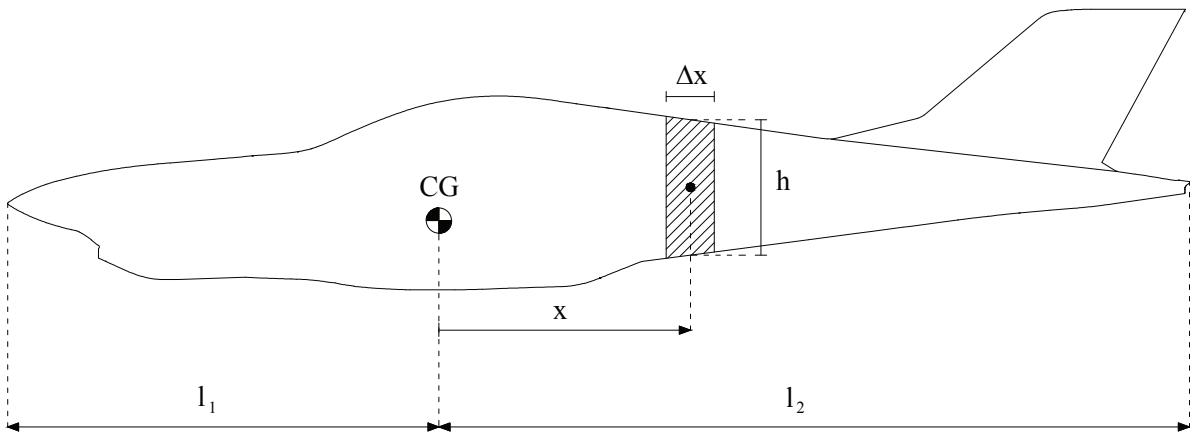


Figure.3.16: Dimensions needed for the calculation of the body rolling moment coefficient

The anti-spin moment coefficient due to the deflection of the rudder is calculated using the following formula:

$$\bar{l}_{\zeta} = \frac{S_R l_r}{Sb}$$

in which S_r is the unshielded portion of the rudder alone and l_r is the distance of its centroid from the center of gravity of the aircraft. To estimate these dimensions the angle of attack is considered 45° with a wake spread of 15° per side as shown in Figure 3.17.

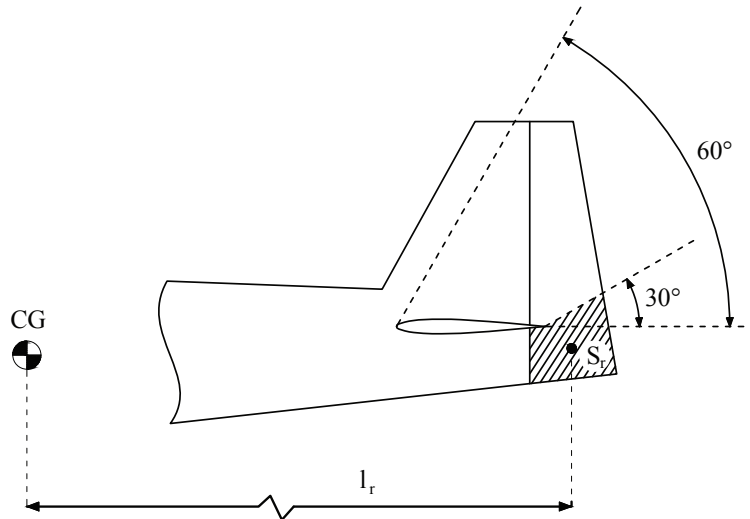


Figure 3.17: Unshielded rudder area and distance from the center of gravity

The pro-spin contribution to the rolling moment due to the wing is estimated using the graph in Figure 3.18 [7] in which the rolling moment coefficient is plotted against the rotational term λ . The curves are based on the assumption that the wing rolling moment is a function of its thickness/chord ratio.

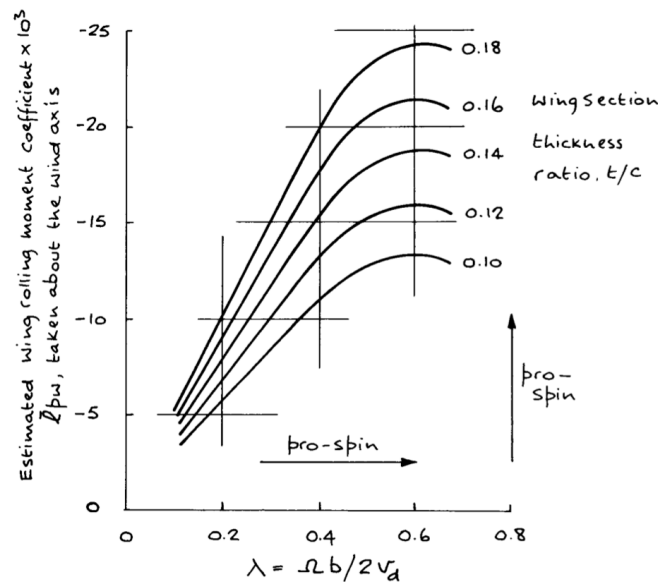


Figure 3.18: Estimation of wing rolling moment coefficient

After all the contribution for the equilibrium of the moments have been estimated, it is possible to calculate the unbalanced rolling moment coefficient and to plot it against the term $(1 - I_y/I_x)$.

By comparison with the boundary lines it is assessed whether or not the aircraft will have a satisfactory behavior in the recovery from a spin.

3.3.3 Application of the criterion

For the computation of the rolling moment coefficient due to the body, the fuselage of the aircraft was divided into 33 sections. For each section of the fuselage was measured the mean height and the distance of the centroid from the center of gravity of the aircraft. (Figure 3.19)

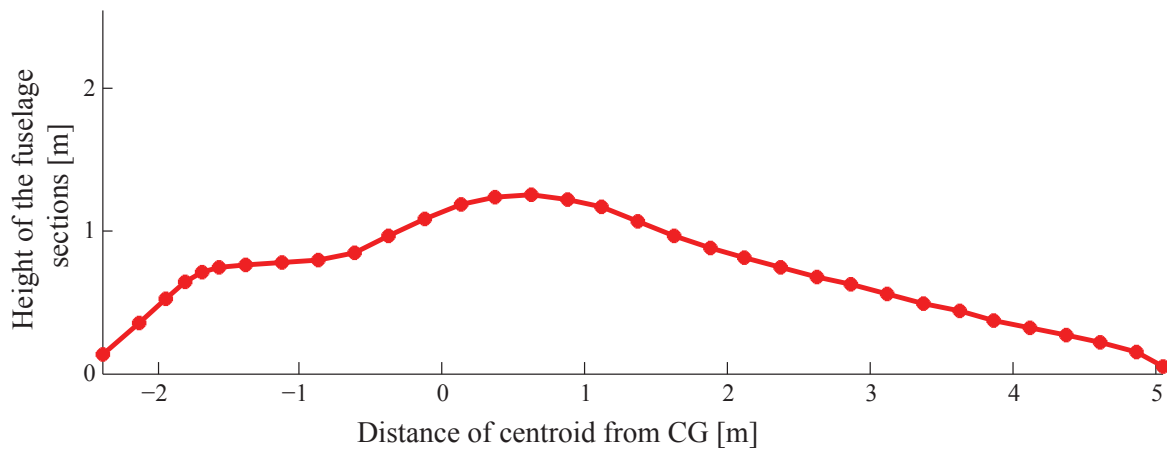


Figure 3.19: Height of fuselage sections and their distance from the CG at 28%

To each section has been assigned a value body damping coefficient based on the shape of the cross-section.

The areas of the shielded and unshielded portion of fin and rudder were measured together with the distance of their centroid from the center of gravity for each load condition. (Figure 3.20)

Their values are shown in Table 3.12.

Table 3.12: Area and distance from CG of vertical tail sections

	Area [m ²]	Distance from CG [m]			ε
		22%	28%	32%	
Fin shielded	0.2797	4.323	4.240	4.187	-0.4
Fin unshielded	0.5974	3.803	3.720	3.667	+1.5
Rudder shielded	0.5227	4.649	4.566	4.503	-0.25
Fin under tailplane	0.1169	4.279	4.196	4.143	+3.0

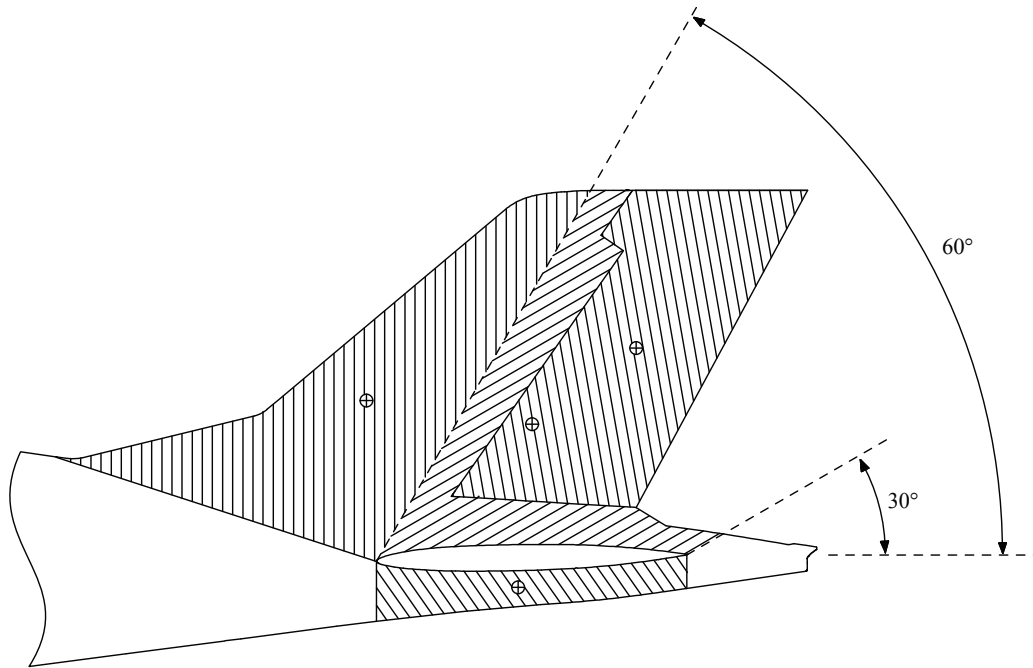


Figure 3.20: Shielded and unshielded areas of fin and rudder

The anti-spin rolling moment coefficient due to the body and vertical tail was calculated for all the load conditions:

$$\bar{I}_{pb} = \frac{\lambda}{Sb^2} \sum_{-l_1}^{l_2} (\epsilon h x^2 \Delta x) \approx \begin{cases} 18.0 \cdot 10^{-3} & \text{(load case A)} \\ 16.6 \cdot 10^{-3} & \text{(load case B)} \\ 15.9 \cdot 10^{-3} & \text{(load case C)} \end{cases}$$

The contribution of the wing was estimated through the graph shown in Figure 3.18. For the calculated value of $\lambda \approx 0.33$ and a thickness-chord ratio $t/c = 0.12$, the wing rolling moment coefficient resulted:

$$\bar{I}_{pw} \approx -11 \cdot 10^{-3}$$

The effect of the deflection of the rudder in the recovery from the spin depends from the portion of the rudder that is not in the wake of the horizontal tail as already explained.

However with the angle of attack assumed by the criterion at 45° there is no portion of the rudder outside the wake as shown in Figure 3.20. For this reason the contribution of the deflection of the rudder is zero.

$$\bar{I}_z = 0$$

It is now possible to calculate the unbalance rolling moment coefficient:

$$\text{URMC} = \bar{I}_{pb} + \bar{I}_{\zeta} + \bar{I}_{pw} \approx \begin{cases} 7.0 \cdot 10^{-3} & \text{(load case A)} \\ 5.6 \cdot 10^{-3} & \text{(load case B)} \\ 4.9 \cdot 10^{-3} & \text{(load case C)} \end{cases}$$

And plot these values on the graph that defines this criterion:

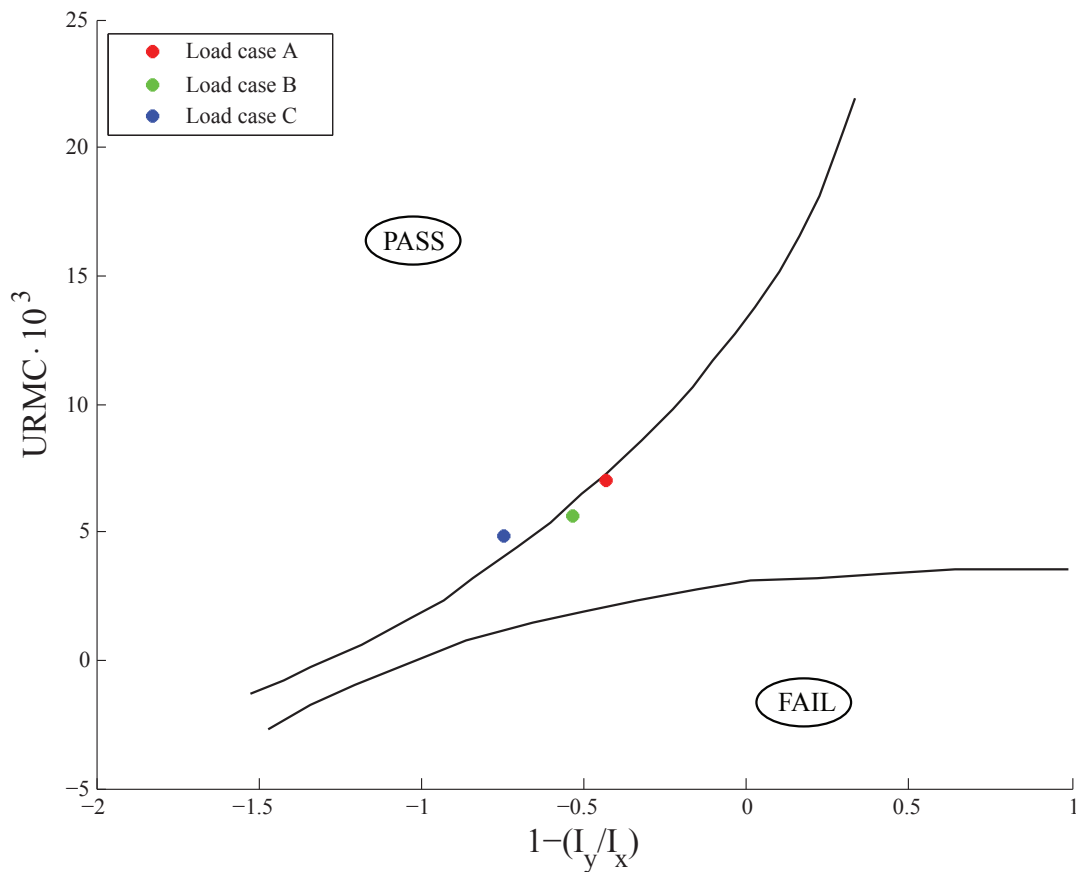


Figure 3.21: Unbalanced rolling moment coefficient for the clean configuration

As already seen for the other of the two semi-empirical methods, also in the application of the Kerr criterion was considered the possibility to improve the results with the employment of additional tail surfaces, namely a ventral strake and anti-spin fillets. The effects of these modifications to the tail design are shown in the following paragraphs.

3.3.4 Ventral strake

To be able to properly compare the results obtained from the two semi-empirical methods, the same designs for the ventral strake, described in 3.1.2, were used also for the present criterion.

In order to perform the computation, the strake was considered as an additional part of the fixed vertical tail, with the corresponding value of body damping coefficient and distance from the center of gravity.

The body moment coefficient, increased by the addition of the strake, has been calculated for all the load conditions considered and two strake designs.

The results are as follows:

- Strake 1:

$$\bar{I}_{pb} \simeq \begin{cases} 20.4 \cdot 10^{-3} & \text{(load case A)} \\ 18.8 \cdot 10^{-3} & \text{(load case B)} \\ 18.0 \cdot 10^{-3} & \text{(load case C)} \end{cases}$$

- Strake 2:

$$\bar{I}_{pb} \simeq \begin{cases} 21.0 \cdot 10^{-3} & \text{(load case A)} \\ 19.4 \cdot 10^{-3} & \text{(load case B)} \\ 18.5 \cdot 10^{-3} & \text{(load case C)} \end{cases}$$

The calculated unbalanced rolling moment coefficient:

- Strake 1:

$$\text{URMC} \simeq \begin{cases} 9.4 \cdot 10^{-3} & \text{(load case A)} \\ 7.8 \cdot 10^{-3} & \text{(load case B)} \\ 7.0 \cdot 10^{-3} & \text{(load case C)} \end{cases}$$

- Strake 2:

$$\text{URMC} \simeq \begin{cases} 10.0 \cdot 10^{-3} & (\text{load case A}) \\ 8.4 \cdot 10^{-3} & (\text{load case B}) \\ 7.5 \cdot 10^{-3} & (\text{load case C}) \end{cases}$$

The results are plotted together with the previous ones for the clean configuration for comparison:

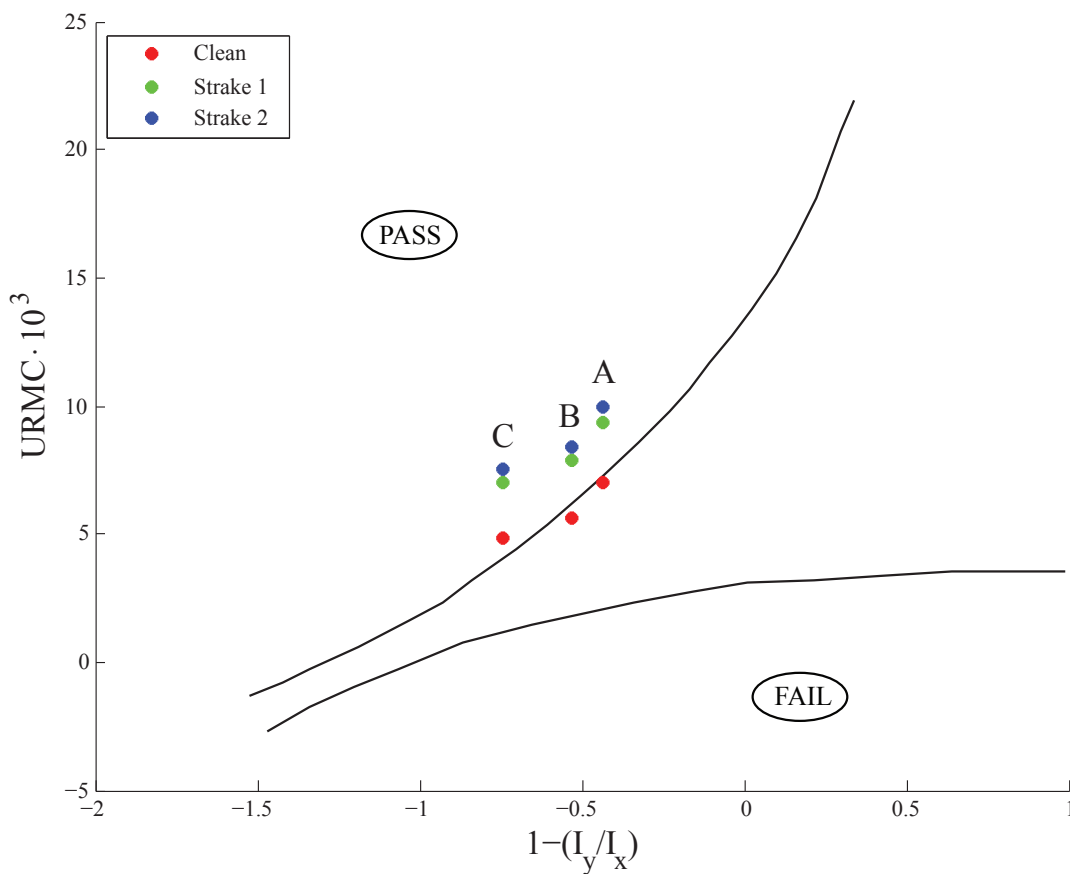


Figure 3.22: Kerr criterion with the addition of ventral strakes, comparison with the clean configuration

It is apparent from the graph how the addition of a ventral strake improved the results, and how in two of the load conditions the outcome has changed from a borderline behavior to a satisfactory recovery performance.

3.3.5 Anti-spin fillets

As already done for the ventral strake, it was considered the effect of anti-spin fillets also for this criterion.

Their effect is described in Reference [10] for the application with the NACA method. The same general concepts have been extended to the Kerr method, by considering the fixed portion of the vertical tail enlarged up to the area below the fillets, and by leaving the wake of the horizontal tail unchanged.

For the present computation, the fillets were applied to the clean tail configuration and also combined with the presence of a ventral strake. The final effect is an increase in the unbalanced rolling moment coefficient for all the configurations. The results are presented in Table 3.13 and plotted in Figure 3.23.

Table 3.13: Anti-spin moment coefficient and unbalanced rolling moment coefficient with anti-spin fillets

	$\bar{I}_{pb} \cdot 10^3$			URMC $\cdot 10^3$		
	Load A	Load B	Load C	Load A	Load B	Load C
Clean	18.9	17.5	16.7	7.9	6.5	5.7
Strake 1	21.6	19.9	19.0	10.6	8.9	8.0
Strake 2	22.4	20.7	19.8	11.4	9.7	8.8

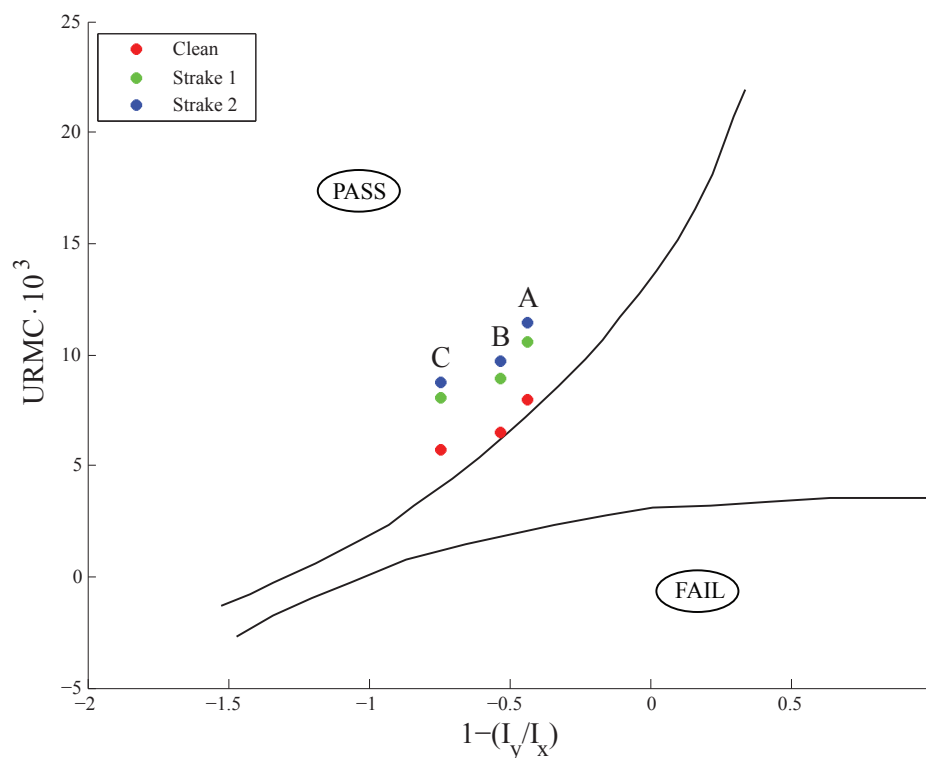


Figure 3.23: Kerr criterion with the addition of anti-spin fillets

3.3.6 Comparison with the BK115

The results obtained for the BK180 were compared with the ones for the BK115 for this second criterion as well.

In Figure 3.24 are shown the points corresponding to the clean tail configuration and the two configurations with a ventral strake for the BK180, and the two available points corresponding to two different load conditions for the BK115.

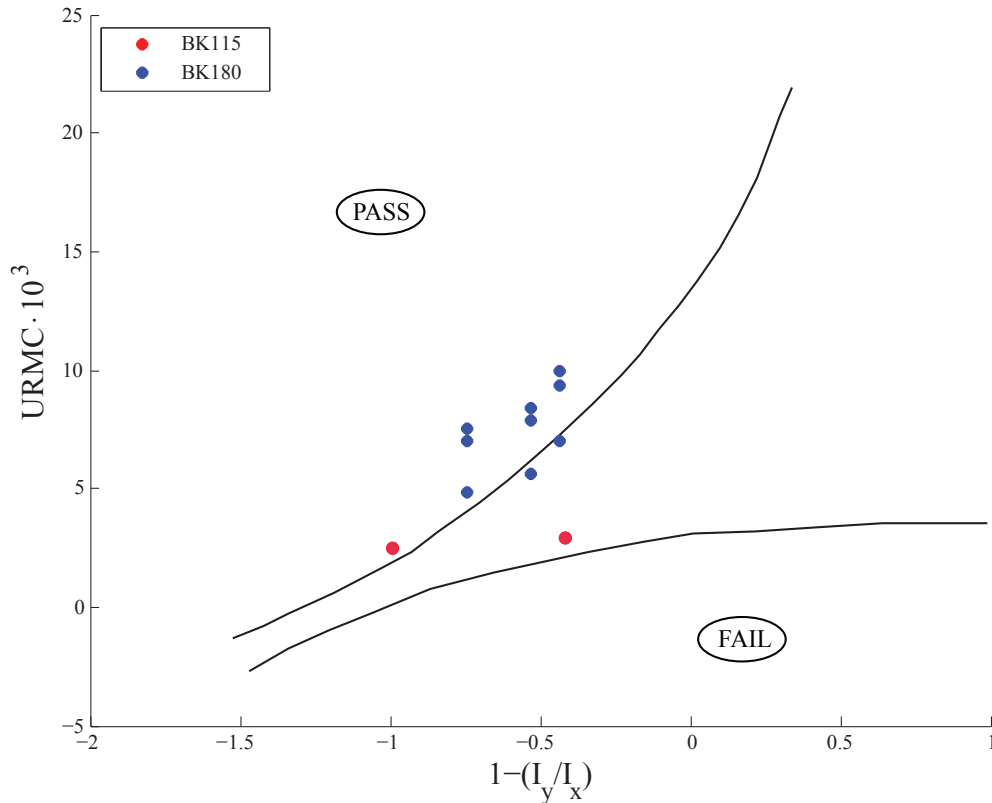


Figure 3.24: Kerr criterion, comparison between the BK180 and the BK115

The graph shows better results for the BK180 even with the clean tail configuration, for which only two of the load conditions are in the borderline region, close to the boundary with the region for satisfactory performance. All the other configurations give a positive outcome.

In comparison, only one of the configurations for the BK115 meets the requirement, while the other is close to the region for unsatisfactory behavior.

3.3.7 Discussion of the results

The results obtained by the application of the Kerr method for spin recovery prediction give generally a positive response. Even in the case in which the rudder would lose its effectiveness due to the wake of the horizontal tail, the moment produced by the tail and body alone looks to be enough to counteract the spinning rotation.

For the configurations with the clean tail design, the method does not give a definitive answer, the corresponding points being close to the boundary between positive and borderline behavior.

As expected, the addition of a ventral strake and anti-spin fillets provide some improvement, even though there is no clear evidence of the need for a modification to the original tail design.

The comparison with the BK115 denotes a slightly better outcome for the BK180, even without the addition of a strake. This result is most probably given by the increase in tail length in the BK180 design and the fact that the criterion does not take into account the increase in weight.

3.4 Concluding remarks on the semi-empirical methods

The preliminary study of the spinning behavior of the BK180 with the application of the two semi-empirical methods considered, produced results that can be considered somewhat discordant.

The NACA method heavily relies on at least a small portion of the rudder to be exposed to the free stream of air in order to produce a non-null result. To be able to meet this requirement, it was necessary to consider the combined effect of a ventral strake and anti-spin fillets, in order to extend the area below the horizontal tail. With the employment of such additional surfaces to the original tail design, it was possible to obtain a satisfactory spin recovery prediction.

The Kerr method, on the other hand, in addition to the tail configuration also considers the beneficial effect of the moment generated by the entire fuselage to oppose to the spinning rotation. As a result, the application of this method to the original tail design gave a partially positive outcome. The addition of the ventral strake and the fillets, however, improved the result by giving a more definite positive answer.

The comparison of the results obtained for the BK180 with the ones for the BK115, was considered of great relevance because of the clear similarities between the two aircraft and for the fact that the BK115 already showed a good recovery behavior during the experimental spin tests.

The NACA method showed slightly better results for the BK115, which, even if characterized by a lower value of TDPF, produced a satisfactory outcome even at the higher altitude considered, due to the lower weight of this aircraft.

The Kerr method, that does not take into account the weight, instead attributed better recovery characteristics to the BK180 for all the configurations considered.

It is notable a difference in the outcomes from the two methods, the Kerr method showing generally favorable results, while the NACA one, clearly more restrictive, needs the employment of additional tail surfaces in order to give a satisfactory prediction.

In conclusion, the limitations inherent to the semi-empirical methods are here apparent. They are able to give an approximate indication on the spin recovery capability of a new design, but their imprecise nature renders them unable to give a definitive response. In the present application, the two methods gave discordant results for the clean tail configuration, while they gave a unanimous positive outcome for the modified tail with the addition of a ventral strake and anti-spin fillets combined. There is a clear need for further, more accurate investigations before being able to give a final answer on the spin and spin recovery characteristics of the aircraft.

4 Analytical spin model

In the present and the following chapters will be presented the work that was done in order to develop an analytical flight dynamic model of an aircraft in a spin. The aim was to perform computer simulations of the complete spin maneuver from the spin entry to the recovery in order to be able to predict the spinning characteristics of the aircraft denominated BK115.

In order to be certified CS-23 under the aerobatic category, the aircraft must meet very stringent requirements for safe and prompt recovery from a fully developed spin. Since only incipient spins had been previously tested, the company showed the need for the development a computer program capable of predicting the behavior of the aircraft in a stabilized spin.

The analytical model works by the integration of the equations of motion in six degrees of freedom that describe the dynamic of the aircraft in flight.

In this chapter will be presented the complete set of equations that describe the motion of a rigid body in space, specialized for the application to an aircraft by the introduction of aerodynamic forces and moments.

4.1 Equations of motion

The analytical model implemented relies on the equations of motion in six degrees of freedom that describe the movement of a rigid body in space subject to forces and moments acting along and about three axes that are fixed with the body itself. Such axes are conventionally defined for an aircraft by the body reference frame shown in Figure 4.1.

4.1.1 Conventions

Before introducing any equation it is necessary to define the conventions for the positive direction of the axes and the rotations. All the forces and moments acting on the aircraft as well as the velocities and the angular rates are expressed in the body axes reference system. In Figure 4.1 are shown the sign conventions used.

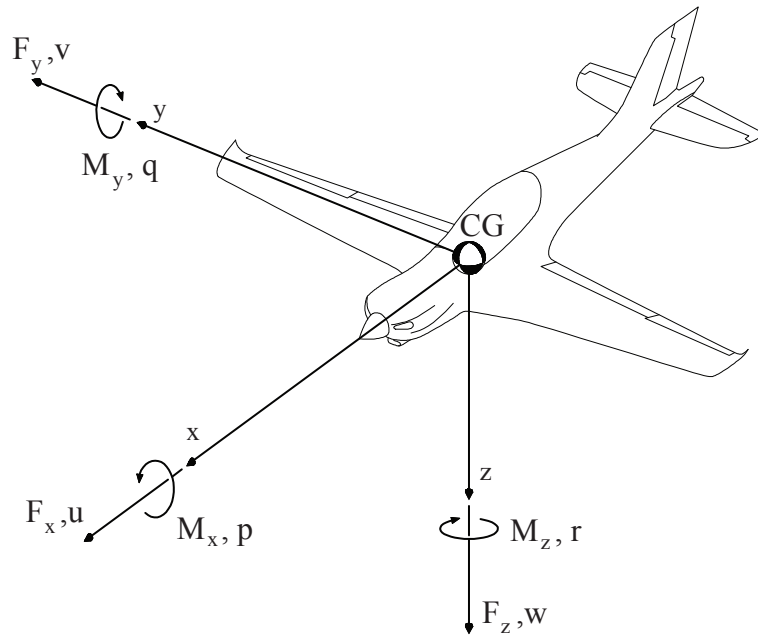


Figure 4.1: Body axes and sign conventions used

With:

$[u, v, w]$: components of the velocity along the body axes

$[F_x, F_y, F_z]$: forces acting along the body axes

$[p, q, r]$: roll, pitch and yaw rates

$[M_x, M_y, M_z]$: rolling, pitching and yawing moments

Other sign conventions that must be defined are the positive directions for the controls deflection, which are expressed in Table 4.1. For the work that will be presented in this chapter, only the three main control surfaces have been considered, leaving out flaps and trim tabs.

Table 4.1: Sign conventions for the controls deflection

Symbol	Control	Positive direction
δ_e	Elevator	Down deflection, pitch down
δ_r	Rudder	Left deflection, yaw left
δ_a	Ailerons	Right aileron up, roll right

4.1.2 Kinematic relations

To describe the aircraft attitudes and its position in space it is necessary to define a fixed reference system and the rotation matrix that describes the orientation of the body reference system with respect to the fixed one.

The fixed reference system is defined by the three axes $[X, Y, Z]$ oriented respectively towards the north, east and the center of the earth. The origin of the reference system is fixed on the surface of the earth.

The body axes frame is fixed to the aircraft and follows its movements and rotations in space. The origin is placed in the center of gravity and the three axes $[x, y, z]$ are oriented respectively towards the nose of the aircraft, the right wing and down to form a right-hand system. (Figure 4.1)

- Euler angles

The orientation of the body reference system relative to the fixed reference frame is conventionally defined by the three Euler angles $[\phi, \theta, \psi]$. By combining three consecutive rotations in the sequence 321 it is possible to bring the orientation of the fixed frame to coincide with the orientation of the body frame. This way it is possible to describe the attitudes of the aircraft with respect to the fixed frame.

Imagining the origin of the fixed frame coinciding with the center of gravity of the aircraft, the three consecutive rotations with reference to Figure 4.2 are as follows:

1. First rotation ψ about the Z axis, which brings the fixed frame into the first intermediate frame $[x_1, y_1, z_1]$.
2. Second rotation θ about the y_1 axis, which brings the first intermediate frame into the second one $[x_2, y_2, z_2]$.
3. Third and final rotation ϕ about the x_2 axis, which brings the second intermediate frame into the body frame, thus completing the transformation from the fixed reference to body axes.

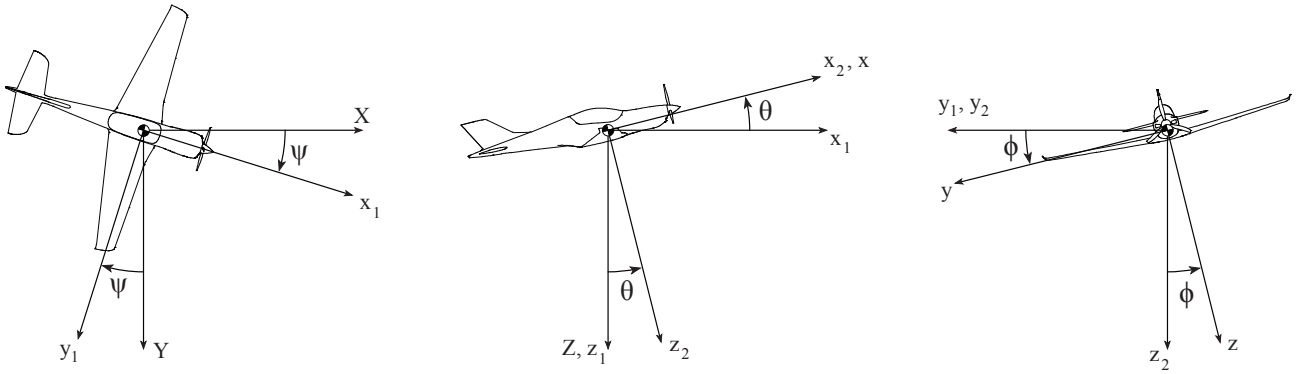


Figure 4.2: Euler angles and sequence of rotation

The overall transformation matrix from the fixed frame to the body frame is obtained by combining the three rotations in the mentioned order and has the following expression:

$$T_{fb} = \begin{bmatrix} \cos \theta \cos \psi & \cos \theta \sin \psi & -\sin \theta \\ \sin \theta \sin \phi \cos \psi - \cos \phi \sin \psi & \sin \theta \sin \phi \sin \psi + \cos \phi \cos \psi & \sin \phi \cos \theta \\ \sin \theta \cos \phi \cos \psi + \sin \phi \sin \psi & \sin \theta \cos \phi \sin \psi - \sin \phi \cos \psi & \cos \phi \cos \theta \end{bmatrix}$$

Since T_{fb} is orthogonal the inverse transformation from the body frame to the fixed frame is the transposed of the matrix:

$$\begin{aligned} T_{bf} &= T_{fb}^T = \\ &= \begin{bmatrix} \cos \theta \cos \psi & \sin \theta \sin \phi \cos \psi - \cos \phi \sin \psi & \sin \theta \cos \phi \cos \psi + \sin \phi \sin \psi \\ \cos \theta \sin \psi & \sin \theta \sin \phi \sin \psi + \cos \phi \cos \psi & \sin \theta \cos \phi \sin \psi - \sin \phi \cos \psi \\ -\sin \theta & \sin \phi \cos \theta & \cos \phi \cos \theta \end{bmatrix} \end{aligned}$$

These two rotation matrices are used to transform one reference frame into the other as needed.

The coordinates transformation from body axes to fixed axes is expressed by the following relation:

$$\begin{Bmatrix} X \\ Y \\ Z \end{Bmatrix} = T_{bf} \begin{Bmatrix} x \\ y \\ z \end{Bmatrix}$$

The transformation of the components of the velocity from body axes to the fixed reference frame can be done using the same rotation matrix used for the coordinates transformation:

$$\begin{Bmatrix} dX/dt \\ dY/dt \\ dZ/dt \end{Bmatrix} = T_{bf} \begin{Bmatrix} u \\ v \\ w \end{Bmatrix}$$

The kinematic relations for the angular velocities from the fixed frame to the body frame is expressed by the following equations:

$$\begin{cases} p = \dot{\phi} - \dot{\psi} \sin \theta \\ q = \dot{\theta} \cos \phi + \dot{\psi} \cos \theta \sin \phi \\ r = -\dot{\theta} \sin \phi + \dot{\psi} \cos \theta \cos \phi \end{cases}$$

Which can be rearranged to obtain the inverse transformation:

$$\begin{cases} \dot{\theta} = q \cos \phi - r \sin \phi \\ \dot{\phi} = p + (q \sin \phi + r \cos \phi) \tan \theta \\ \dot{\psi} = (q \sin \phi + r \cos \phi) / \cos \theta \end{cases}$$

4.1.3 Six degrees of freedom equations of motion

Once all the necessary relations have been defined, it is possible to write the equations of motion in the body axes reference system.

- Forces

$$\begin{cases} F_x = m(\dot{u} + qw - rv) \\ F_y = m(\dot{v} + ru - pw) \\ F_z = m(\dot{w} + pv - qu) \end{cases}$$

- Moments

$$\begin{cases} M_x = \dot{p}I_x + qr(I_z - I_y) - \dot{r}I_{xz} - pqI_{xz} \\ M_y = \dot{q}I_y + pr(I_x - I_z) + (p^2 - r^2)I_{xz} \\ M_z = \dot{r}I_z + pq(I_y - I_x) - \dot{p}I_{xz} + qrI_{xz} \end{cases}$$

The total forces and moments acting on the aircraft are of different nature: aerodynamic, propulsive, gyroscopic and gravitational (weight). They can be expressed in explicit form by the following equations:

$$\begin{cases} F_x = -mg \sin \theta + F_{xA} + T \\ F_y = mg \cos \theta \sin \phi + F_{yA} \\ F_z = mg \cos \theta \cos \phi + F_{zA} \end{cases}$$

Where F_{xA} , F_{yA} , F_{zA} are the components of the resultant aerodynamic force along the body axes and T is the thrust of the engine assuming the axis of thrust parallel to the longitudinal body axis.

$$\begin{cases} M_x = M_{xA} \\ M_y = M_{yA} + M_{yG} + T \cdot d \\ M_z = M_{zA} + M_{zG} \end{cases}$$

Where M_{xA} , M_{yA} , M_{zA} are the components of the aerodynamic moment acting about the body axes, M_{yG} , M_{zG} are the gyroscopic moments produced by the rotation of the propeller and d is the distance of the axis of thrust from the longitudinal axis (positive for positive values of z).

The aerodynamic forces and moments have the following expressions:

$$\begin{cases} F_{xA} = \frac{1}{2} \rho V^2 S C_{xtot} \\ F_{yA} = \frac{1}{2} \rho V^2 S C_{ytot} \\ F_{zA} = \frac{1}{2} \rho V^2 S C_{ztot} \end{cases}$$

$$\begin{cases} M_{xA} = \frac{1}{2} \rho V^2 S b C_{ltot} \\ M_{yA} = \frac{1}{2} \rho V^2 S \bar{c} C_{mtot} \\ M_{zA} = \frac{1}{2} \rho V^2 S b C_{ntot} \end{cases}$$

Where C_{xtot} , C_{ytot} , C_{ztot} , C_{ltot} , C_{mtot} , C_{ntot} are the force and moment coefficients acting along and about the body axes.

V is the flight velocity and can be written as the combination of the three velocities along the body axes:

$$V = \sqrt{u^2 + v^2 + w^2}$$

The two gyroscopic moments can be expressed as:

$$\begin{cases} M_{yG} = -J_m \omega_m r \\ M_{zG} = J_m \omega_m q \end{cases}$$

Where J_m is the moment of inertia of the propeller about its axis of rotation and ω_m is its angular velocity.

4.2 Numerical integration of the equations of motion

By rearranging the terms of the six equations of motion it is possible to obtain six of the differential equation to be integrated [16] [18].

$$\begin{cases} \dot{u} = rv - qw - g \sin \theta + \frac{F_{xA}}{m} + \frac{T}{m} \\ \dot{v} = pw - ru + g \cos \theta \sin \phi + \frac{F_{yA}}{m} \\ \dot{w} = qu - pv + g \cos \theta \cos \phi + \frac{F_{zA}}{m} \end{cases}$$

$$\begin{cases} \dot{p} = \frac{I_y - I_z}{I_x} qr + \frac{I_{xz}}{I_x} (\dot{r} + pq) + \frac{M_{xA}}{I_x} \\ \dot{q} = \frac{I_z - I_x}{I_y} pr + \frac{I_{xz}}{I_y} (r^2 - p^2) + \frac{M_{yA}}{I_y} + \frac{M_{yG}}{I_y} + \frac{T d}{I_y} \\ \dot{r} = \frac{I_x - I_y}{I_z} pq + \frac{I_{xz}}{I_z} (\dot{p} - qr) + \frac{M_{zA}}{I_z} + \frac{M_{zG}}{I_z} \end{cases}$$

The attitudes of the aircraft with respect to the fixed frame and its trajectory are obtained by the integration of the kinematic relation for the angular and linear velocities:

$$\begin{cases} \dot{\theta} = q \cos \phi - r \sin \phi \\ \dot{\phi} = p + (q \sin \phi + r \cos \phi) \tan \theta \\ \dot{\psi} = (q \sin \phi + r \cos \phi) / \cos \theta \end{cases}$$

$$\begin{pmatrix} dX/dt \\ dY/dt \\ dZ/dt \end{pmatrix} = T_{bf} \begin{pmatrix} u \\ v \\ w \end{pmatrix}$$

The last step to have a complete set of equation to be integrated in the computer simulation program is to explicit the stability and control coefficients in the expressions of the aerodynamic forces and moments:

$$\begin{cases} F_{xA} = \frac{1}{2} \rho V^2 S (C_x + C_{x\delta_e} \delta_e) \\ F_{yA} = \frac{1}{2} \rho V^2 S \left(C_{y\beta} \beta + C_{y\delta_a} \delta_a + C_{y\delta_r} \delta_r + \frac{b}{2V} (C_{yp} p + C_{yr} r) \right) \\ F_{zA} = \frac{1}{2} \rho V^2 S (C_z + C_{z\delta_e} \delta_e) \end{cases}$$

$$\begin{cases} M_{xA} = \frac{1}{2} \rho V^2 S b \left(C_{l\beta} \beta + C_{l\delta_a} \delta_a + C_{l\delta_r} \delta_r + \frac{b}{2V} (C_{lp} p + C_{lr} r) \right) \\ M_{yA} = \frac{1}{2} \rho V^2 S \bar{c} \left(C_m + C_{m\delta_e} \delta_e + \frac{\bar{c}}{2V} (C_{mq} q) \right) \\ M_{zA} = \frac{1}{2} \rho V^2 S b \left(C_{n\beta} \beta + C_{n\delta_a} \delta_a + C_{n\delta_r} \delta_r + \frac{b}{2V} (C_{np} p + C_{nr} r) \right) \end{cases}$$

Where $\delta_a, \delta_e, \delta_r$ are the deflection of the control surfaces, respectively ailerons, elevator and rudder. β is the sideslip angle and is calculated as:

$$\beta = \sin^{-1} \left(\frac{v}{V} \right)$$

All the stability and control coefficients are variable with the angle of attack, which can be calculated as follows (Figure 4.3):

$$\alpha = \tan^{-1} \left(\frac{w}{u} \right)$$

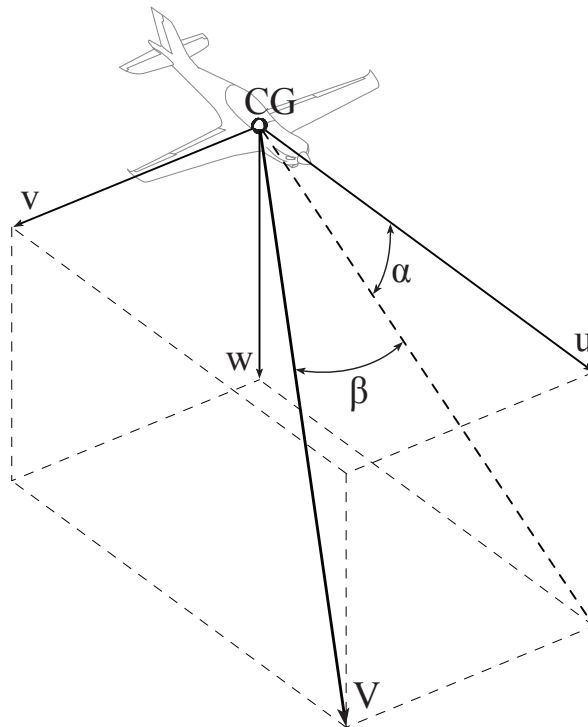


Figure 4.3: Angle of attack and sideslip angle

All the equations of motion that describe the dynamic of the aircraft have been implemented in a computer program written in Matlab code, and are numerically integrated using the ode45 function. This function is an implementation of the Runge-Kutta method for the numerical integration with a variable time step.

Given the time histories of the control inputs, the program is able to output the attitudes, positions, velocities and angular rates of the aircraft making it possible to simulate any desired maneuver.

5 Aerodynamic data-set

Beside the geometric and inertial characteristics of the aircraft, the most relevant data required for the simulation program is the complete aerodynamic data set that characterizes the aircraft. The difficulty with retrieving such aerodynamic data is given by the nature of the spin itself, which involves large angles of attack, which mean extensive regions of separated flow. In fact at spinning attitudes the aircraft is well beyond the linearity region of the aerodynamics and this makes it impossible to be able to estimate the necessary aerodynamic coefficients using only a vortex lattice method.

Conventionally the high angle of attack data set needed for the computer simulations is produced by expensive and very time-consuming wind tunnel test campaigns using also a rotary balance. For the present work however a complete data set from wind tunnel tests was not available or feasible to produce.

The aerodynamic characteristics were estimated mostly from the data gathered during the flight tests of both stabilized low angle of attack maneuvers and the incipient spin tests performed on the full-scale prototype of the aircraft BK115. The complete process that was followed is explained in more detail in the relative section.

5.1 Low angle of attack aerodynamic data

The only missing data, and possibly the most difficult to obtain, is relative to the aerodynamic characteristics of the aircraft, expressed in terms of non-dimensional coefficients. The first step to determine a complete aerodynamic data-set was to estimate the values of stability and control derivatives at low angle of attack within the region of linearity of the aerodynamics.

Where it was possible the aerodynamic characteristics were determined from the available data gathered in numerous flight tests performed on the prototype aircraft.

The aerodynamic derivatives that were not possible to be computed from the available experimental tests, were estimated using the simplified DATCOM method obtained from Ref. [12] and Ref. [13]. In Table 5.1 is shown the source of all the aerodynamic derivatives: FT for Flight Test; E for Empirical estimation.

Table 5.1: Source of the aerodynamic derivatives at low angle of attack

	C_L	C_D	C_y	C_l	C_m	C_n
α	FT	FT	×	×	FT	×
β	×	×	E	E	×	FT
p	×	×	E	FT	×	E
q	×	×	×	×	E	×
r	×	×	E	E	×	E
δ_e	FT	×	×	×	FT	×
δ_r	×	×	E	E	×	E
δ_a	×	×	×	E	×	E

5.1.1 Aerodynamic data from flight tests

- Aerodynamic center of the complete aircraft

The aerodynamic center of the aircraft was calculated from the available experimental data of trimmed flight for two different positions of the center of gravity. For each flight speed is indicated the recorded angle of deflection of the elevator needed in order to achieve longitudinal equilibrium. The data is shown in Table 5.2 and Table 5.3.

Table 5.2: Trimmed flight experimental data 1

m		712 kg
x_{CG}		18.2 % MAC
V_{eq} [m/s]	δ_{eq} [°]	α [°]
36.0	-5.6	6.5
41.2	-3.2	3.3
46.3	-1.2	1.1
51.4	-0.3	0.4
63.3	1.5	-1.8
69.4	2.4	-1.9

Table 5.3: Trimmed flight experimental data 2

m	786 kg
x_{CG}	30 % MAC
V_{eq} [m/s]	δ_{eq} [°]
38.6	-2.2
47.8	-0.33
61.7	0.9
72.0	2

For each data point it was calculated the equilibrium lift coefficient as follows:

$$C_{Leq} = \frac{2 m g}{\rho S V_{eq}^2}$$

The lift coefficients calculated for the two positions of center of gravity was then plotted against the corresponding angle of deflection of the elevator as shown in Figure 5.1. The data points were approximated by a linear curve and the slope of the interpolating curve $\frac{d\delta_{eq}}{dC_{Leq}}$ was recorded. The two values of slope corresponding to the two positions of center of gravity are shown in Table 5.4.

Table 5.4: Slope of the interpolating curve C_{Leq}-δ_{eq}

x_{CG} (% MAC)	$\frac{d\delta_{eq}}{dC_{Leq}}$ [°]
18.2	-12.6
30	-6.8

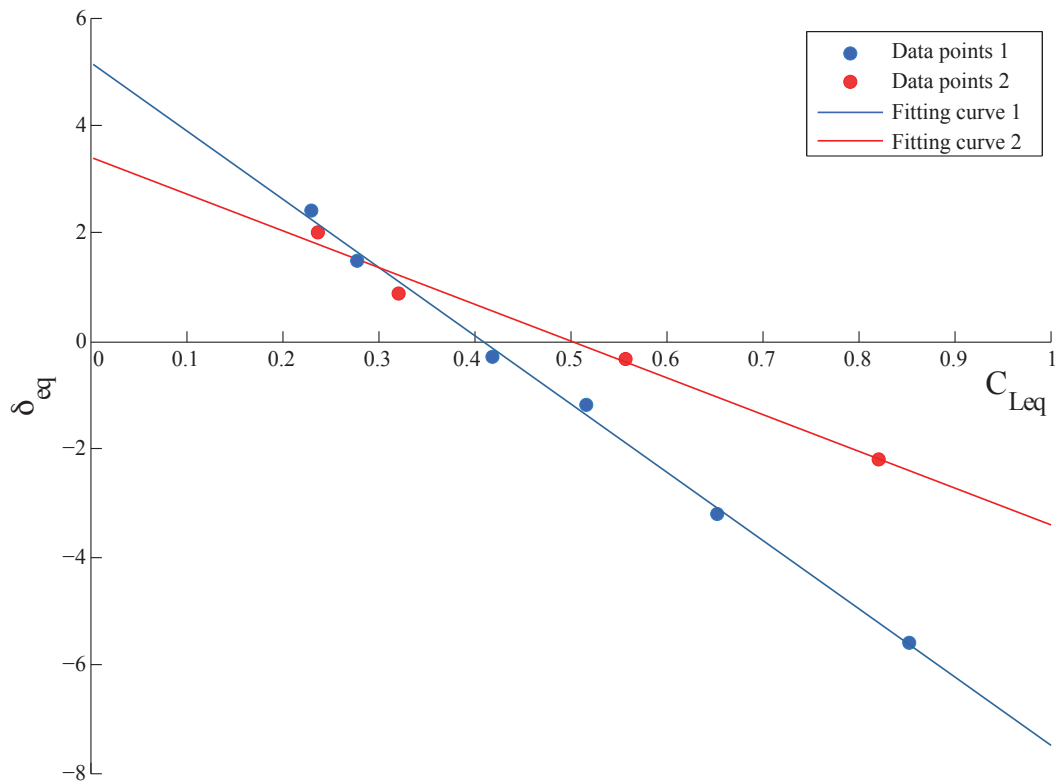


Figure 5.1: Graph of equilibrium lift coefficient against elevator deflection for two positions of center of gravity

By plotting a graph with the positions of center of gravity on the x-axis and the slopes of the interpolating curves on the y-axis it was possible to find the position of the aerodynamic center by extrapolation as shown in Figure 5.2. The aerodynamic center of the complete aircraft is found for the position of center of gravity that would give $\frac{d\delta_{eq}}{dC_{Leq}} = 0$. The calculated value is:

$$x_{AC} = 43.8 \% \text{ MAC}$$

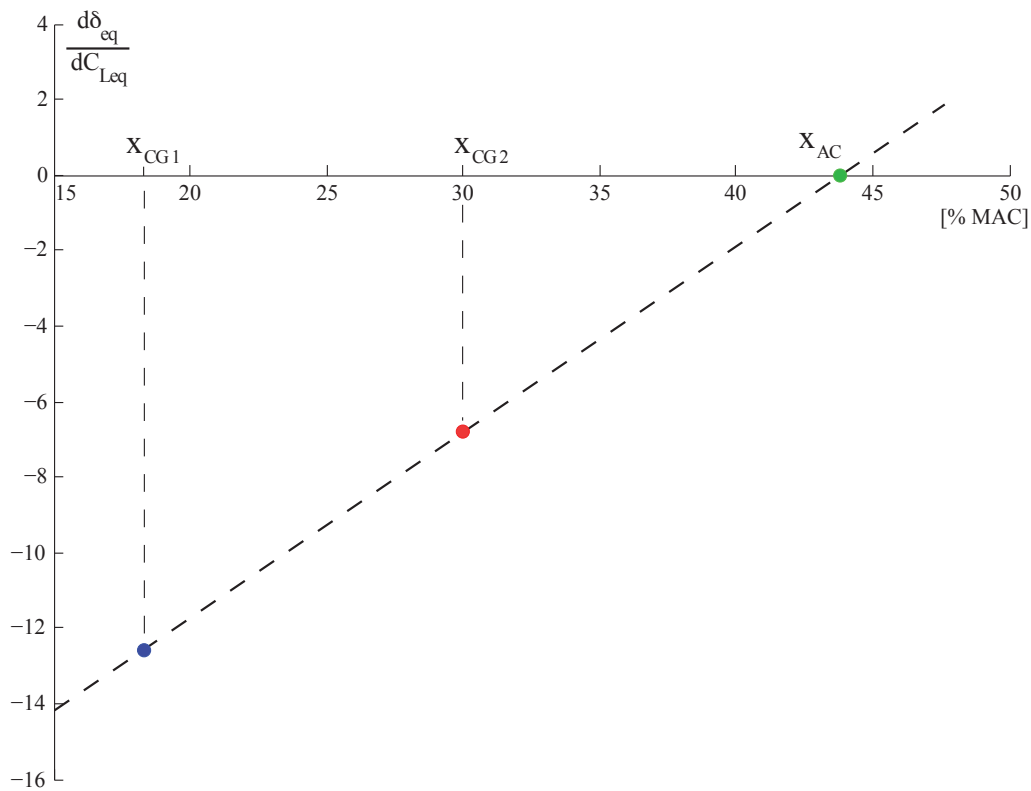


Figure 5.2: Determination of the position of the aerodynamic center

- Lift and pitching moment coefficients

In this section is explained the process that was used in order to calculate the six aerodynamic parameters needed to describe the conditions for longitudinal equilibrium of the aircraft expressed by the following two equations:

$$\begin{cases} C_{Leq} = C_{L0} + C_{L\alpha}\alpha + C_{L\delta_e}\delta_e = \frac{2 m g}{\rho S V_{eq}^2} \\ 0 = C_{m0} + C_{m\alpha}\alpha + C_{m\delta_e}\delta_e \end{cases}$$

For one set of the recorded trimmed flight data was also given the angle of attack of equilibrium as already shown in Table 5.2. Using this data it was possible to obtain a lift curve for trimmed flight $C_{Leq}-\alpha_{eq}$. By means of interpolation of the data points it was then calculated the lift coefficient for zero angle of attack and elevator deflection:

$$C_{L0} \cong 0.4$$

The lift slope coefficient was first estimated using the DATCOM method and then refined using the iterative process described in the present section. With this first estimation was also calculated the moment coefficient due to angle of attack for the configuration with the center of gravity at 18.2% MAC as follows:

$$C_{L\alpha} \cong 4.9 \frac{1}{\text{rad}}$$

$$C_{m\alpha} = C_{L\alpha} \frac{x_{CG} - x_{AC}}{\bar{c}} \cong -1.25 \frac{1}{\text{rad}}$$

By plotting the trim curve $V_{\text{eq}}-\delta_{\text{eq}}$ and interpolating it was found the equilibrium flight speed for $\delta_e=0$:

$$V_{\text{eq}}|_{\delta_e=0} \cong 53 \text{ m/s}$$

The angle of attack needed to achieve this flight condition was calculated with the first of the two equilibrium equations:

$$\alpha_{\text{eq}}|_{\delta_e=0} = \frac{C_{L\text{eq}} - C_{L0}}{C_{L\alpha}} \cong -0.07^\circ$$

With the second equilibrium equation was calculated the pitching moment coefficient for zero angle of attack:

$$C_{m0} = -C_{m\alpha} \alpha_{\text{eq}}|_{\delta_e=0} \cong -0.0016$$

At this point it was possible to calculate the lift and moment derivatives with respect to the elevator deflection for each of the experimental test points. By calculating the mean value between each test point, the two derivatives were estimated as follows:

$$C_{L\delta_e} = \frac{C_{L\text{eq}} - C_{L0} - C_{L\alpha}\alpha_{\text{eq}}}{\delta_{\text{eq}}} = 0.766 \frac{1}{\text{rad}}$$

$$C_{m\delta_e} = \frac{-C_{m0} - C_{m\alpha}\alpha_{eq}}{\delta_{eq}} = -1.399 \frac{1}{\text{rad}}$$

The only aerodynamic coefficient that wasn't extracted from experimental data at this stage was the lift curve slope. To refine its estimation were used the two theoretical formulae for $C_{L\delta_e}$ and $C_{m\delta_e}$:

$$\begin{cases} C_{L\delta_e} = \frac{S_h}{S} \frac{dC_{L_t}}{d\alpha_t} \frac{d\alpha_t}{d\delta_e} \\ C_{m\delta_e} = C_{L\delta_e} \frac{x_{CG} - x_{AC}}{\bar{c}} - \frac{dC_{L_t}}{d\alpha_t} \frac{d\alpha_t}{d\delta_e} \bar{V} \end{cases}$$

From which it was possible to calculate the value of $C_{m\delta_e}$ as a function of $C_{L\delta_e}$ as follows:

$$\begin{cases} \frac{dC_{L_t}}{d\alpha_t} \frac{d\alpha_t}{d\delta_e} = C_{L\delta_e} \frac{S}{S_h} \\ C_{m\delta_e} = C_{L\delta_e} \frac{x_{CG} - x_{AC}}{\bar{c}} - C_{L\delta_e} \frac{S}{S_h} \bar{V} = -2.382 \frac{1}{\text{rad}} \end{cases}$$

It can be seen that the two values for $C_{m\delta_e}$ calculated with these different methods exhibit a substantial discrepancy. To correct this large difference the estimated value of $C_{L\alpha}$ was adjusted in an iterative process until the two values of $C_{m\delta_e}$ would coincide with an error below 1%.

The correct values of aerodynamic coefficients found at the end of the iterative process are shown in Table 5.5 for the configuration with the center of gravity at 18.2% of the mean aerodynamic chord.

Table 5.5: Aerodynamic derivatives in the longitudinal plane for CG at 18.2% MAC

	[1/rad]	[1/°]
$C_{L\alpha}$	4.58	0.0799
$C_{m\alpha}$	-1.172	0.0205
$C_{L\delta_e}$	0.4226	0.0074
$C_{m\delta_e}$	-1.312	0.0229

The same derivatives were also calculated for the position of center of gravity at 30% of the mean aerodynamic chord.

Using these calculated values and the longitudinal equilibrium equations were then reconstructed two theoretical trim curves in order to make a comparison with the measured experimental data. The results are shown in Figure 5.3 and Figure 5.4.

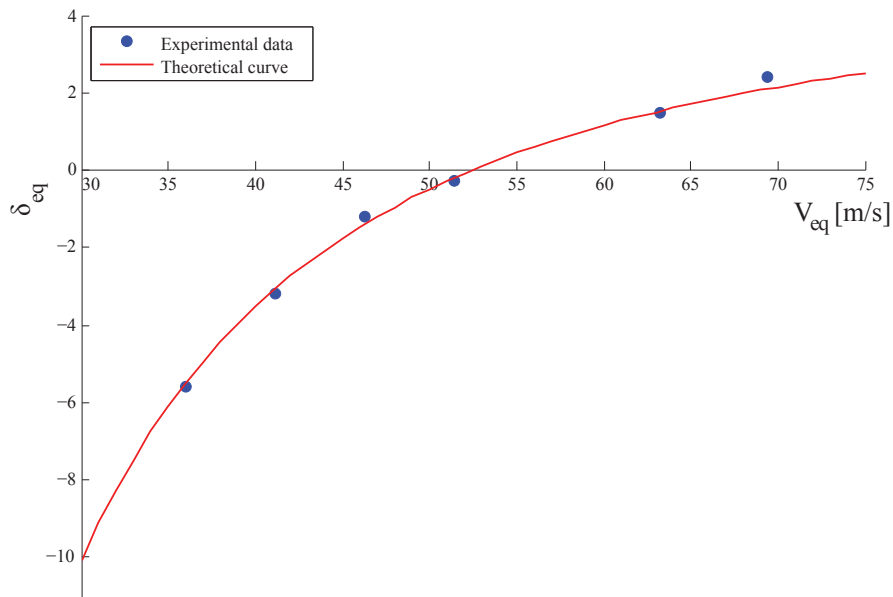


Figure 5.3: Trim curve for CG 18.2%. Comparison between experimental data and theoretical calculation

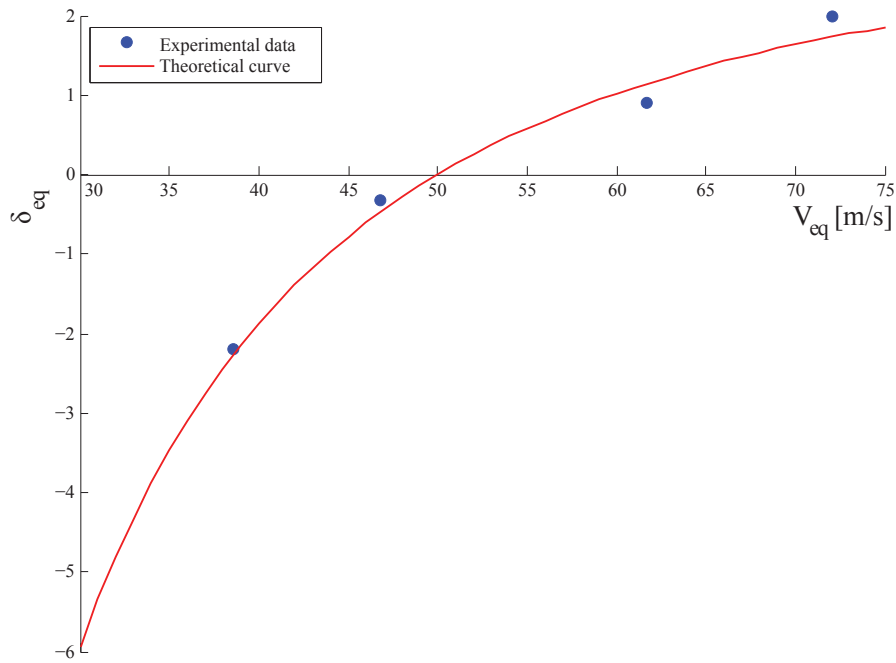


Figure 5.4: Trim curve for CG 30%. Comparison between experimental data and theoretical calculation

- Yawing moment coefficients

To be able to evaluate the yawing-moment coefficient due to rudder deflection and due to sideslip angle were analyzed the flight tests that were performed in order to assess the directional stability of the aircraft. The tests were performed by stabilizing the aircraft at the desired trim speed and slowly applying pedal force in order to establish a sideslip angle $\beta \neq 0$. For each test point were recorded both the angle of sideslip and the angle of deflection of the rudder. The data gathered from the tests are presented in Table 5.6.

The yawing-moment coefficient due to rudder deflection was calculated using the DATCOM method and the following value was obtained:

$$C_{n\delta_r} = -0.0638 \frac{1}{\text{rad}}$$

Table 5.6: Stabilized sideslip and rudder deflection from flight tests

m	786 kg	
x_{CG}	30 % MAC	
V_{eq} [m/s]	δ_r [°]	β [°]
33.4	16	10
33.4	-17	-12
36.0	18	10
36.0	-22	-15
46.3	21	10
46.3	-19	-11
63.3	13	9
63.3	-16	-6.5
72.0	-7	-6

The directional equilibrium for stabilized sideslip angle can be expressed by the following equation:

$$C_{n\delta_r} \delta_r + C_{n\beta} \beta = 0$$

From which it is possible to calculate the sideslip angle derivative from the flight test data as the mean value between all test points:

$$C_{n\beta} = -C_{n\delta_r} \delta_r \frac{1}{\beta} = 0.1025 \frac{1}{\text{rad}}$$

- Rolling moment coefficients

The rolling-moment coefficients due to roll rate and to aileron deflection were again determined from the available flight test data. The derivative with respect to the aileron deflection was already given as it was previously calculated using CFD simulations and it was indicated in the flight test report with the following value:

$$C_{l\delta_a} = 0.1828 \frac{1}{\text{rad}}$$

From the same report were taken the flight test results for stabilized roll rate measured for different mean values of aileron deflection:

Table 5.7: Stabilized roll rates from flight tests

V [m/s]	63.3
$\delta_{a_{avg}}$ [°]	p [°/s]
14	75
7	43
-8	-38
-14	-70

By writing the lateral equilibrium of the stabilized roll rate as follows:

$$C_{lp} \frac{pb}{2V} + C_{l\delta_a} \delta_a = 0$$

It is possible to calculate the rolling-moment coefficient due to roll rate as the mean value between all test points, which gave as a result:

$$C_{lp} = -C_{l\delta_a} \delta_a \frac{2V}{pb} = -0.488 \frac{1}{\text{rad}}$$

5.1.2 Aerodynamic data using the DATCOM method

All the remaining aerodynamic derivatives needed in order to complete the aerodynamic data-set of the aircraft were calculated using the simplified DATCOM method presented in Ref. [12]. In order to be able to correctly estimate the values of these derivatives it was necessary to measure many geometric dimensions of the aircraft, which was done using the three view CAD drawings. All the measurements obtained needed to perform the calculations are presented in Table 5.8 through Table 5.12.

Table 5.8: Wing geometric data used with the DATCOM method

Wing geometric data			
S	10.31	[m ²]	Wing area
\bar{c}	1.36	[m]	Mean aerodynamic chord
b	9	[m]	Wing span
AR	7.86	[-]	Aspect ratio
t/c	12%	[-]	Wing thickness-chord ratio
Γ	4°	[°]	Dihedral angle
c_{root}	1.86	[m]	Root chord
c_{tip}	0.62	[m]	Tip chord
$c_{\text{tip}}/c_{\text{root}}$	0.33	[-]	Taper ratio
$\Lambda_{c/2}$	-3°	[°]	Sweep angle at 1/2 chord
$\Lambda_{c/4}$	1°	[°]	Sweep angle at 1/4 chord
ϵ_t	-3°	[°]	Twist angle
c_a	0.198	[m]	Aileron mean chord
b_a	1.68	[m]	Aileron span
S_a	0.34	[m ²]	Aileron surface area

Table 5.9: Horizontal tail geometric data used with the DATCOM method

Horizontal tail geometric data			
S_h	2.36	[m ²]	Horizontal tail area
\bar{c}_t	0.773	[m]	Horizontal tail mean aerodynamic chord
l_t	3.79	[m]	Horizontal tail arm
S_e	0.733	[m ²]	Elevator area
c_e	0.265	[m]	Elevator mean chord
\bar{V}	0.636	[-]	Tail volume coefficient
b_t	3.04	[m]	Horizontal tail span
AR_t	3.9	[-]	Aspect ratio
c_e/c_t	0.36	[-]	Chord ratio (elevator/HT)

Table 5.10: Vertical tail geometric data used with the DATCOM method

Vertical tail geometric data			
S_v	1.50	[m ²]	Vertical tail area
l_v	3.53	[m]	Vertical tail arm
Z_v	0.58	[m]	Distance of the center of pressure to the fuselage axis
b_v	1.16	[m]	Vertical tail span
c_{vroot}	1.87	[m]	Root chord
c_{vtip}	0.71	[m]	Tip chord
\bar{c}_v	1.38	[m]	Mean aerodynamic chord
c_r/c_v	0.45	[-]	Chord ratio (rudder/VT)
$\Lambda_{c/2}$	47°	[°]	Sweep angle at ½ chord
$\Lambda_{c/4}$	53°	[°]	Sweep angle at ¼ chord
AR_v	0.897	[-]	Aspect ratio
S_r	0.521	[m ²]	Rudder surface area
b_r	0.99	[m]	Rudder span
c_r	0.51	[m]	Rudder mean chord

Table 5.11: Fuselage geometric data used with the DATCOM method

Fuselage geometric data			
l_f	7.23	[m]	Fuselage length
h_{max}	1.25	[m]	Fuselage maximum height
w_{max}	0.83	[m]	Fuselage maximum width
S_B	5.2	[m ²]	Fuselage side area
$S_{f_{ave}}$	0.27	[m ²]	Mean cross-section area

Table 5.12: Ventral strake geometric data used with the DATCOM method

Ventral strake geometric data			
S_s	0.18	[m ²]	Ventral strake area
b_s	0.20	[m]	Ventral strake span
l_s	3.90	[m]	Ventral strake arm
Z_s	-0.23	[m]	Distance from the center of pressure to the fuselage axis

5.1.3 Summary low angle of attack aerodynamic coefficients

All the values of the stability and control aerodynamic derivatives at low angle of attack calculated for the position of center of gravity at 25% MAC are here summarized:

Table 5.13: Low α aerodynamic derivatives for CG at 25% MAC

	[1/rad]	[1/°]
$C_{L\alpha}$	4.58	0.079936
$C_{m\alpha}$	-0.861	-0.015027
$C_{l\beta}$	-0.0379	-0.000661
$C_{n\beta}$	0.1025	0.001789
$C_{y\beta}$	-0.387	-0.006754
C_{lp}	-0.488	-0.008517
C_{np}	-0.007	-0.000122
C_{yp}	-0.022	-0.000384
C_{mq}	-14	-0.224346
C_{lr}	0.0994	0.001735
C_{nr}	-0.08	-0.001396
C_{yr}	0.156	0.002723
$C_{L\delta_e}$	0.4226	0.007376
$C_{m\delta_e}$	-1.257	-0.021939
$C_{l\delta_r}$	0.009	0.000157
$C_{n\delta_r}$	-0.0638	-0.001114
$C_{y\delta_r}$	0.070	0.001222
$C_{l\delta_a}$	0.1828	0.003190
$C_{n\delta_a}$	-0.0006	-0.000011
$C_{y\delta_a}$	0	0

5.2 High angle of attack aerodynamic data

In order to be able to simulate the spin maneuver it was necessary to determine the values of all the aerodynamic coefficients up to high angles of attack. This is needed because this specific maneuver is characterized by angles of attack beyond the stall region.

The process to estimate the post stall characteristics of the aircraft was quite long and difficult. The starting point was to gather all the possible data regarding aerodynamic coefficients up to high angle of attack for other aircraft with similar geometric characteristics. This kind of data is usually produced by very extensive tests campaigns in a wind tunnel. Since this campaigns can be very long and expensive they are usually done on military aircraft and that is the reason why it was not possible to find such data regarding a general aviation aircraft.

The aerodynamic data that was considered in this section is mainly from two military training jet aircraft: the Italian Macchi MB339 and the Chinese Hongdu JL-8 for which it was possible to obtain a complete aerodynamic data set. Even if these two aircraft have characteristics that differ a lot from the aircraft under study, mainly due to the higher weight and the jet propulsion, these factors are not of great influence in the aerodynamics during a spin where the engine is maintained at idle regime. On the other hand the geometric characteristics of the un-swept wing and the traditional tail configuration have many similarities with the aircraft that is being analyzed.

Each of the aerodynamic coefficients from the available sets of data was non-dimensionalized with the corresponding value at low angle of attack, and its trend up to high angles of attack was recorded. This way it was possible to gather information about the possible behaviors of the coefficients beyond the stall region independently from their value at low angle of attack. An example of the different tendencies of aerodynamic coefficients curves beyond the linearity region is shown in Figure 5.5, extracted from Reference [19].

Starting from the values at low angle of attack calculated previously it was possible to estimate the values at higher α for each of the aerodynamic coefficients, based on the trends of the curves and the spin tests performed on the aircraft prototype. This was an iterative process in which the results of the computer simulations were compared to the flight tests results and each time one or more of the aerodynamic coefficients were carefully adjusted before proceeding to a new simulation. The process of determination of the complete aerodynamic data set ended when the predicted behavior obtained with the computer simulation matched closely with the recorded data from the flight tests.

the flight speed. The time histories for these data are shown in the following figures for the maneuver considered.

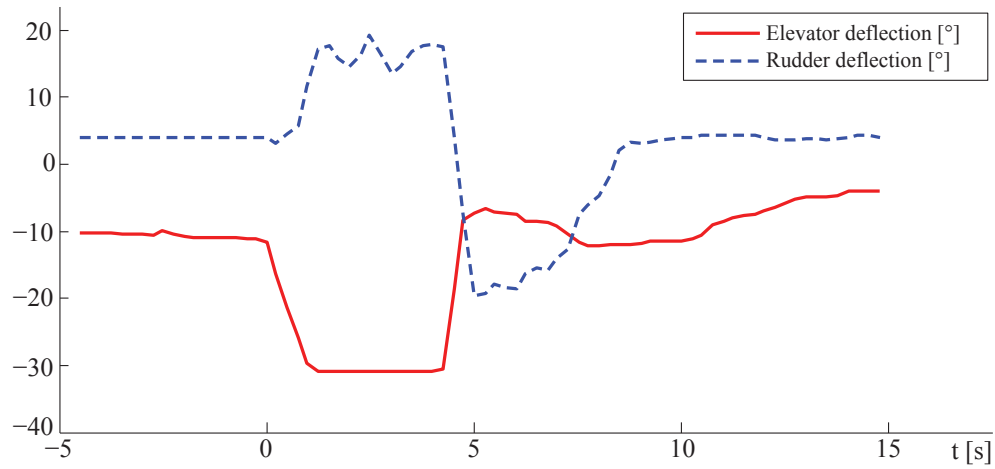


Figure 5.6: Time histories of controls deflection, spin 1

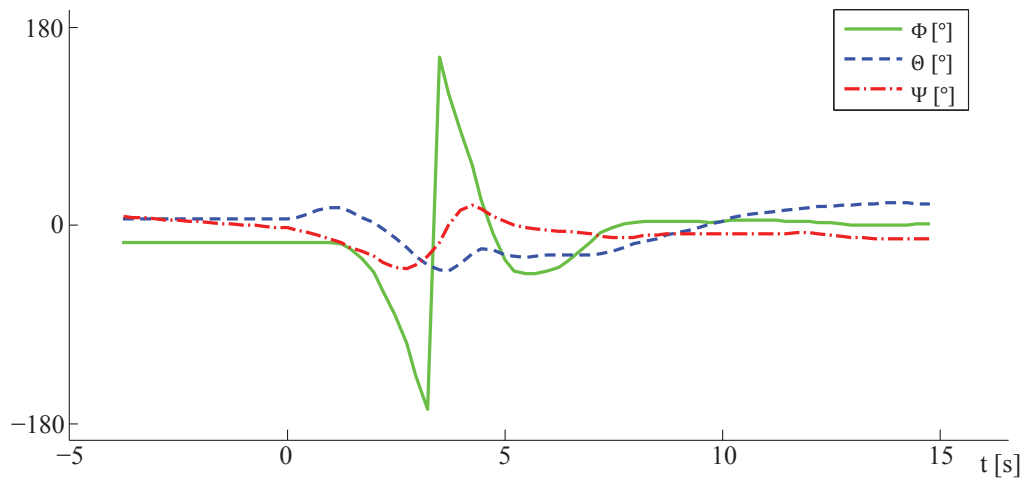


Figure 5.7: Time histories of aircraft attitudes, spin 1

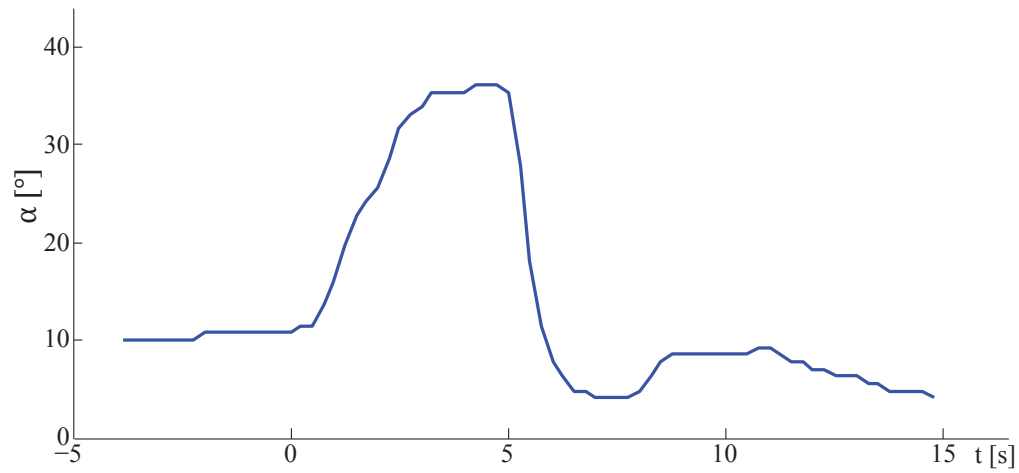


Figure 5.8: Time history of angle of attack, spin 1

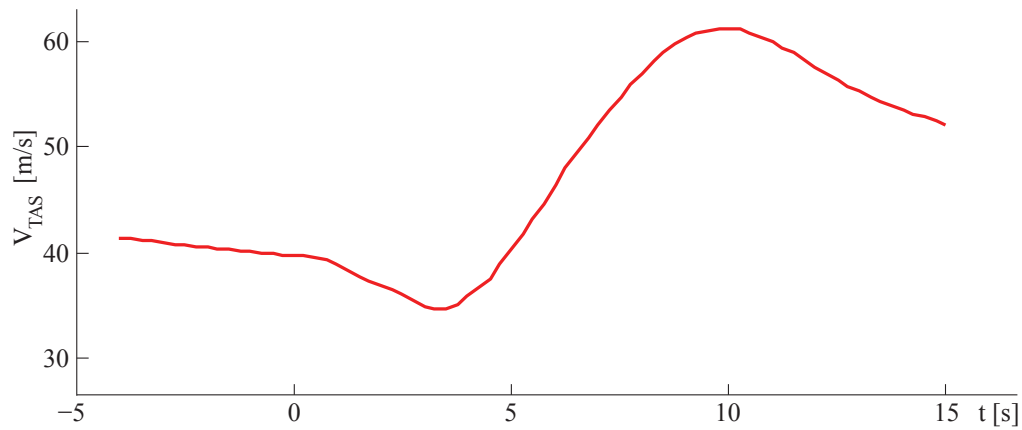


Figure 5.9: Time history of flight speed, spin 1

Given the time histories from the flight test it was possible to define the inputs of the elevator and the rudder deflections for the numerical simulations, as well as the initial conditions in terms of attitude, angle of attack and flight speed at the spin entry. The control inputs were modeled as shown in Figure 5.10.

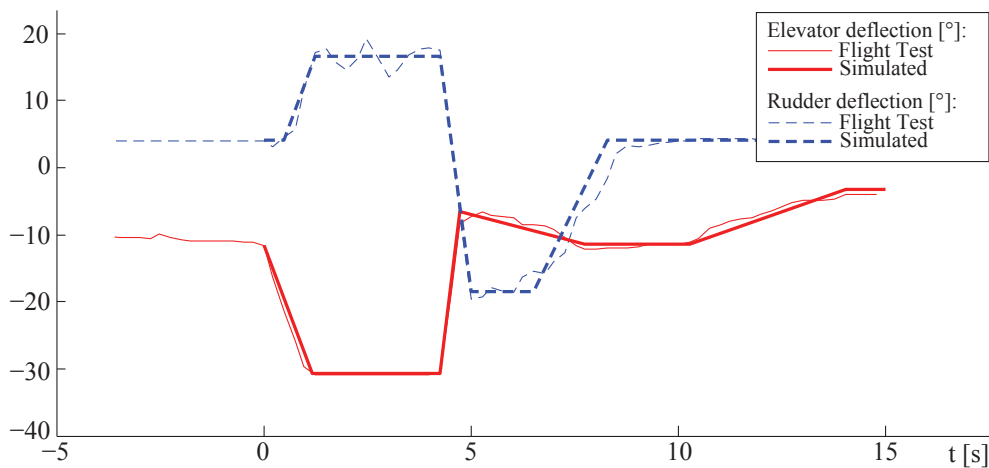


Figure 5.10: Control deflection inputs used in the simulation, comparison with the time histories from flight test, spin 1

Other known characteristics needed for the simulations are the inertial properties of the aircraft expressed in Table 5.14 as well as the initial altitude of 10000 ft. The air density was modeled as a function of the altitude using the equations of the international standard atmosphere.

Table 5.14: Inertial properties of the aircraft used in the simulations

m [kg]	712
I_x [kgm^2]	850
I_y [kgm^2]	1217
I_z [kgm^2]	1987
I_{xz} [kgm^2]	~ 0

By performing numerous simulations maintaining the same control inputs and initial conditions and by carefully adjusting the trends of the aerodynamic coefficients at high angle of attack it was possible to obtain a simulation that closely matched the behavior of the aircraft in the flight test. To do so were taken in consideration both the amplitudes and the frequencies of the simulated quantities, mainly the aircraft attitudes and the angle of attack, in order to best represent the spinning behavior of the aircraft shown in the flight tests.

The final result of these simulations is shown in the following figures as a comparison between the recorded time histories of the flight test and the time histories obtained as output of the simulation.

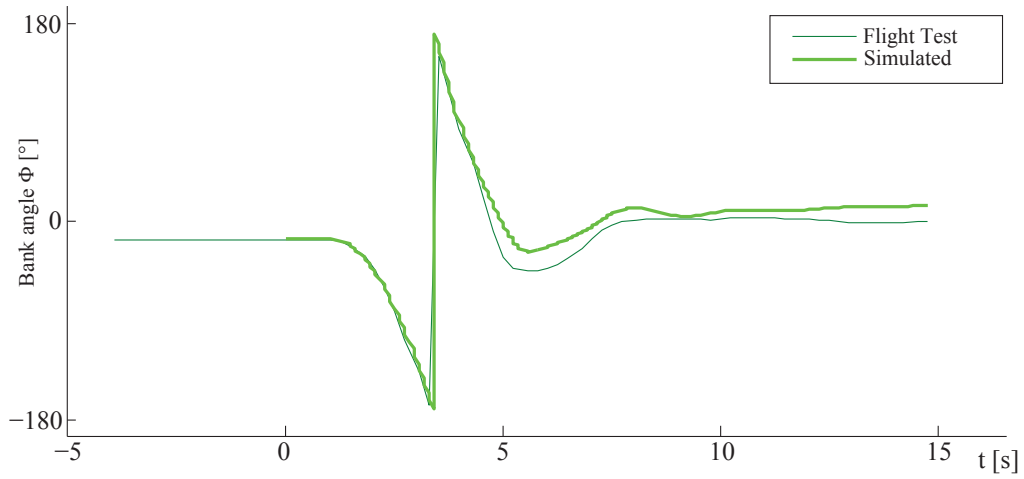


Figure 5.11: Bank angle, comparison between flight test and simulation output

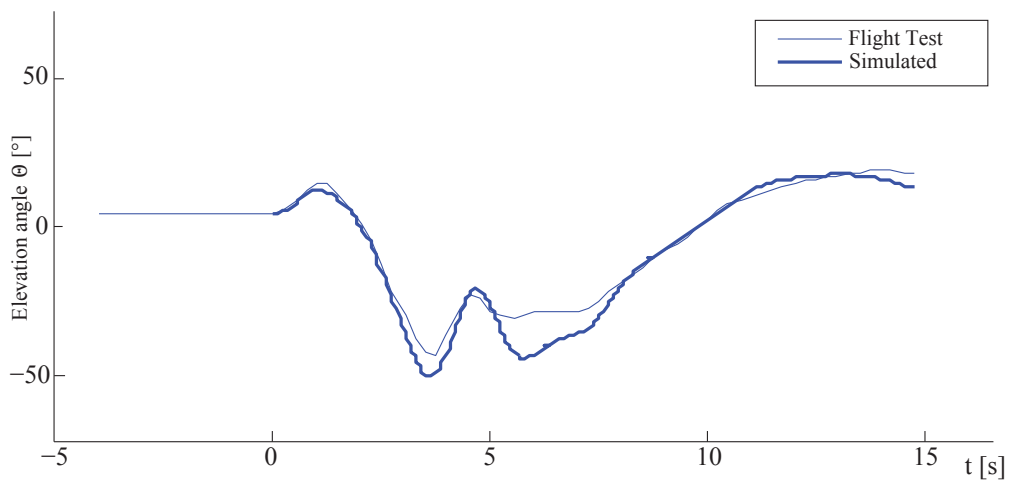


Figure 5.12: Elevation angle, comparison between flight test and simulation output

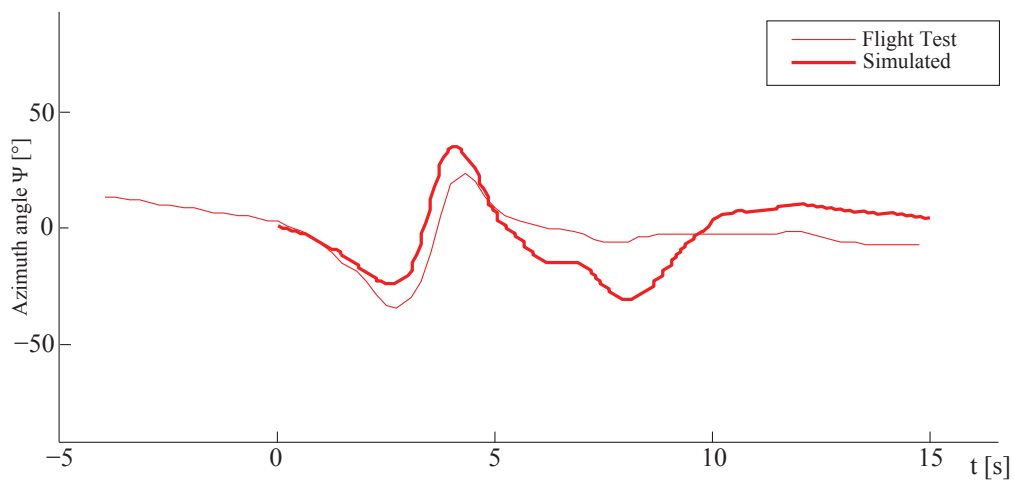


Figure 5.13: Azimuth angle, comparison between flight test and simulation output

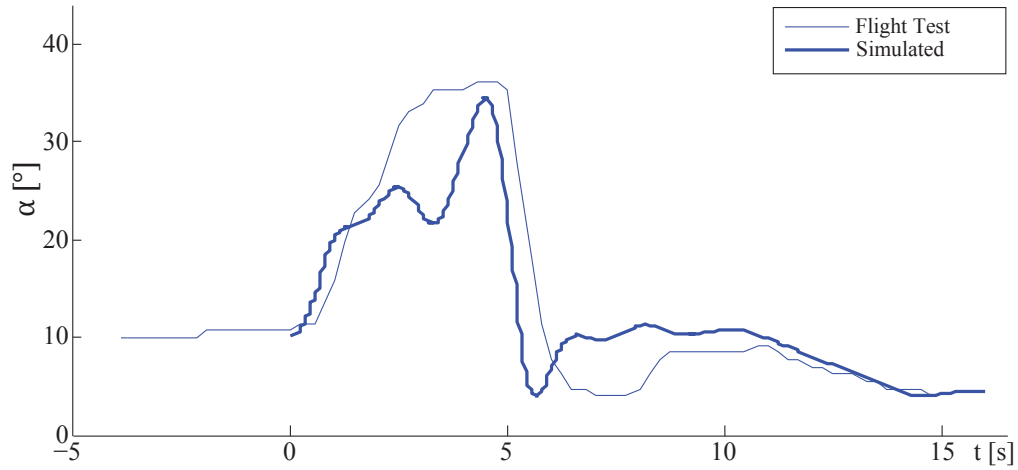


Figure 5.14: Angle of attack, comparison between flight test and simulation output

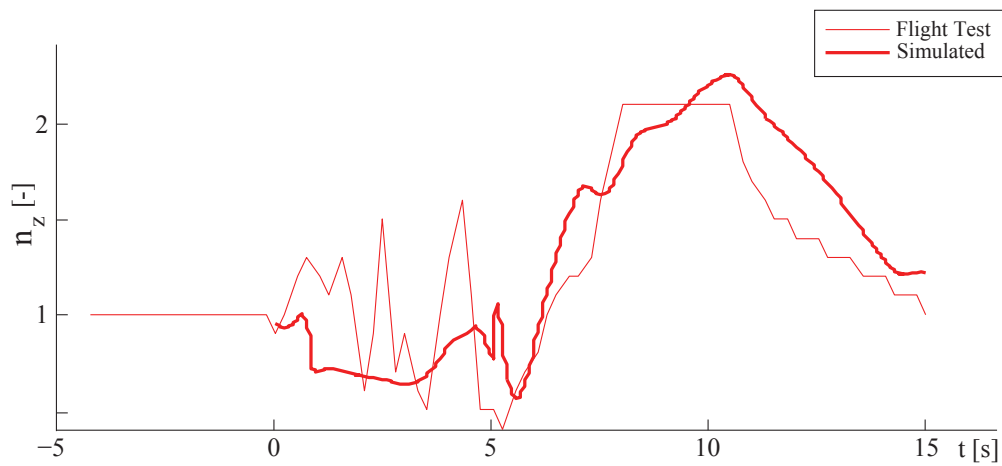


Figure 5.15: Load factor, comparison between flight test and simulation output

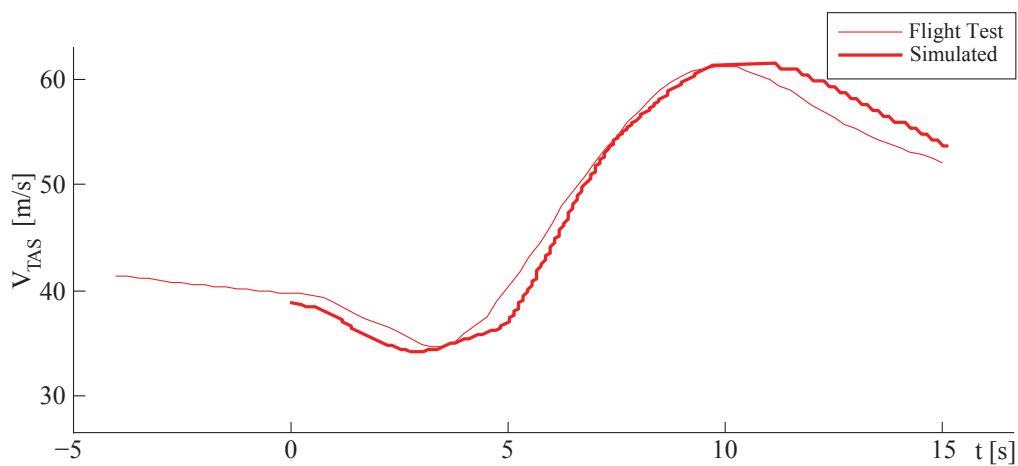


Figure 5.16: Flight speed, comparison between flight test and simulation output

5.3 Model validation

In order to validate the analytical spin model, two additional simulations were performed for two more test points available in the recorded flight tests. This time no changes were made to the model to be able to determine whether it was able to satisfactorily simulate the behavior of the aircraft in a spin with different control inputs and initial conditions.

The comparisons between the time histories from the flight tests and the inputs and outputs of the simulations are shown in the following figures.

- Spin 2

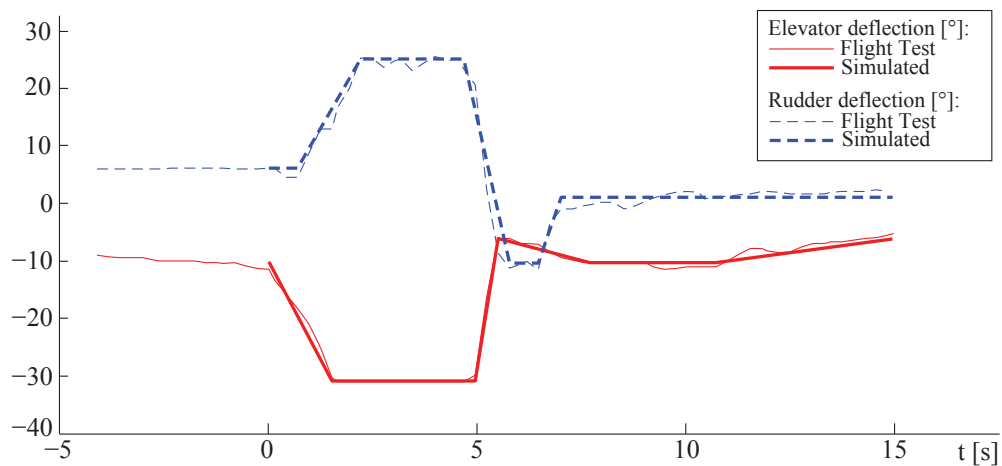


Figure 5.17: Control deflection, comparison between flight test and simulation input, spin 2

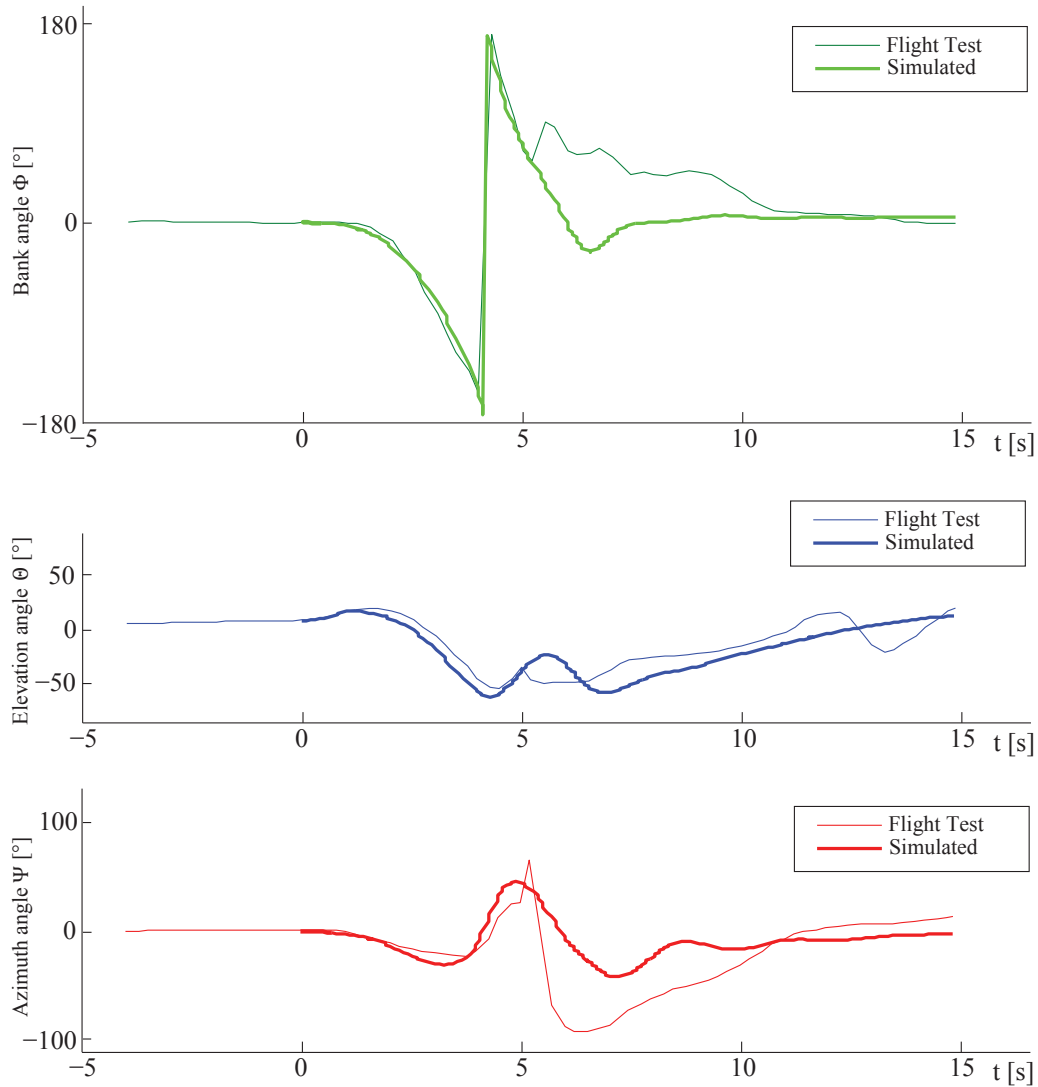


Figure 5.18: Aircraft attitudes, comparison between flight test and simulation output, spin 2

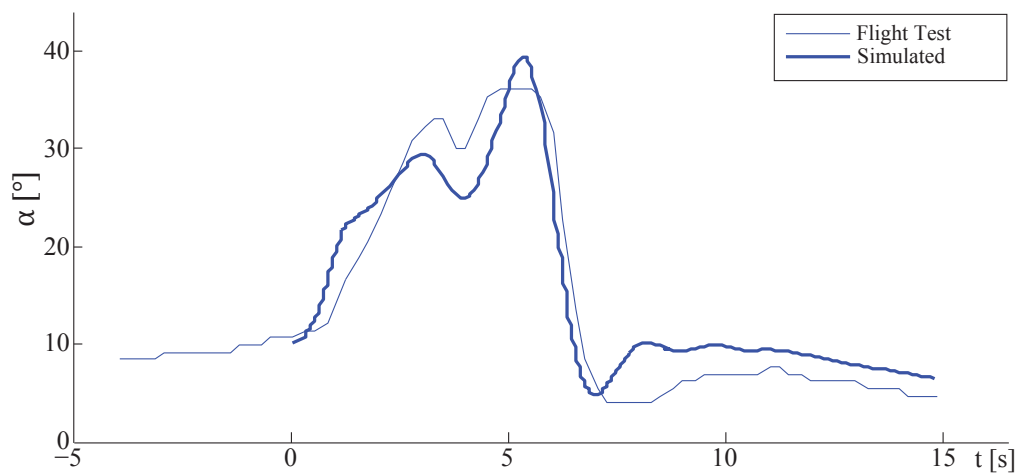


Figure 5.19: Angle of attack, comparison between flight test and simulation output, spin 2

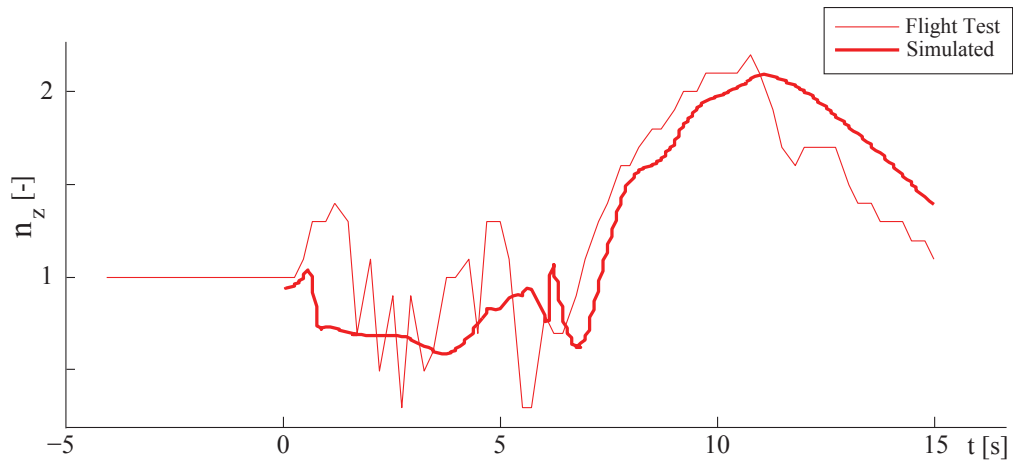


Figure 5.20: Load factor, comparison between flight test and simulation output, spin 2

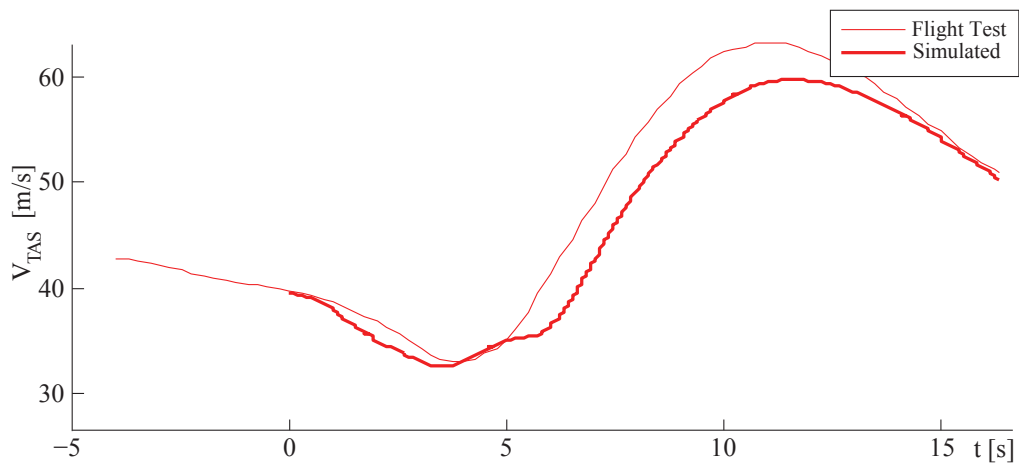


Figure 5.21: Flight speed, comparison between flight test and simulation output, spin 2

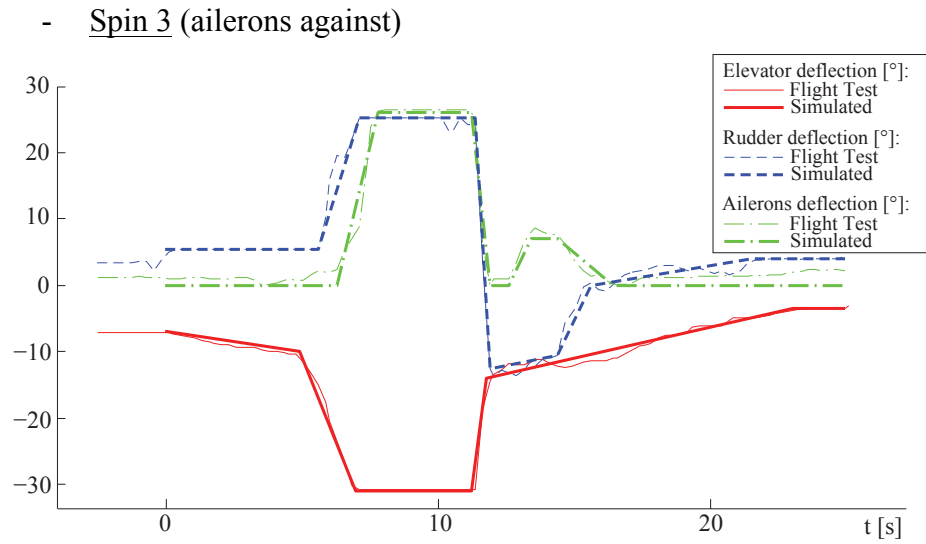


Figure 5.22: Control deflection, comparison between flight test and simulation input, spin 3

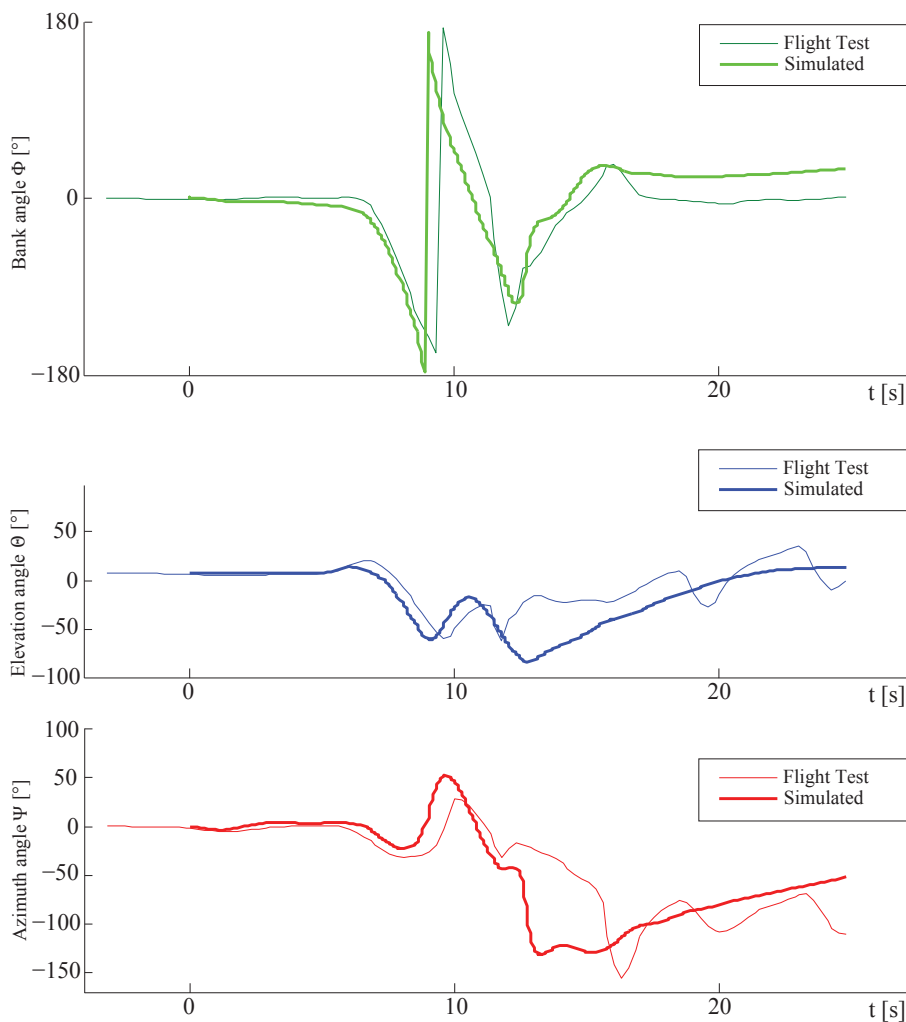


Figure 5.23: Aircraft attitudes, comparison between flight test and simulation output, spin 3

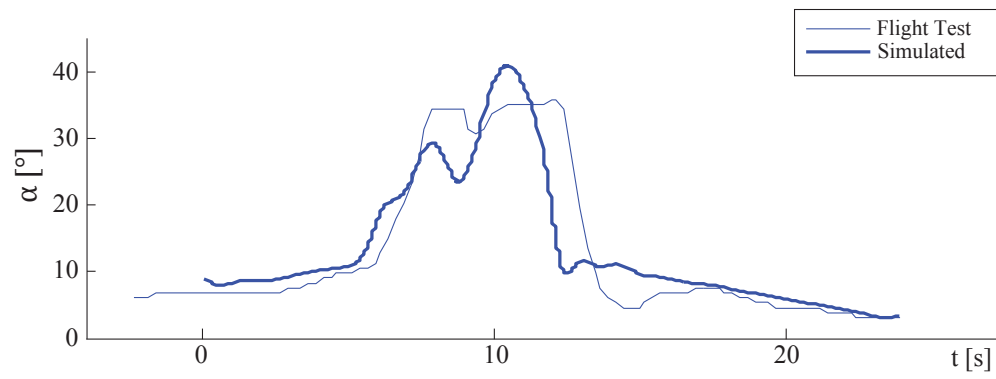


Figure 5.24: Angle of attack, comparison between flight test and simulation output, spin 3

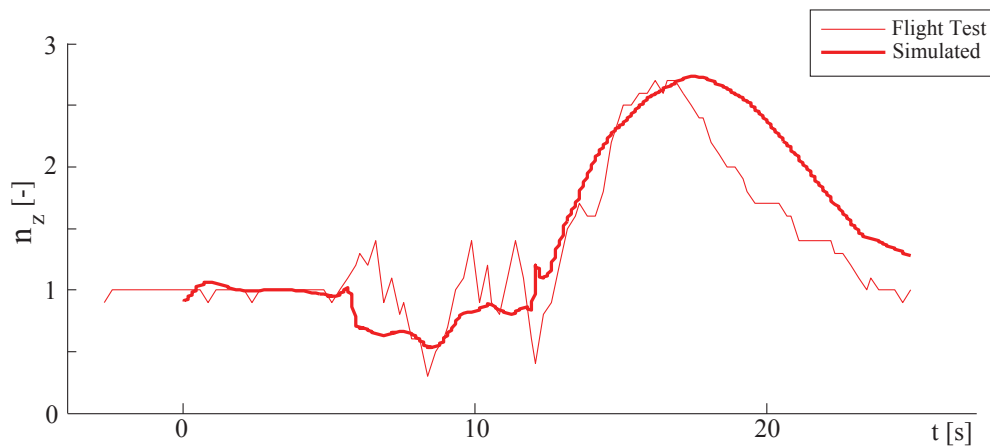


Figure 5.25: Load factor, comparison between flight test and simulation output, spin 3

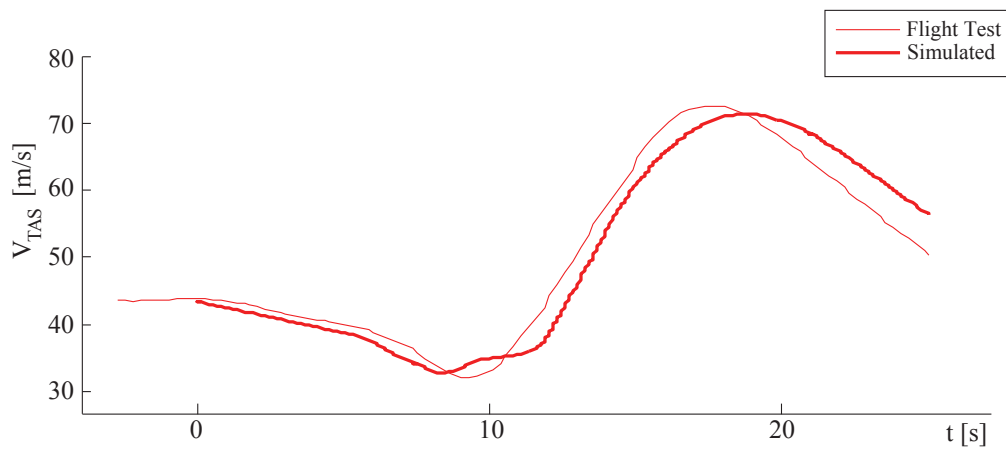


Figure 5.26: Flight speed, comparison between flight test and simulation output, spin 3

The results of the simulations were considered a good approximation of the behavior of the aircraft during the spin maneuver from the stall and spin entry to the recovery phase, thus validating the analytical model and the estimated values of the aerodynamic coefficients.

5.4 Spin susceptibility criteria

Once determined the aerodynamic coefficients at high angles of attack it was possible to evaluate the susceptibility of the aircraft to depart from controlled flight and possibly enter a spin. These criteria are based mainly on the values of yawing-moment and rolling-moment coefficients due to sideslip angle at high angle of attack. Even though the criteria presented are only approximate, they can be applied to give an estimation of the tendency of the aircraft to depart from controlled flight after a stall occurred [21].

- $C_{n\beta_{dyn}}$, Directional stability parameter

This parameter is used for the evaluation of the resistance to directional divergence. Its expression is shown below, and the requirement is for it to be positive:

$$C_{n\beta_{dyn}} = C_{n\beta} \cos \alpha - \frac{I_z}{I_x} C_{l\beta} \sin \alpha > 0$$

The plot of the parameter as a function of the angle of attack is shown in Figure 5.27 up to $\alpha = 50^\circ$. It can be seen that the parameter remains positive throughout the entire range considered, thus meeting the requirement even where $C_{n\beta}$ becomes negative.

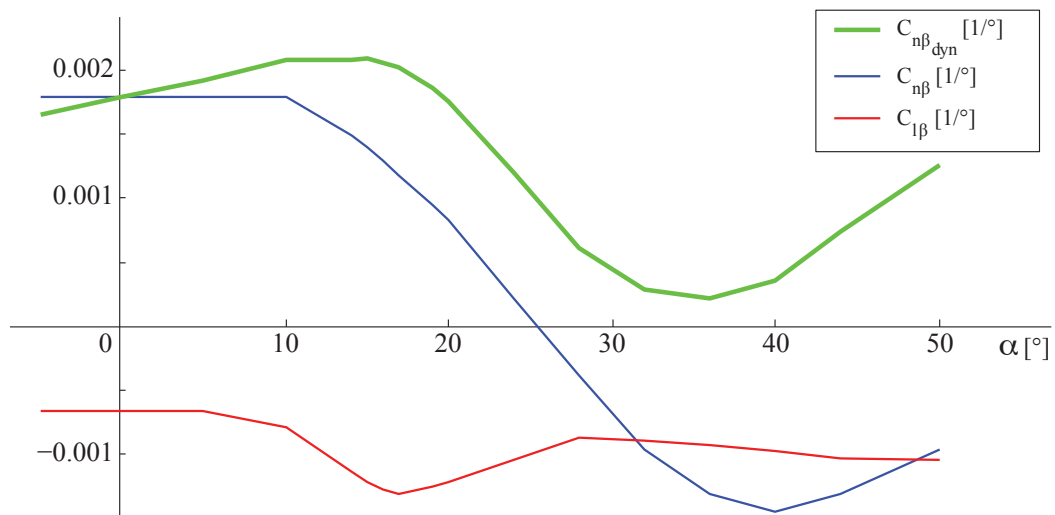


Figure 5.27: Directional stability parameter

- LCDP, Lateral control departure parameter

This parameter gives an indication of the lateral stability of the aircraft up to angles of attack beyond the stall. Its expression is shown below and again the requirement for stability is a positive value:

$$\text{LCDP} = C_{n\beta} - C_{l\beta} \frac{C_{n\delta_a}}{C_{l\delta_a}} > 0$$

The values for this parameter are shown in Figure 5.28 as function of the angle of attack. Negative values mean controls reversal, in which case the aircraft rolls in the opposite direction to the control input applied. It can be seen from the plot that this condition is reached at angles of attack above 25°.

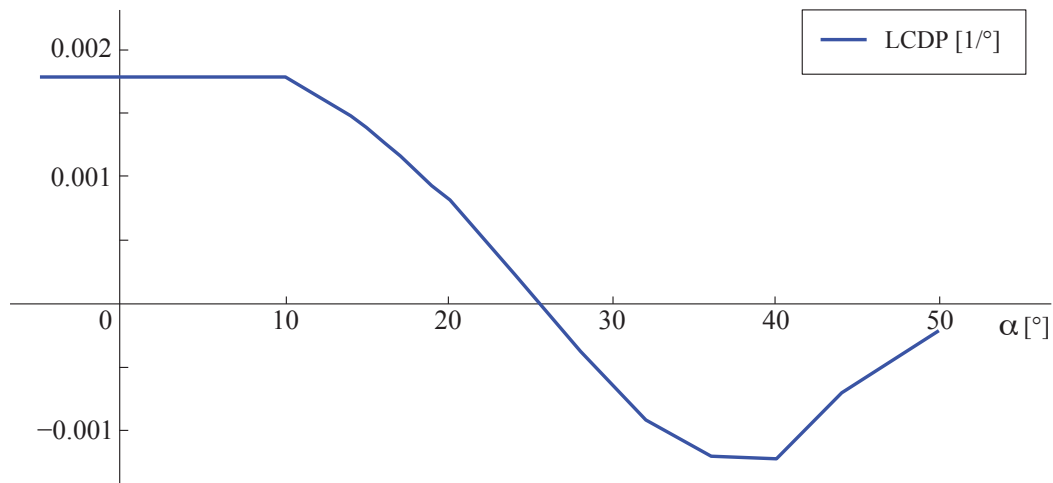


Figure 5.28: Lateral control departure parameter

- Bihrlé - Weissman chart

This chart combines the two parameters seen above by plotting them one against the other. Depending on the region of the chart in which the curve lies it is possible to determine the overall tendency of the aircraft to departure and spin entry.

The chart is shown in Figure 5.29 and the plot of the two parameters is shown in red for the range of angles of attack considered. The curve is all comprised in the region denominated by the letter F, starting closer to region A for lower angles of attack. From the description reported below the chart it is possible to understand that the aircraft will have little tendency to departure from controlled flight and will not enter a spin very easily without intentional action from the pilot.

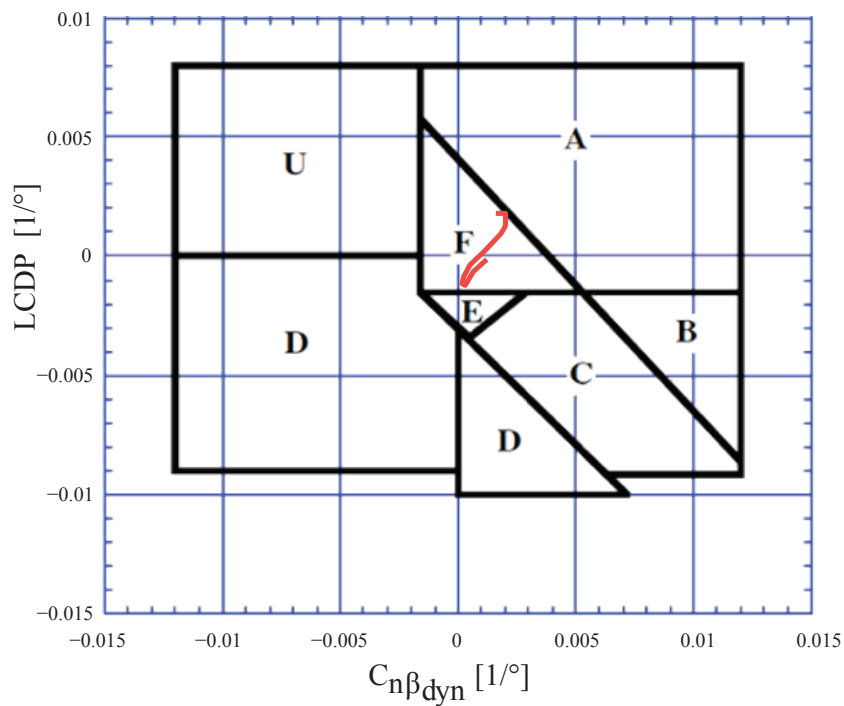


Figure 5.29: Bihrlé - Weissman chart

Where the characteristics of each region are:

- A: Highly departure and spin resistant
- B: Spin resistant, objectionable roll reversals can induce departure and post stall gyrations
- C: Weak spin tendency, strong roll reversal results in control-induced departure
- D: Strong departure, roll reversals and spin tendencies
- E: Weak spin tendency, moderate departure and roll reversals, affected by secondary factors
- F: Weak departure and spin resistance, no roll reversals, heavily influenced by secondary factors
- U: High directional instability, little data

6 Simulations

Once the analytical spin model was completed with the full aerodynamic data-set up to high angle of attack it was possible to employ the simulation program developed in order to be able to predict the behavior of the aircraft in a spin with greater number of turns. As seen in the previous chapter, the spin maneuvers that were tested in flight are limited to a single turn before the recovery procedure is applied, in order to demonstrate compliance with CS-VLA certification requirements [25].

However the company that produces the aircraft expressed the need to certify the same aircraft with increased maximum take-off weight for the Aerobatic category of EASA CS-23 [24]. To be able to comply with the requirements of the new certification with regard to the spin maneuver, the aircraft has to safely and promptly recover from a spin consisting of up to six turns.

The main purpose for the development of the simulation program was specifically to be capable of predicting the maneuver up to the fully developed spin phase based on the experimental data already gathered, prior to flight-testing.

In this chapter will be presented the comparison of the simulated maneuver with the experimental data from the spin tests performed on a scaled model and the prediction of a complete six-turns spin from stall to recovery.

6.1 Comparison with the dynamically scaled model

During the course of 2016 it was realized a dynamically scaled flying model of the same aircraft analyzed in the present work. The model was realized in order to perform a series tests to characterize the behavior of the aircraft during the spin maneuver.

To further verify the accuracy of the analytical model it was considered of interest to compare the results of the tests on the flying model with the output of the simulations. In order to make the comparison, the time histories of the flight tests had to be properly scaled using the criteria of dynamic similarity as a function of the scale factor. This way the magnitudes of the considered quantities are appropriately scaled back to the magnitudes for the full size aircraft.

The test point considered for the comparison is one for the standard spin maneuver, with clean configuration and ailerons neutral. Since the controls deflection of the model was not recorded, for the simulation inputs were used the standard controls of full elevator deflection followed by full rudder deflection for the spin entry, and simultaneous rudder and elevator neutralization for the recovery.

The results of the simulation and the comparison with the recorded time histories of the flying model are shown in the following figures.

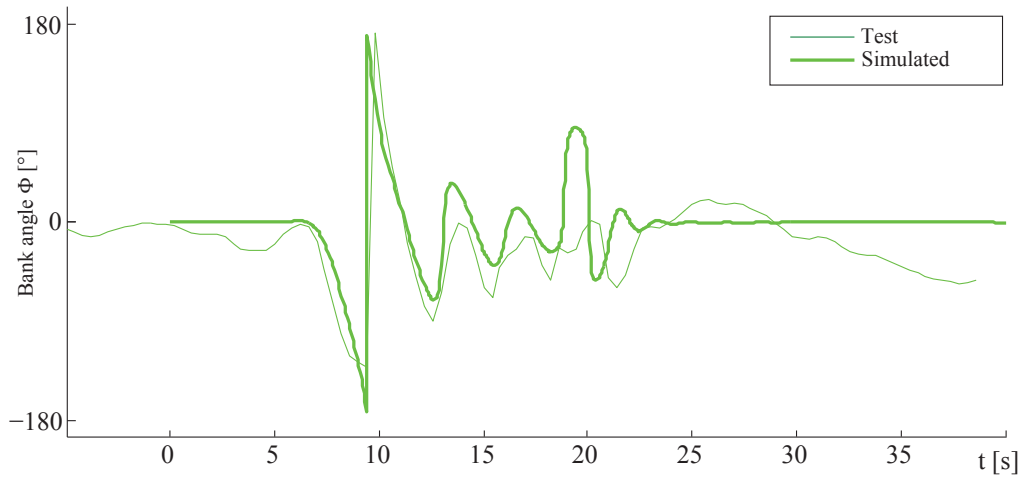


Figure 6.1: Bank angle, comparison between scaled model and simulation

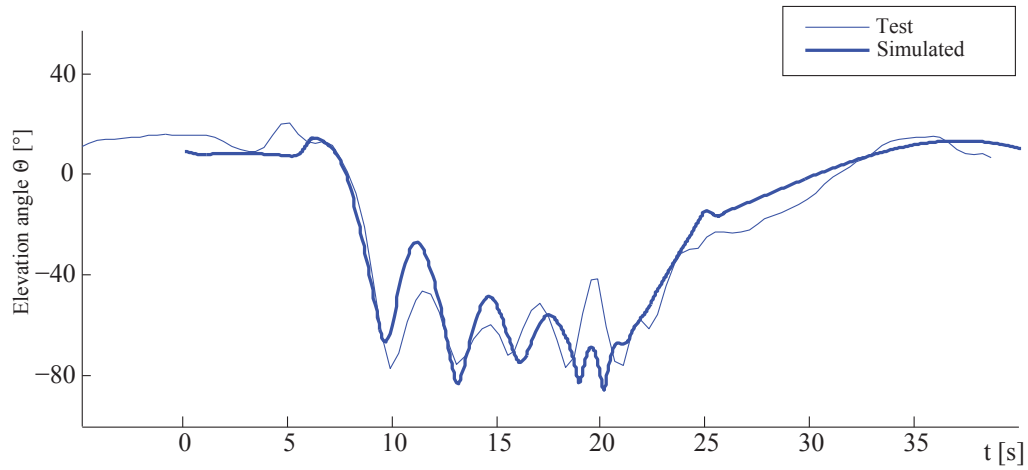


Figure 6.2: Elevation angle, comparison between scaled model and simulation

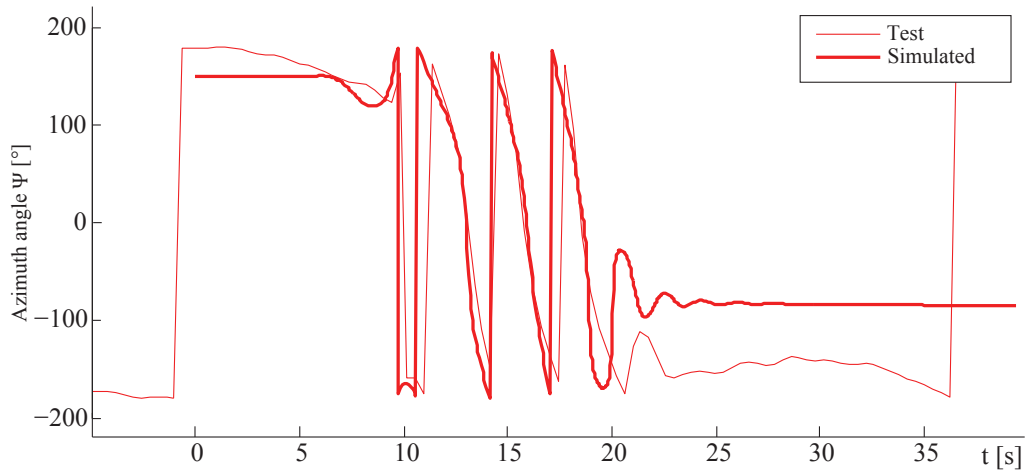


Figure 6.3: Azimuth angle, comparison between scaled model and simulation

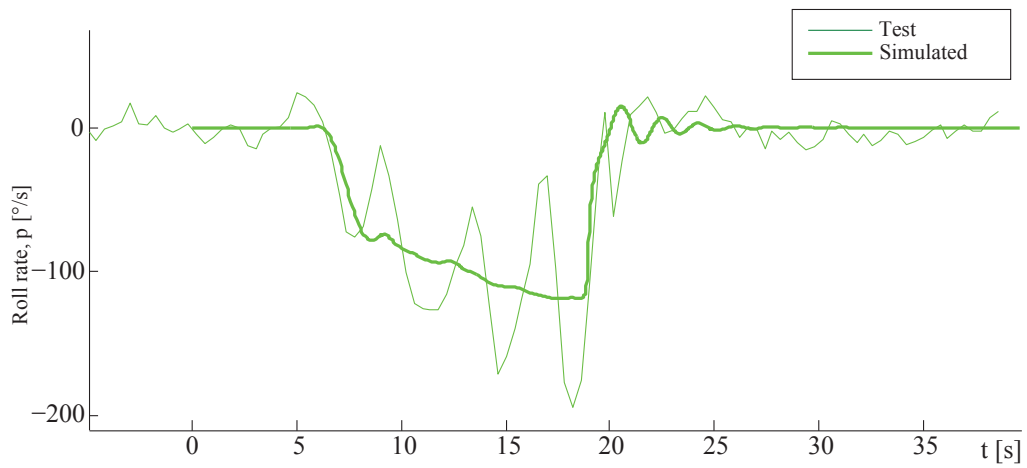


Figure 6.4: Roll rate, comparison between scaled model and simulation

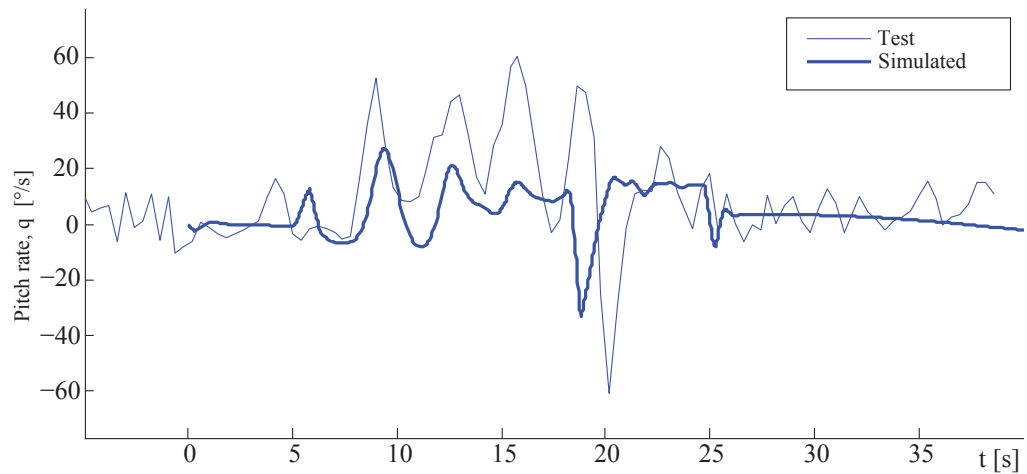


Figure 6.5: Pitch rate, comparison between scaled model and simulation

Simulations

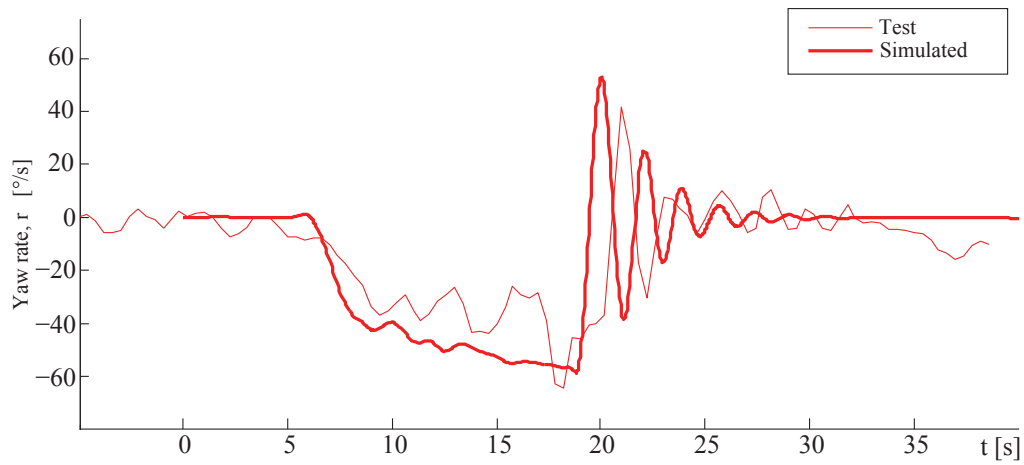


Figure 6.6: Yaw rate, comparison between scaled model and simulation

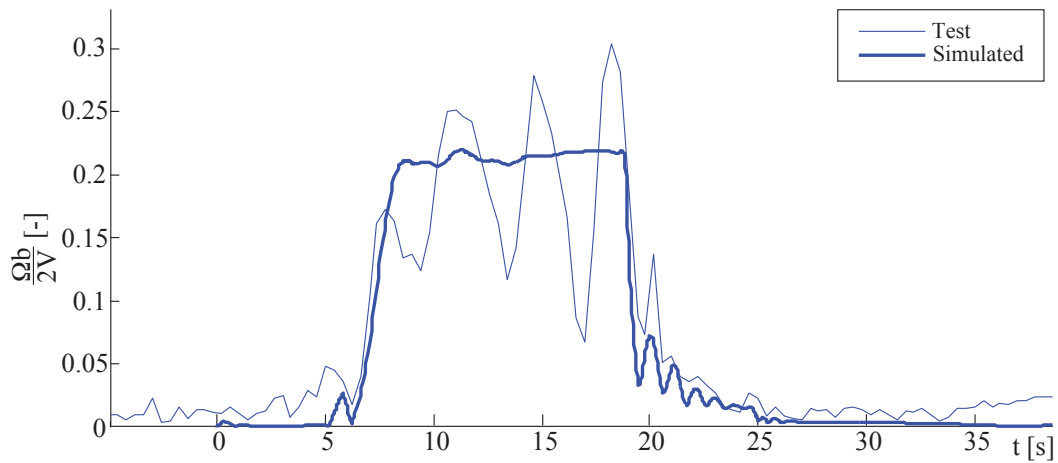


Figure 6.7: Non-dimensional spin rate of rotation, comparison between scaled model and simulation

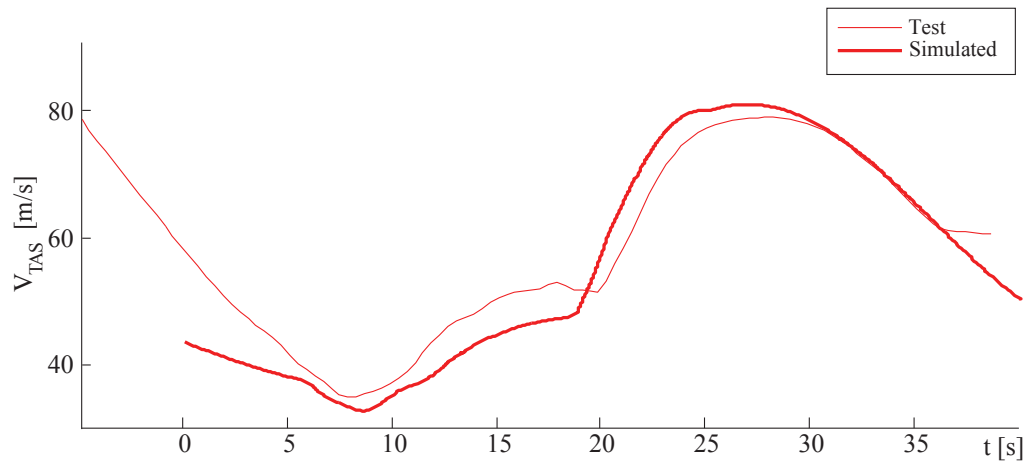


Figure 6.8: Flight speed, comparison between scaled model and simulation

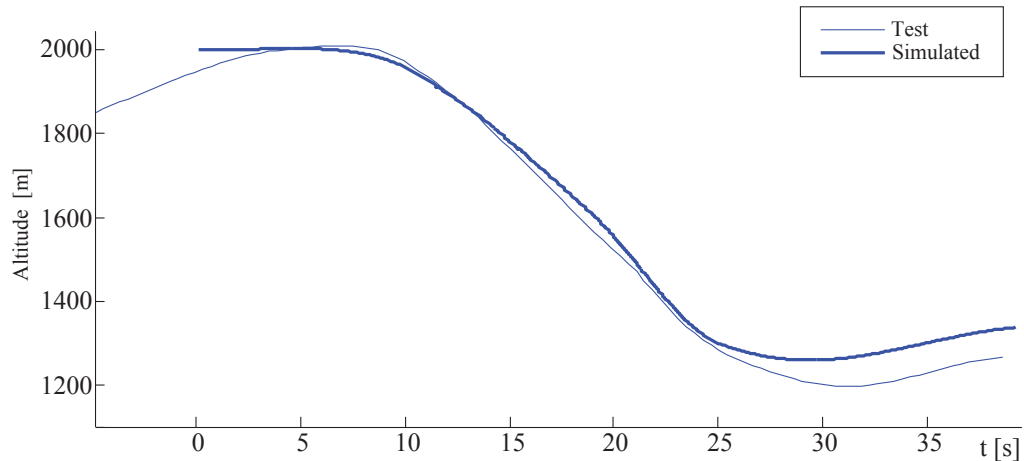


Figure 6.9: Altitude loss, comparison between scaled model and simulation

It can be seen from the graphs of the aircraft attitudes how the simulated behavior matches very closely the spinning attitudes of the scaled flying model, both in terms of the frequency of rotation and amplitude of the oscillations.

Looking at the angular rates it is apparent how the behavior of the model is very oscillatory, where the simulated one is a lot more stable. The oscillatory nature of the spin is probably caused by non-linearities in the yawing-moment and rolling-moment coefficients as a function of the spin rate of rotation. These non-linearities were not implemented in the analytical model mainly for two reasons: they are very difficult to predict without rotary balance tests in the wind tunnel and because the spin tests on the full scale aircraft did not exhibit such oscillatory behavior. However the simulated angular rates are very comparable with the mean values of the oscillations shown by the scaled model.

The flight velocity and the altitude loss simulated are both a good representation of the behavior shown by the model.

In Figure 6.10 is shown a qualitative comparison of the entire maneuver between the simulation output and the scaled model extracted from video files.

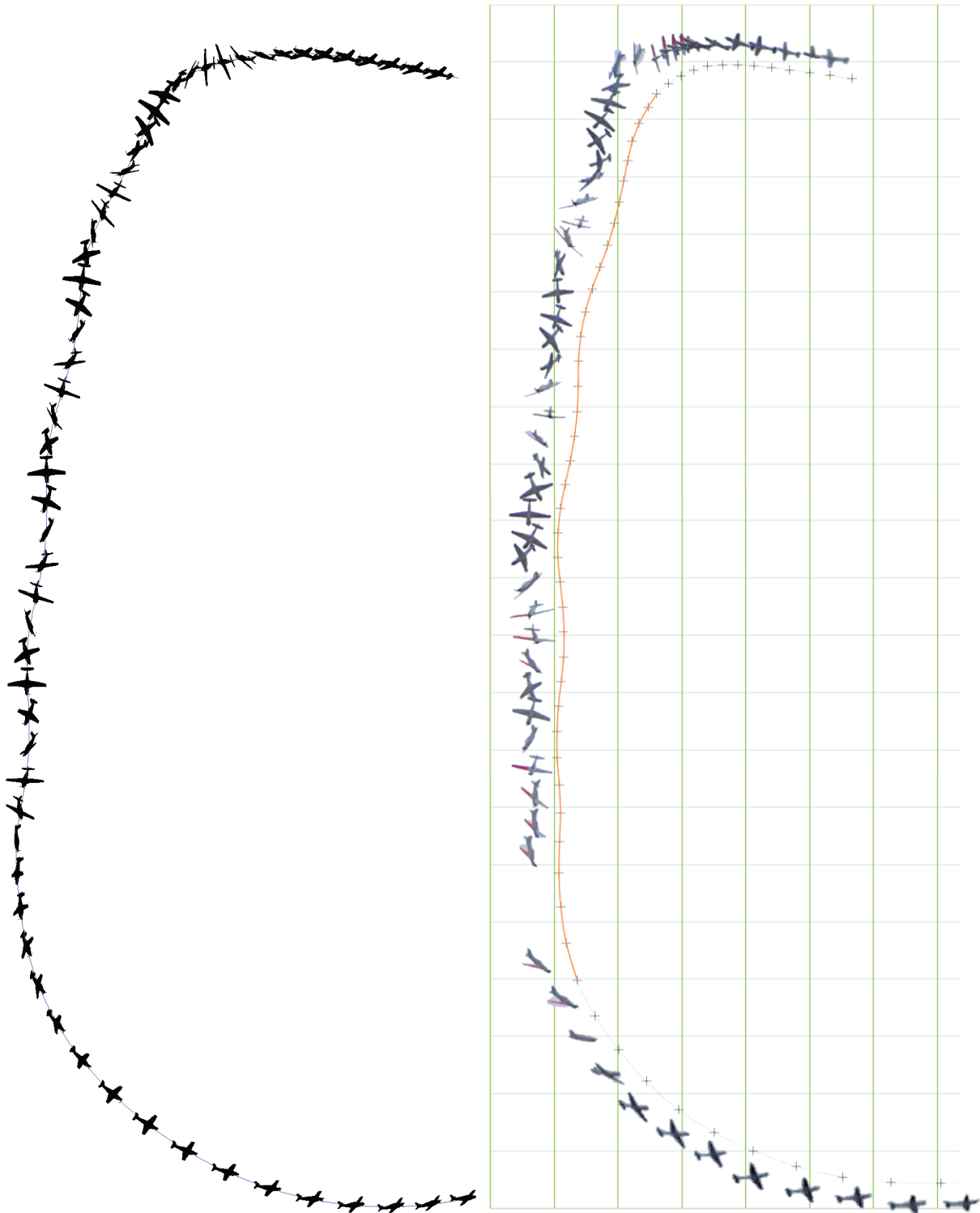


Figure 6.10: The spin maneuver, graphic comparison between the simulation (left) and the scaled model (right, extracted from video files)

6.2 Spin maneuver prediction

The main purpose for the development of the analytical model presented in this chapter is the ability to predict the behavior of the aircraft under study in a fully developed spin.

In order to certify the aircraft CS-23 in the aerobatic category, a spinning requirement must be met: the aircraft must recover from any point in a spin up to six turns in not more than one and one-half additional turns after the first control action for recovery is applied. Additionally the limit load factor and the limit air speed must never be exceeded.

After the finalization of the analytical model, the attention was directed towards the simulation of a complete six-turns spin maneuver, in order to assess that the spin and recovery characteristics of the aircraft would meet the certification requirements.

The procedure followed was to simulate the maneuver without the controls for recovery, in order to determine the time in which the sixth turn would be completed. This resulted in about 20 seconds from the stall and initiation of the spin to the completion of the sixth turn. It was then possible to define the correct time history of the control inputs by applying the standard recovery actions right after the completion of the sixth turn as shown in Figure 6.11.

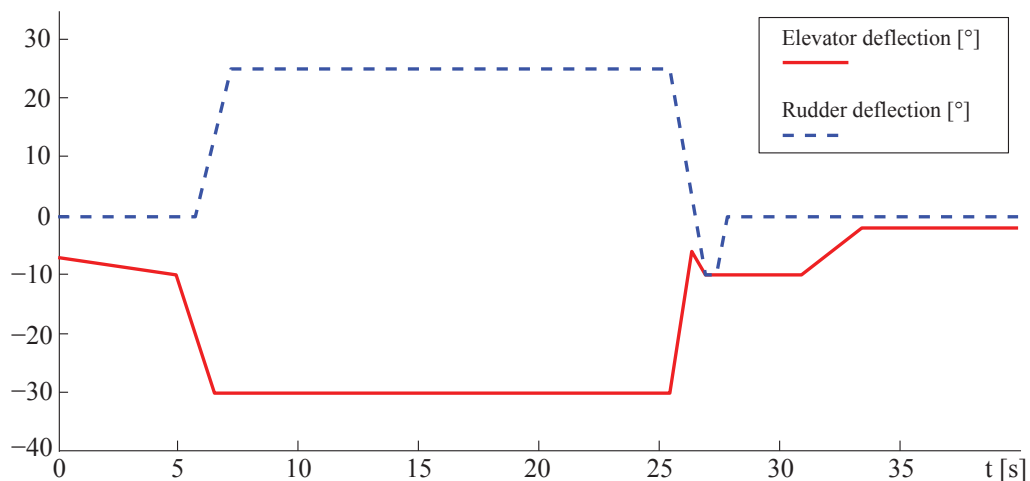


Figure 6.11: Controls deflection, inputs for the simulation

The resulting time histories of the aircraft attitudes and angular rates as output of the simulated maneuver are shown in the following figures.

The plots of the aircraft attitudes are pretty much textbook, showing oscillations in pitch and roll that rapidly decrease in amplitude and tend to a stabilized value.

Looking at the plot of the azimuth angle (Figure 6.14) it is possible to see the sweeping pattern from 180° to -180° typical of the spin, which indicates that a stable yaw-rate is quickly achieved. It can also be noted that after the recovery controls are applied, at $t \cong 25$ s, the rotation is rapidly arrested after a few oscillations. In total it takes about one-half additional turn to completely stop the rotation and to achieve full recovery, thus meeting one of the certification requirements.

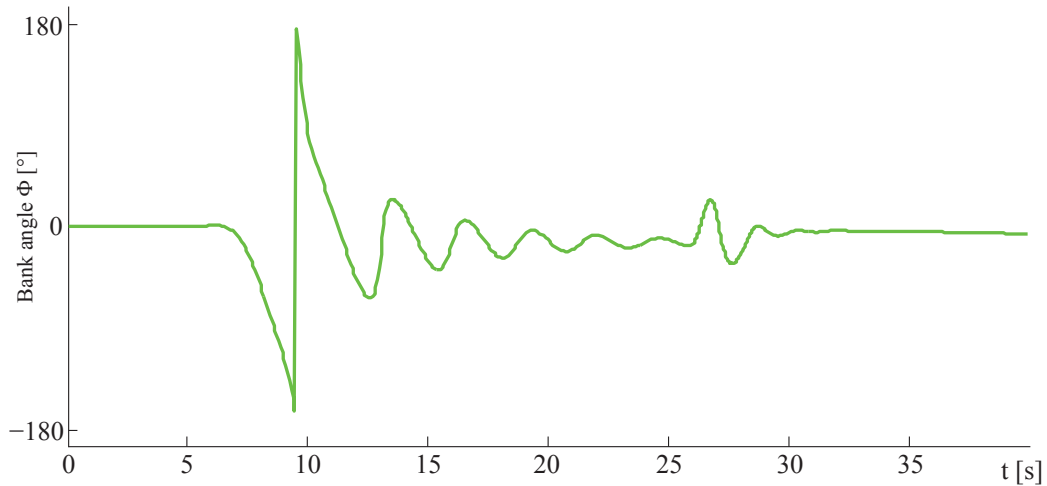


Figure 6.12: Bank angle, simulated prediction

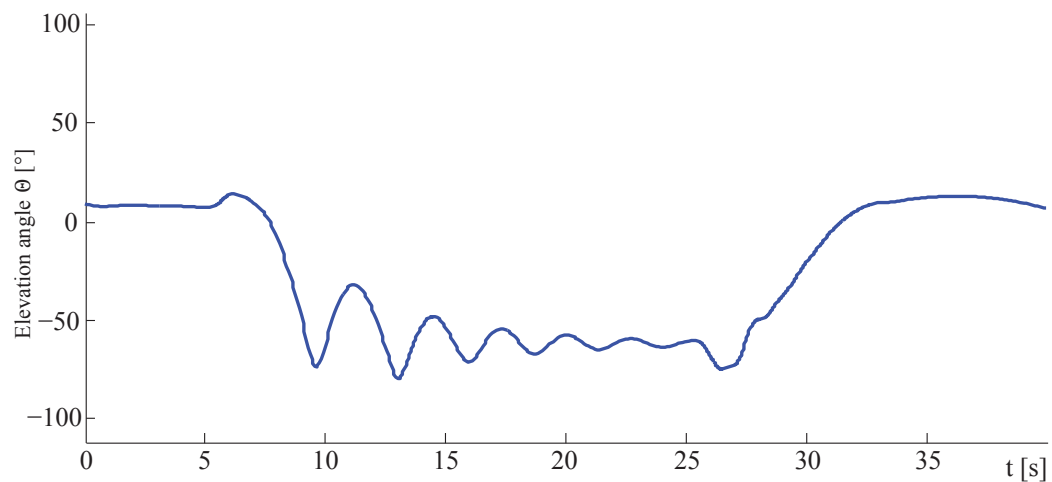


Figure 6.13: Elevation angle, simulated prediction

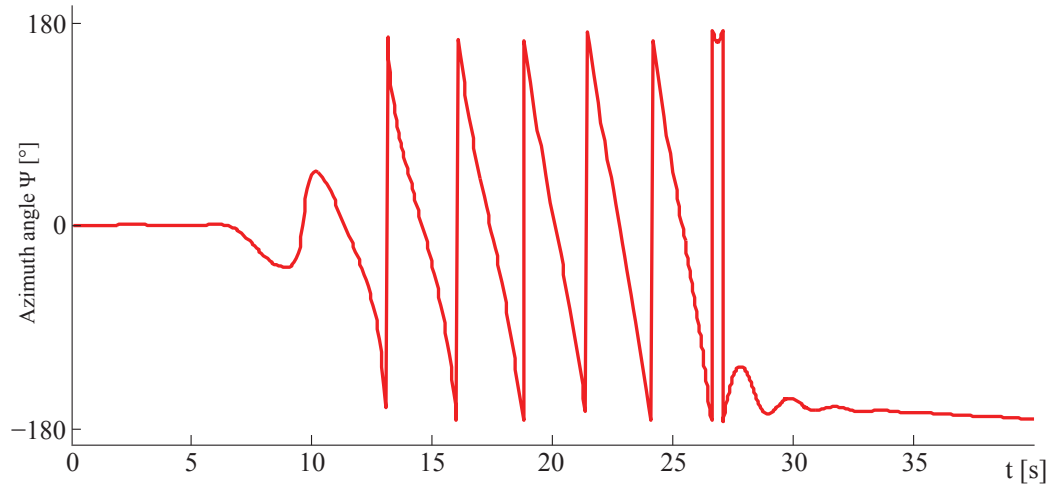


Figure 6.14: Azimuth angle, simulated prediction

The angular rates show very little oscillations in roll and yaw and few oscillations in pitch that however are quickly dampened. Stable rates are achieved after the third turn indicating that equilibrium between aerodynamic and inertial forces and moments is reached and the spin is fully developed.

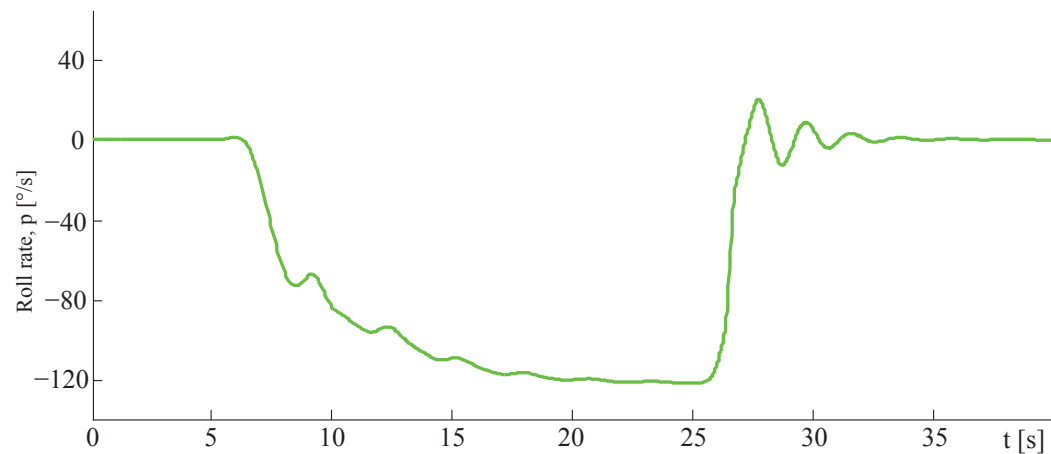


Figure 6.15: Roll rate, simulated prediction

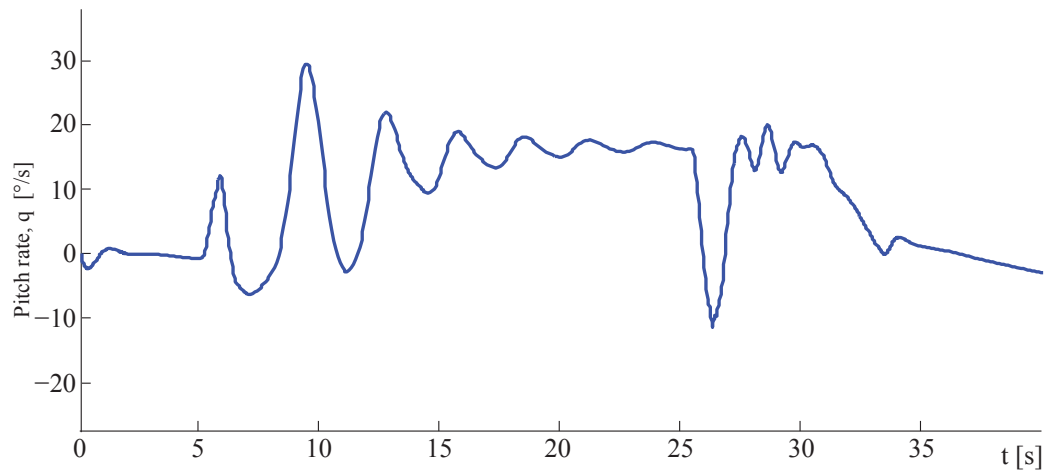


Figure 6.16: Pitch rate, simulated prediction

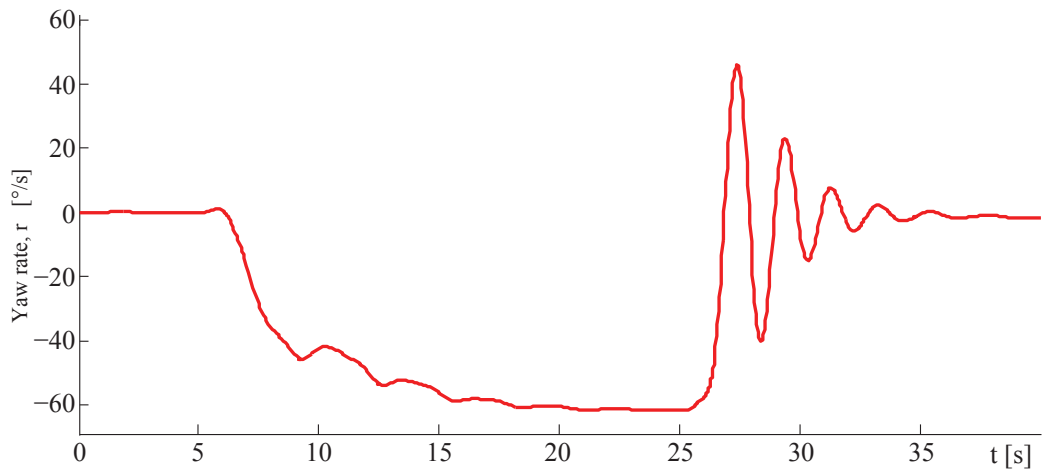


Figure 6.17: Yaw rate, simulated prediction

The plot of the angle of attack (Figure 6.18) indicates clearly that the spin is rather steep with no tendency to flatten out. The angle of attack stabilizes around 28° after about three turns.

As discussed before a steep spin is preferable and less critical to recovery from, mainly because the rudder is able to maintain part of its control effectiveness needed for a prompt recovery. In a flatter spin in fact it is possible that the wake produced by the stalled tail-plane would shield the rudder and vertical tail enough to render the recovery very difficult if not impossible.

The angle of sideslip (Figure 6.19) present little oscillations in the incipient spin phase and reaches a stable value close to -1° after the third turn.

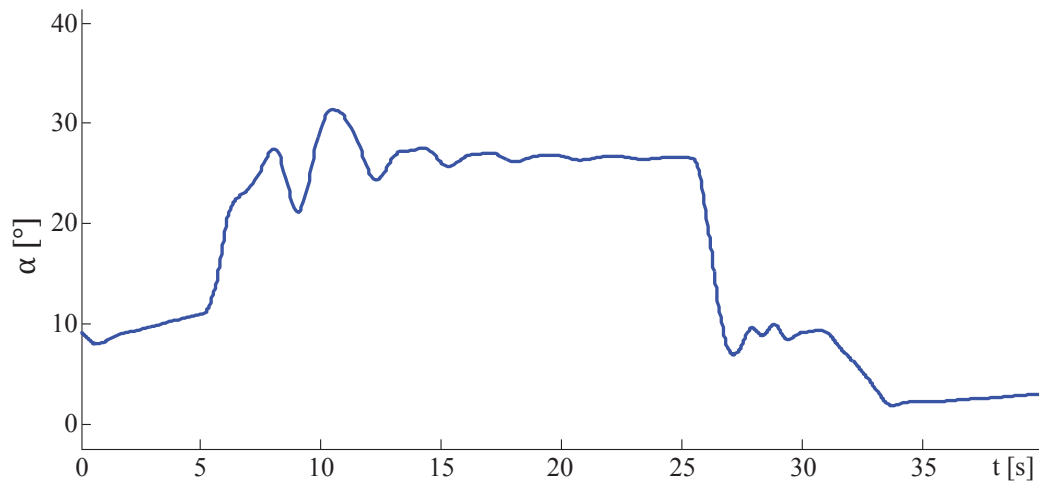


Figure 6.18: Angle of attack, simulated prediction

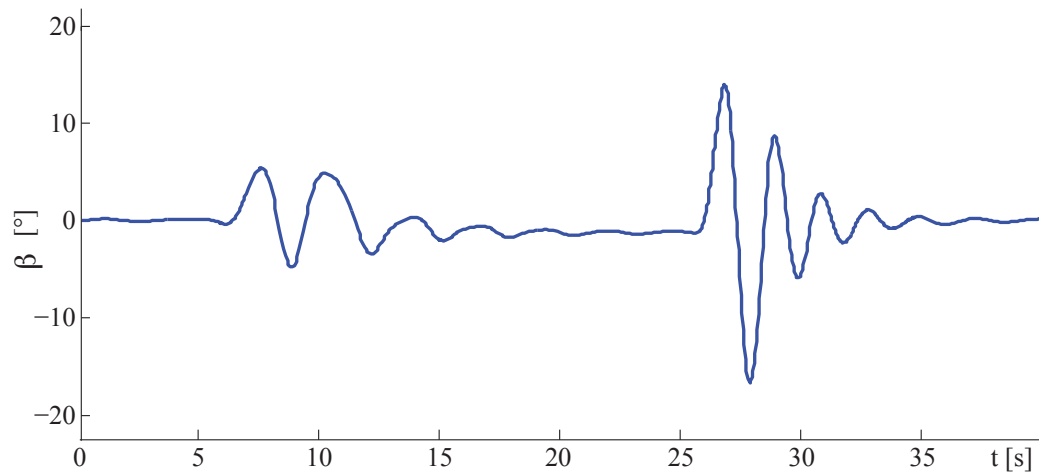


Figure 6.19: Angle of sideslip, simulated prediction

Looking at the plot of the equivalent air speed (Figure 6.20) it is apparent that, after the stall and spin entry phase, the velocity of descent reaches a stable value of about 44 m/s, which is not excessive and typical of a steep spin. In the pull-up maneuver, needed to regain level flight after the rotation is stopped, the flight speed reaches a maximum value of about 62 m/s, which is well below the limit air speed of 88 m/s.

The overall spin rate of rotation (Figure 6.21) reaches a stable maximum value of 137°/s, which again is typical for a steep spin and not excessive. At this rate it takes 2.6 s to complete a full rotation, which would be easily manageable for the pilot.

Simulations

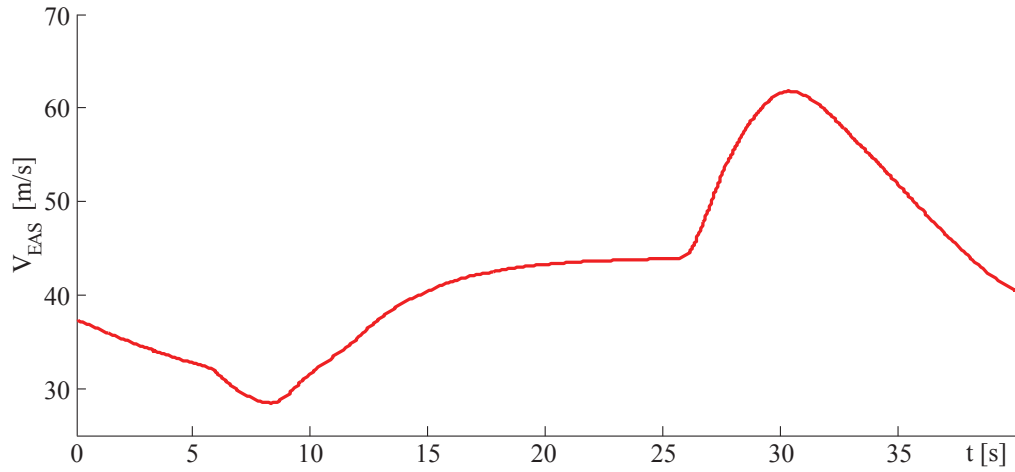


Figure 6.20: Equivalent air speed speed, simulated prediction

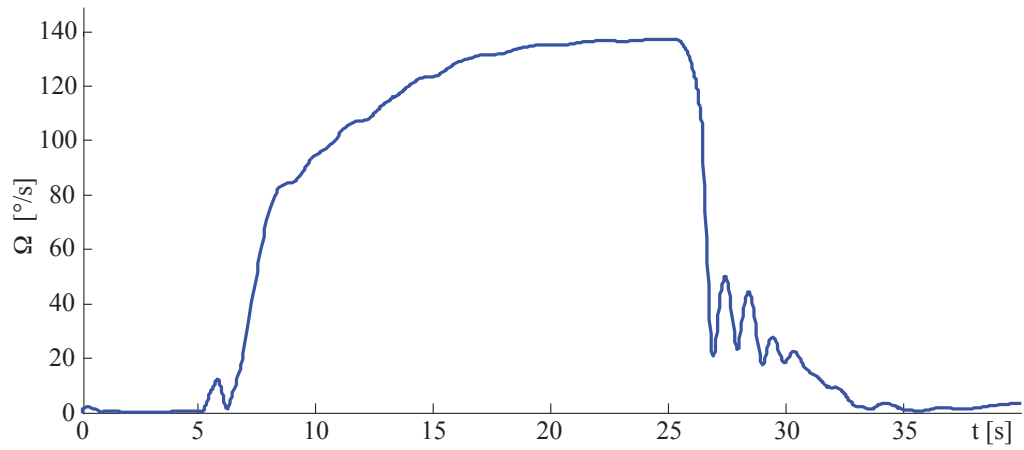


Figure 6.21: Spin rate of rotation, simulated prediction

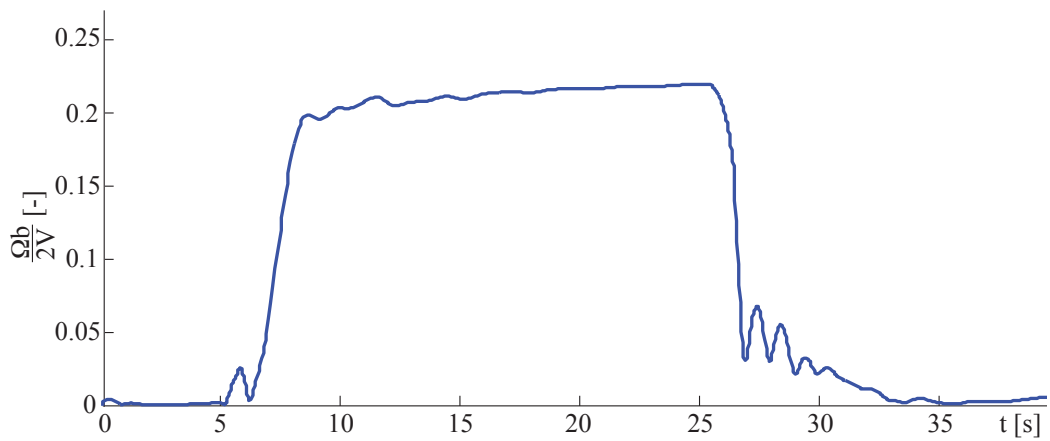


Figure 6.22: Non-dimensional spin rate of rotation, simulated prediction

The load factor (Figure 6.23) in the stable spin gets to a comfortable value of around 1.5 times the acceleration of gravity, and reaches the peak value of less than 3 during the pull-up maneuver. The limit positive load factor for the aircraft is +5, meaning that the requirement is met with ample margin.

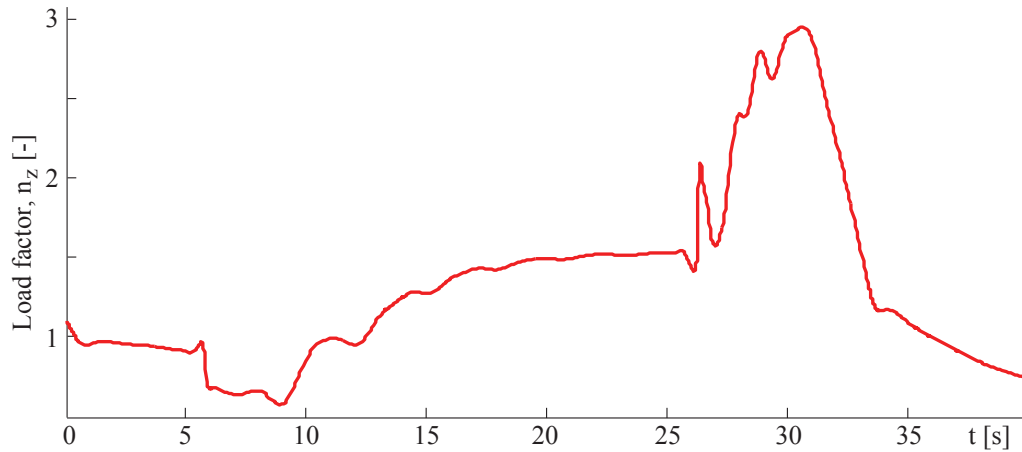


Figure 6.23: Load factor, simulated prediction

The predicted loss of altitude for the entire maneuver from the stall to the complete recovery, is 1025 m (~3360 ft), starting from a safe altitude of 3000 m (~10000 ft) (Figure 6.24).

For every turn in the spin the loss of altitude is about 125 m, meaning a total of 750 is needed to complete six turns. Additional 275 m are lost to complete the recovery procedure and regain level flight.

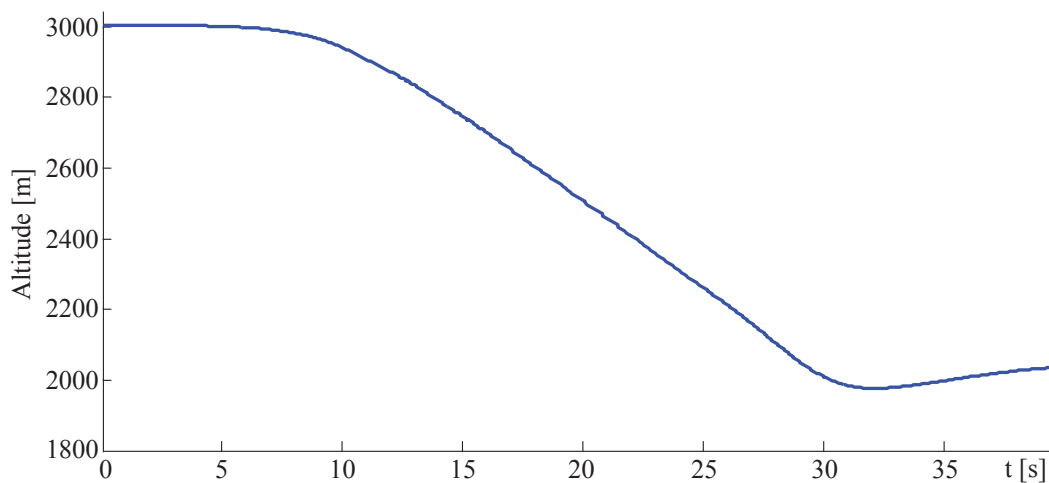


Figure 6.24: Altitude, simulated prediction

7 Parametric study

In this chapter will be presented the parametric study performed in order to assess the spin behavior in greater detail and the effect of different control inputs and other variables to the overall spin maneuver.

The study was carried out by employing the simulation algorithm described in the previous chapters in order to test different flight conditions from stall and spin entry to the recovery procedure.

The aircraft under test is the same that was modeled in the previous chapters and, unless stated otherwise, the mass and load distribution has to be considered the same as expressed in Table 5.14.

For all the test points considered, where is not specified, the simulated altitude at the beginning of the maneuver is 3000 m (~10000 ft.).

First will be presented the simulations of the different stall maneuvers in accordance to the requirements for the certification CS-23. The aim is to determine whether the aircraft shows a tendency to stall asymmetrically, with possible departure from controlled flight, which eventually could lead to an inadvertent spin.

After the stall behavior assessment, it was tested the spin performance for the basic configuration with increasing number of turns. In this case the aim is to denote the difference in the spinning characteristics from the incipient phase, which is mostly oscillatory, to the fully developed phase, in which equilibrium is reached and all the variables show a stabilized constant value.

The study of the recovery performance was conducted with the simulations of the three most common recovery procedures. Starting from the fully developed spin phase, after the completion of the sixth turn, the three different sets of control inputs for recovery were applied in order to determine the number of additional turns needed to stop the rotation and the loss of altitude before regaining level flight.

The last part of the chapter presents the simulations that were carried out in order to determine the effect of other variables to the overall performance. Specifically it was tested the effect of the increase of weight, increase of yawing moment of inertia and the decrease of altitude at the beginning of the maneuver.

For all the test point that were simulated are reported the quantities that were considered of greatest relevance as well as the graphs of the time histories of the input and outputs of the simulations.

7.1 Stalls

The simulations that are presented in this paragraph were performed in order to determine the behavior of the aircraft during and after a stall. The importance of these tests is to assess whether in such conditions the aircraft would develop lateral and/or directional instability, which could possibly lead to an inadvertent spin.

In order to study the aircraft behavior in detail it was first simulated the stall from level flight as well as two test points from turning flight, which aggravates the stall by introducing asymmetries in the flight conditions.

All the maneuvers that were simulated are in accordance with the acceptable means of compliance for CS-23 certification [24].

Since the simulation program was developed mainly to assess the spin behavior, at the present state it does not allow for different power settings to be simulated, and for this reason all the maneuvers that will be shown in the following paragraphs were performed in power off conditions.

7.1.1 Wings level stall

For testing the stall characteristics from level flight, the certification requires the maneuver to be initiated at a flight speed at least 10 knots above the stall speed. Then the speed must be reduced at a rate below 1 knot per second by gradually pulling on the elevator control until the stall occurs, usually denoted by a downward pitching motion. After the stall occurs, normal use of the elevator control is allowed for recovery.

To be able to simulate the stall behavior correctly, the maneuver was initiated at about 73 knots EAS, and a time history of the elevator controls was provided in order to achieve the desired rate of speed reduction. After stall, the elevator was brought back to 0° followed by a pull-up maneuver.

The simulations produced a stall characterized by a downward pitching motion and no sign of lateral or directional instability with rudder and ailerons controls held in neutral position. The flight speed quickly rises above the stall speed allowing for a prompt recovery.

The recorded stall speed and angle of attack are shown below:

$$V_s = 60 \text{ knots} \cong 31 \text{ m/s}$$

$$\alpha_s = 16.5^\circ$$

The time histories for the elevator input and the simulated outputs are shown in Figure 7.1.

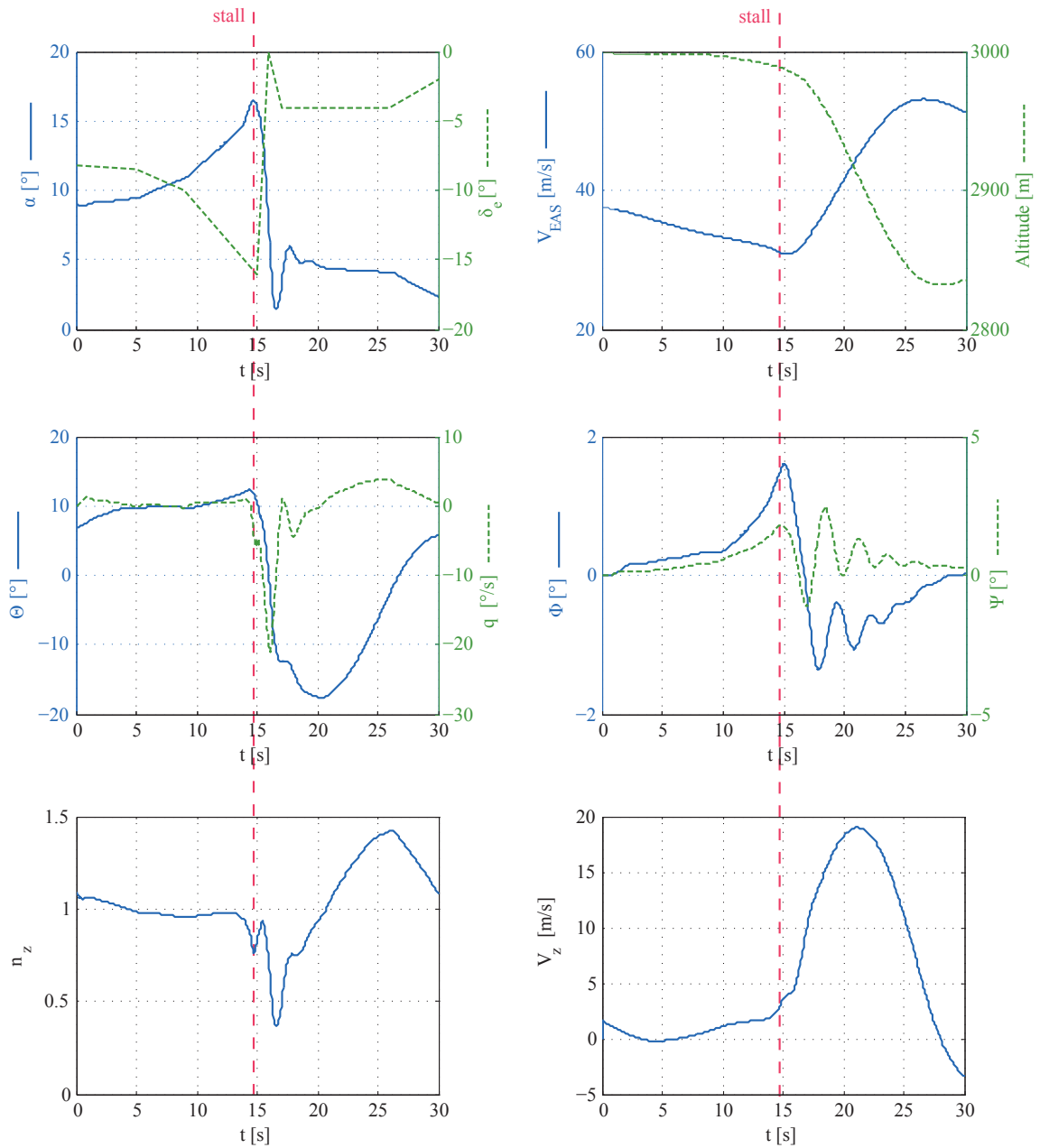


Figure 7.1: Time histories for simulated wing level stall

7.1.2 Turning flight stall

The required procedure to assess the turning flight stall prescribes the aircraft to be maintained in a coordinated turn at 30° of bank. The initial flight speed and rate of speed reduction are the same as seen for the wing level stall as well as the recovery procedure. In order to be compliant with the certification requirement, after the stall is reached the bank angle must not exceed 60°. Other limitations include the requirement to not exceed the maximum allowable speed and the limit load factor.

The control input for the elevator is similar to the one for the level flight stall, increasing progressively until stall is reached, released to 0° and followed by a pull-up maneuver. The 30° bank angle is imposed in the initial conditions and maintained with minimal aileron control. After stall all controls are neutralized prior to the pull-up.

The simulations show a similar behavior as seen for the wing level stall, characterized by downward pitching motion and regain of speed with no sign of lateral or directional instability. After stall the bank angle increases by only 4° before returning back towards level flight.

The recorded stall speed and angle of attack are shown below:

$$V_s = 62 \text{ knots} \cong 32 \text{ m/s}$$

$$\alpha_s = 16.3^\circ$$

The time histories the simulated turning flight stall are shown in Figure 7.2.

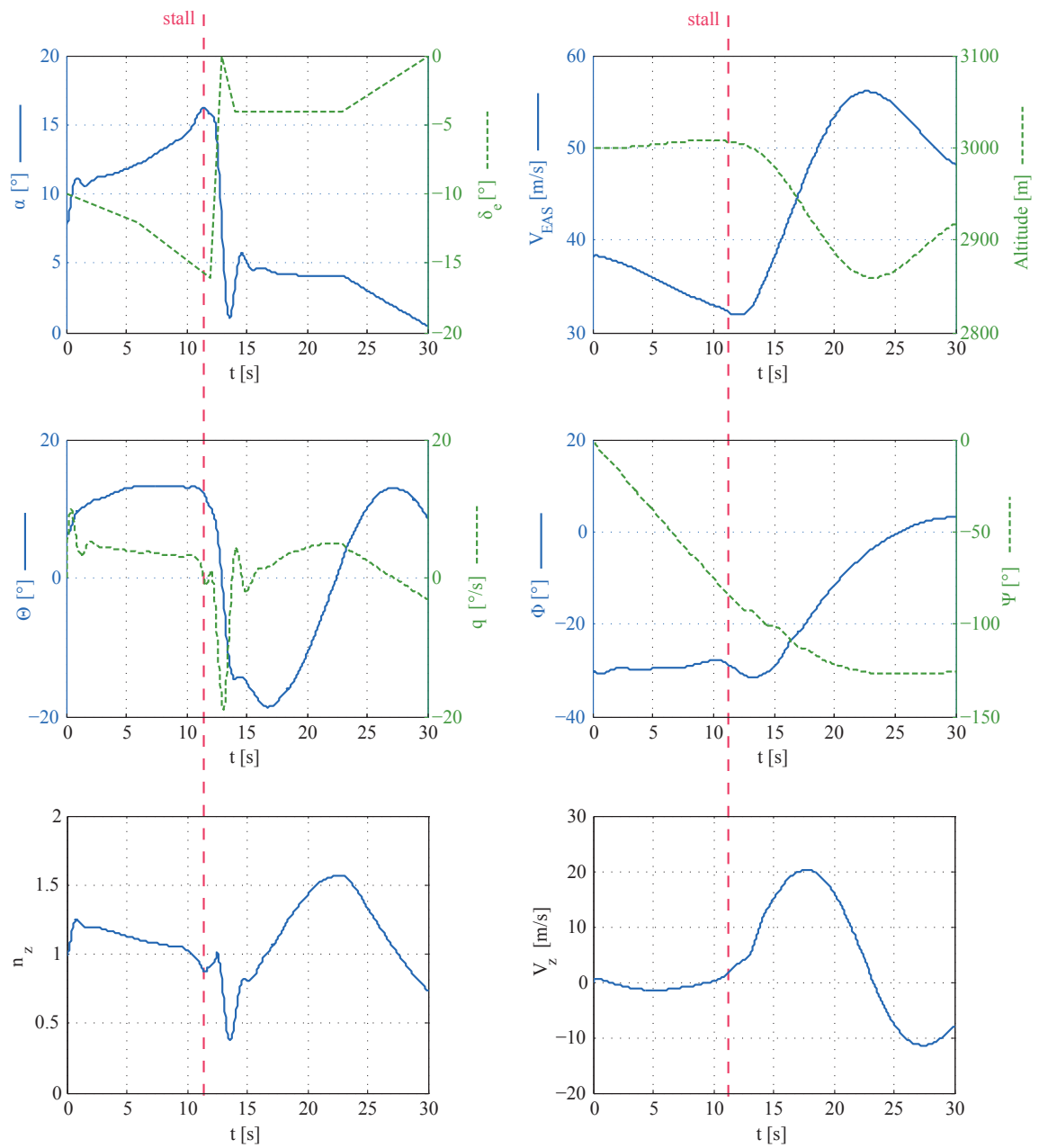


Figure 7.2: Time histories for simulated turning flight stall

7.1.3 Accelerated turning stall

In order to simulate the accelerated turning stall, it was again followed the procedure described by the certification requirements. The procedure is very similar to the one for the turning flight stall, with the main difference being the rate of speed reduction that has to be maintained between 3 and 5 knots per second by a more rapid increase of the elevator deflection. The initial flight conditions are the same as for the previous maneuver with a bank angle held at 30°. After stall is reached the maximum allowable bank angle this time is 90°. As before the maximum flight speed and limit load factor must not be exceeded in order to satisfy the requirement.

The control inputs to the simulation program are similar to the ones used for the turning flight stall, with the exception of the elevator deflection which is increased more rapidly in order to achieve the higher rate of speed reduction.

The resulting outputs of the simulation show again a very good stall behavior, with pitch-down motion and no sign of lateral or directional instability. There is no noticeable increase in bank angle at stall, which gets reduced toward level flight during the recovery.

The recorded stall speed and angle of attack resulted as follows:

$$V_s = 66 \text{ knots} \cong 34 \text{ m/s}$$

$$\alpha_s = 17.5^\circ$$

In Figure 7.3 are represented the time histories for the simulated accelerated turning stall.

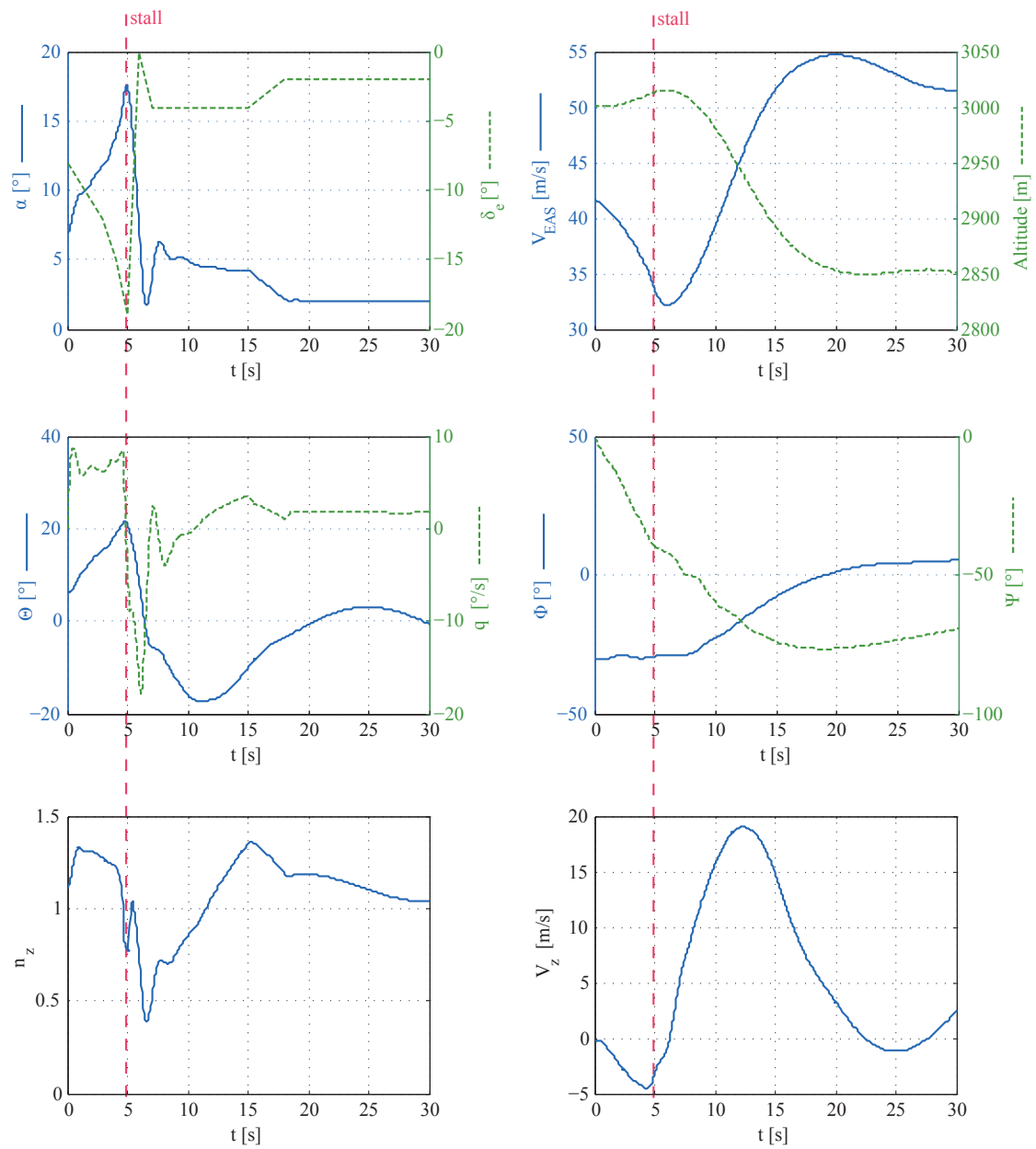


Figure 7.3: Simulated time histories of accelerated turning stall

7.2 Spins

After the stall behavior has been assessed in detail, which did not present any sign of departure from controlled flight, the next step in the study of the post-stall characteristics of the aircraft is the addition of directional control after stall. The addition of asymmetrical control, typically the deflection of the rudder, is most likely to cause the so-called post-stall gyrations, which if maintained would lead to an incipient spin.

In order to determine in greater detail the spinning characteristics from the incipient phase to the fully developed spin, it was decided to simulate the maneuver from stall to recovery with incremental number of turns.

The control inputs for spin entry are the same for all the test points. In particular they consist in a wing level stall followed by full elevator deflection and simultaneous full pro-spin rudder deflection, held until the desired number of turns is achieved.

The recovery procedure, again are the same for all the simulation in this paragraph, consisting in simultaneous neutralization of the elevator and deflection of the rudder 10° against the spin until the rotation is stopped, immediately followed by a pull-up maneuver in order to regain level flight.

For all the test points were recorded the most important parameter that characterize the spin in each of its phases.

7.2.1 Incipient spin

The incipient spin phase was studied by performing simulations for a one-turn spin immediately followed by the recovery procedure after the completion of one full turn. The most significant values such as time and loss of altitude per turn as well as the mean and oscillatory values for angle of attack, angle of sideslip, and angular rates were recorded and are presented in Table 7.1.

The plots of the time histories of the simulated inputs and outputs are shown in Figure 7.4.

The incipient spin is characterized by an oscillatory nature, as can be seen clearly from the plots of the angle of attack and angle of sideslip. The recovery from this phase is very quick, needing about one quarter additional turns to stop the rotation. Since the equilibrium is not reached, the first turn is rather slow and far from vertical, the loss of altitude is mainly due to the recovery maneuver.

Table 7.1: Significant values for the incipient spin simulation

V_s	31 m/s	Stall speed
t_{turn}	4.8 s	Average time for one turn
Δz_{turn}	100 m	Average loss of altitude per turn
Δz_{tot}	391 m	Total loss of altitude
$\Delta \Psi_{\text{rec}}$	100°	Additional rotation for recovery
α_{mean}	26°	Mean value of angle of attack
α_{osc}	$\pm 5^\circ$	Oscillatory value of angle of attack
β_{mean}	+1°	Mean value of angle of sideslip
β_{osc}	$\pm 5^\circ$	Oscillatory value of angle of sideslip
p_{mean}	-80°/s	Mean value of roll rate
p_{osc}	$\pm 15^\circ/\text{s}$	Oscillatory value of roll rate
q_{mean}	+13°/s	Mean value of pitch rate
q_{osc}	$\pm 17^\circ/\text{s}$	Oscillatory value of pitch rate
r_{mean}	-46°/s	Mean value of yaw rate
r_{osc}	$\pm 6^\circ/\text{s}$	Oscillatory value of yaw rate
$n_{z \text{ max}}$	2.63	Maximum load factor during recovery
$V_{\text{EAS max}}$	58 m/s	Maximum flight speed during recovery

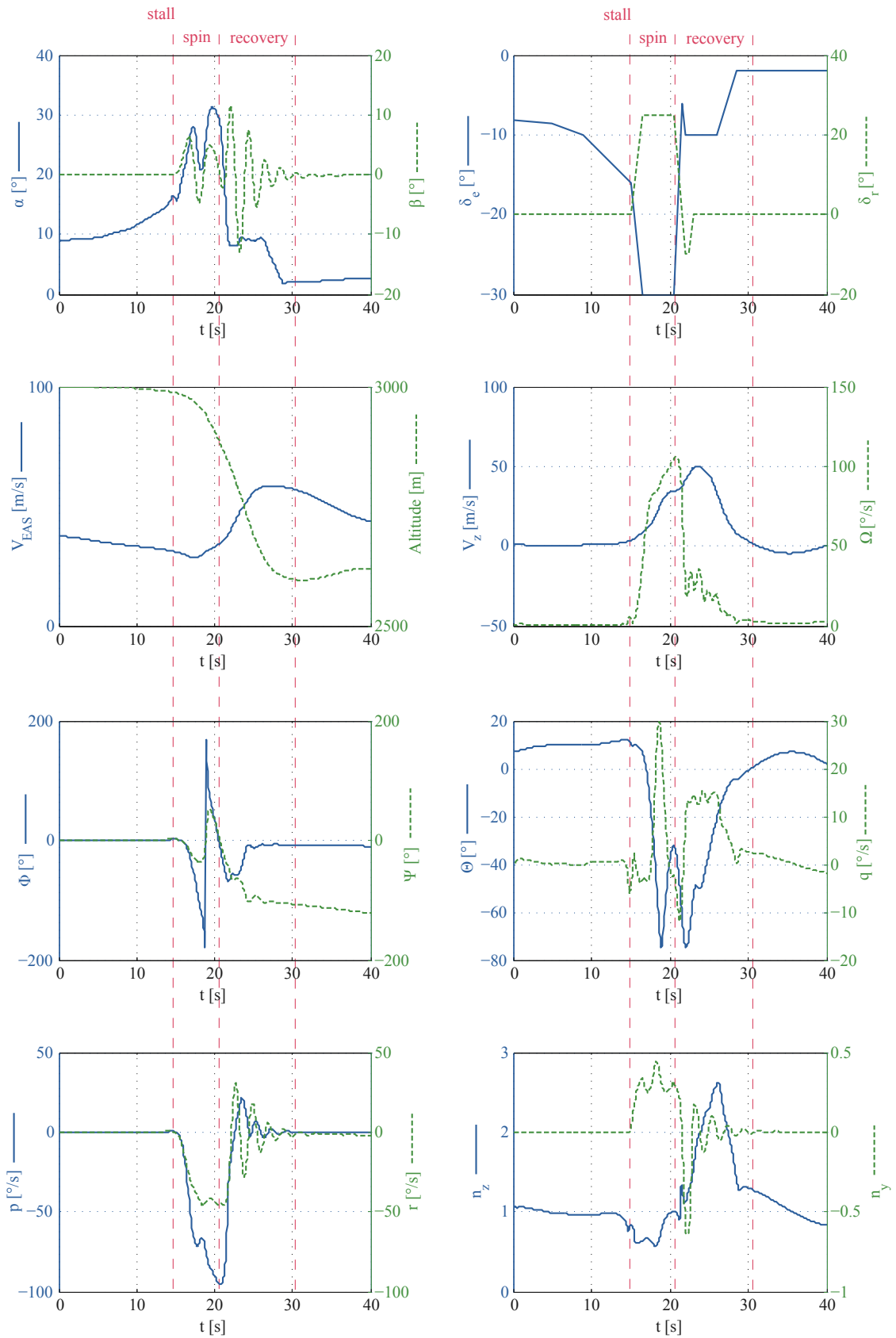


Figure 7.4: Time histories of the simulated incipient spin

7.2.2 Developed spin

In order to obtain the conditions for the developed spin, it usually takes three complete turns, after which all the variables reach their stabilized value with only minor oscillations. The results of the simulations for a three-turns spin are presented in Table 7.2 and Figure 7.5. It can be seen how at the end of the third turn all the variables have almost reached their stabilized value, and the oscillations are greatly reduced meaning that the conditions for equilibrium are achieved. With respect to the incipient spin, the average time needed to complete a turn is significantly reduced and the loss of altitude per turn is increased.

When the developed phase is reached, the recovery becomes more difficult due to the necessity to break the equilibrium of forces and moments. Even though the additional rotation needed to terminate the spin is greater, the recovery is still very prompt needing less than one half additional turns.

Table 7.2: Significant values for the developed spin simulation

V_s	31 m/s	Stall speed
t_{turn}	3.6 s	Average time for one turn
Δz_{turn}	121 m	Average loss of altitude per turn
Δz_{tot}	651 m	Total loss of altitude
$\Delta \Psi_{\text{rec}}$	168°	Additional rotation for recovery
α_{mean}	26.5°	Mean value of angle of attack
α_{osc}	$\pm 1^\circ$	Oscillatory value of angle of attack
β_{mean}	-1°	Mean value of angle of sideslip
β_{osc}	$\pm 0.5^\circ$	Oscillatory value of angle of sideslip
p_{mean}	$-96^\circ/\text{s}$	Mean value of roll rate
p_{osc}	$\pm 5^\circ/\text{s}$	Oscillatory value of roll rate
q_{mean}	$+16^\circ/\text{s}$	Mean value of pitch rate
q_{osc}	$\pm 3^\circ/\text{s}$	Oscillatory value of pitch rate
r_{mean}	$-52^\circ/\text{s}$	Mean value of yaw rate
r_{osc}	$\pm 3^\circ/\text{s}$	Oscillatory value of yaw rate
$n_z \text{ max}$	2.96	Maximum load factor during recovery
$V_{\text{EAS max}}$	62 m/s	Maximum flight speed during recovery

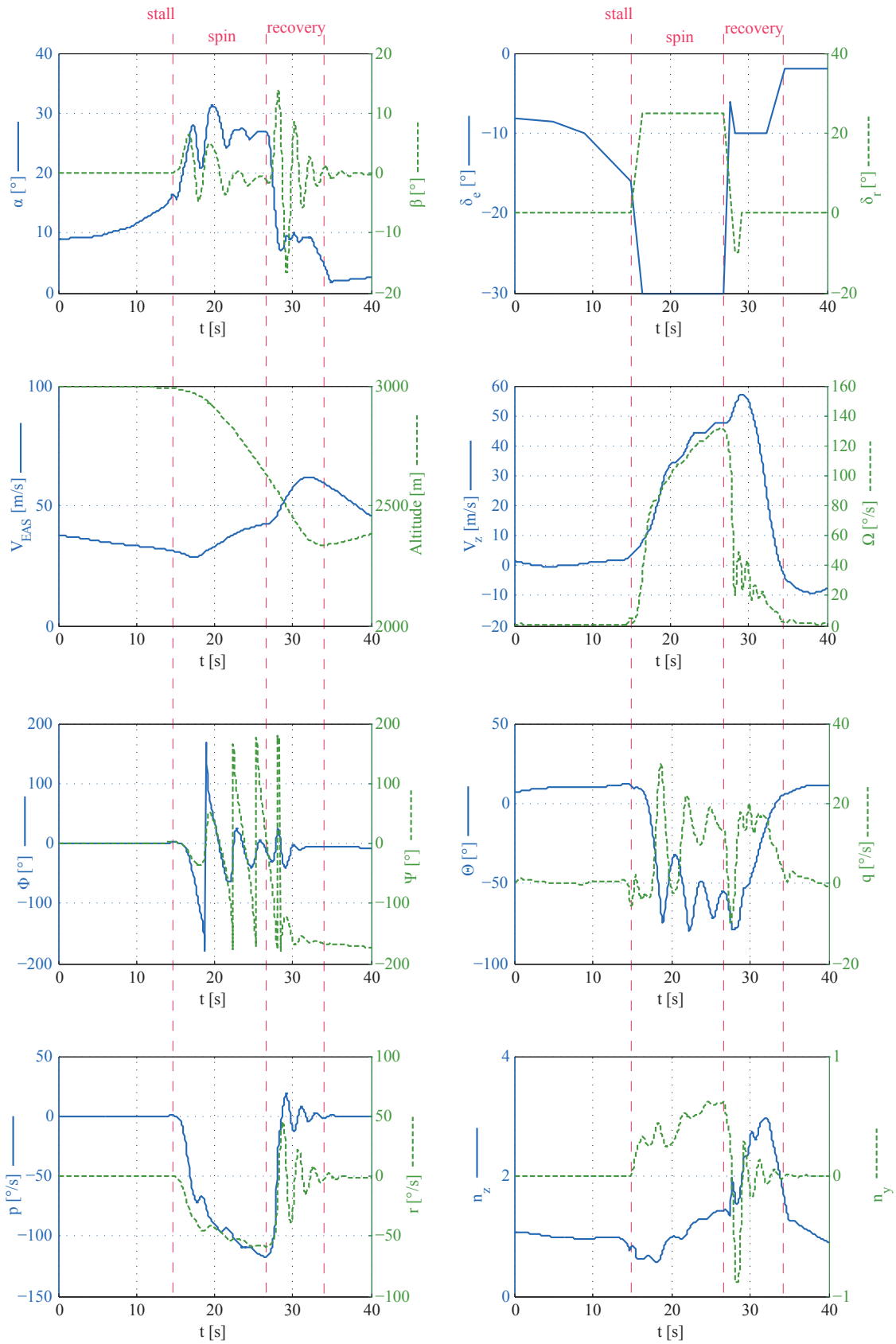


Figure 7.5: Time histories of the simulated developed spin

7.2.3 Fully developed spin

As already seen, after the third turn in the spin, all the variables reach their stabilized value, meaning that all the subsequent turns will bring no changes to the equilibrium point reached. In order to study this condition it was performed the simulation of a six-turns spin. The most significant quantities and the time histories of the simulations are reported in Table 7.3 and Figure 7.6 respectively.

It can be noted how, after the third turn, the oscillations are almost completely absent in all the recorded variables and how their values does not change with time. In Table 7.3 are also shown the stabilized values that characterize the fully developed spin. In particular the angle of attack denotes a steep attitude, the spin rate is quite fast but not out of the ordinary and the average loss of attitude per turn is comparable with other aircrafts certified for spins.

Again the recovery is very prompt and almost identical to the one for the three-turns spin, needing less than one half additional turns in order to stop the rotation.

Throughout the entire maneuver, and especially during the recovery procedure, the limitations for flight speed and load factor were never exceeded.

Table 7.3: Significant values for the fully developed spin simulation

V_s	31 m/s	Stall speed
t_{turn}	3.2 s	Average time for one turn
$t_{\text{turn,stab}}$	2.6 s	Stabilized time for one turn
Δz_{turn}	125 m	Average loss of altitude per turn
$\Delta z_{\text{turn,stab}}$	129 m	Stabilized loss of altitude per turn
Δz_{tot}	1020 m	Total loss of altitude
$\Delta\Psi_{\text{rec}}$	174°	Additional rotation for recovery
α_{mean}	26.5°	Mean value of angle of attack
α_{osc}	~0°	Oscillatory value of angle of attack
β_{mean}	-1°	Mean value of angle of sideslip
β_{osc}	~0°	Oscillatory value of angle of sideslip
p_{stab}	-120°/s	Stabilized value of roll rate
p_{osc}	±0.5°/s	Oscillatory value of roll rate
q_{stab}	+16.5°/s	Stabilized value of pitch rate
q_{osc}	±1°/s	Oscillatory value of pitch rate
r_{stab}	-61°/s	Stabilized value of yaw rate
r_{osc}	~0°/s	Oscillatory value of yaw rate
Ω_{stab}	137°/s	Stabilized value of spin rate
$n_z \text{ max}$	2.95	Maximum load factor during recovery
$V_{\text{EAS max}}$	62 m/s	Maximum flight speed during recovery

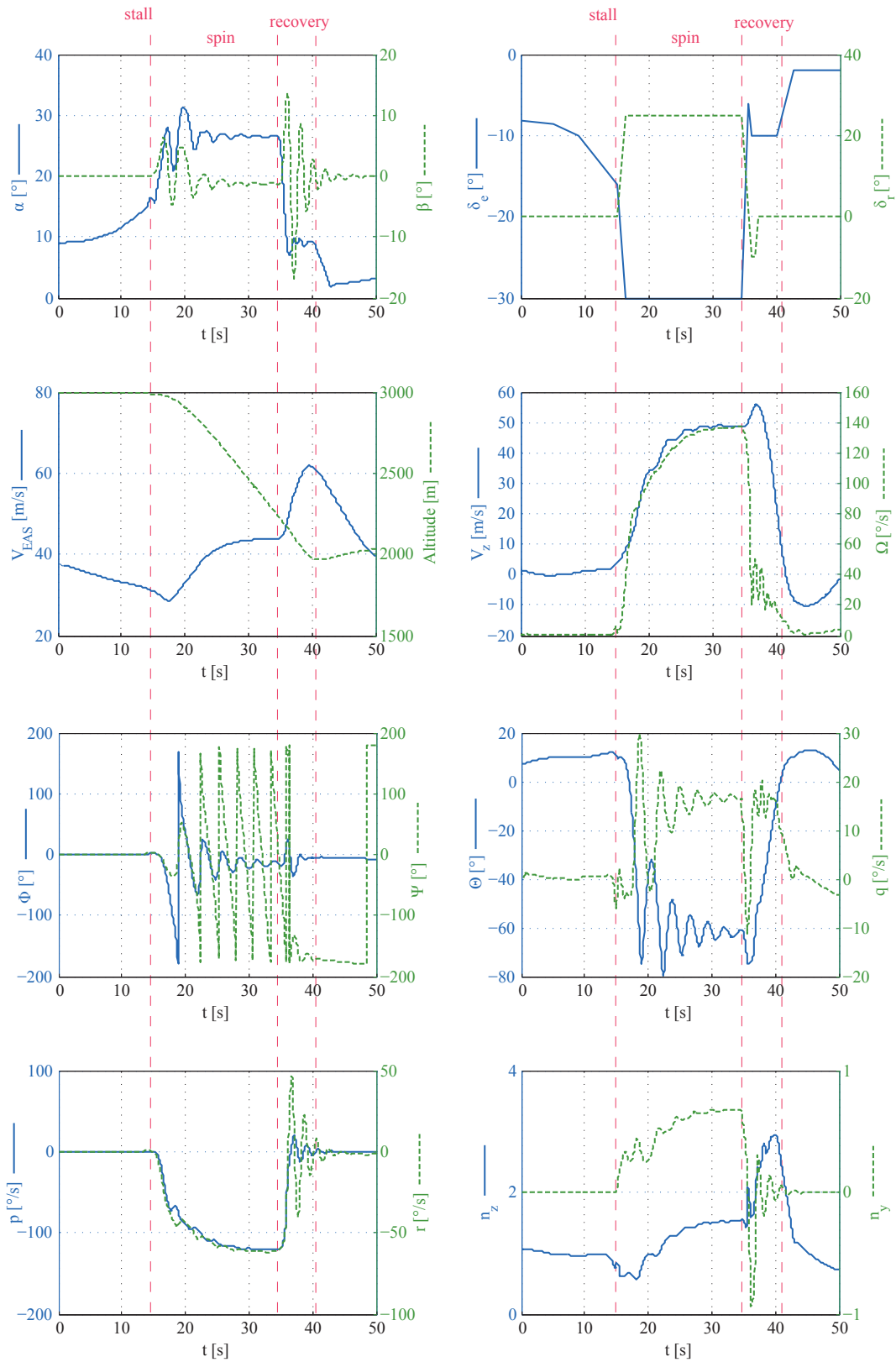


Figure 7.6: Time histories of the simulated fully developed spin

7.3 Recovery procedures

In this section will be presented the study of the most common spin recovery procedure performed in order to determine the optimal maneuver for the aircraft under study. It is in fact well known [6] that different configurations and different weight distributions on the aircraft would require different recovery procedures to achieve the optimal performance.

The recovery maneuvers that were simulated are described in Reference [23] and will be analyzed in the following paragraphs.

The most significant parameters that were considered in order to assess the recovery performance are mainly the time needed to arrest the rotation after the initial recovery input, the additional number of turns and the loss of altitude. Other important parameters are the load factor and the maximum speed, which should never exceed their limit value.

For all the simulations, the initial conditions were of fully developed spin, meaning that the first control inputs for recovery were applied after the completion of the sixth turn in the spin.

7.3.1 Standard recovery

The most common of the recovery procedures, denominated NASA Standard, requires the pilot to deflect the rudder fully against the spin while maintaining the elevator fully up. When the rotation is stopped the rudder is centralized and the elevator eased towards the neutral position. The reason why the elevator should be maintained deflected until the rotation is stopped is because for some tail configurations the neutralization of the elevator would shield a larger part of the rudder making it less effective in the counteraction of the spin. However, for the aircraft under study, the tail configuration is such that this effect would not occur.

Since from previous simulations became apparent that the rotation is arrested very quickly it was considered unnecessary to fully deflect the rudder against the spin, instead only 10° of deflection is applied.

The results of the simulation of the NASA Standard recovery are presented in Table 7.4 and Figure 7.7. The time, loss of altitude and over-rotation are all very contained making this maneuver suitable for a recovery compliant with certification requirements.

Table 7.4: Significant values for the Standard recovery procedure

t_{stop}	2.1 s	Time needed to stop rotation
$\Delta\Psi_{\text{rec}}$	192°	Additional rotation for recovery
Δz_{rec}	295 m	Loss of altitude for recovery
$n_z \text{ max}$	2.75	Maximum load factor during recovery
$V_{\text{EAS max}}$	60 m/s	Maximum flight speed during recovery

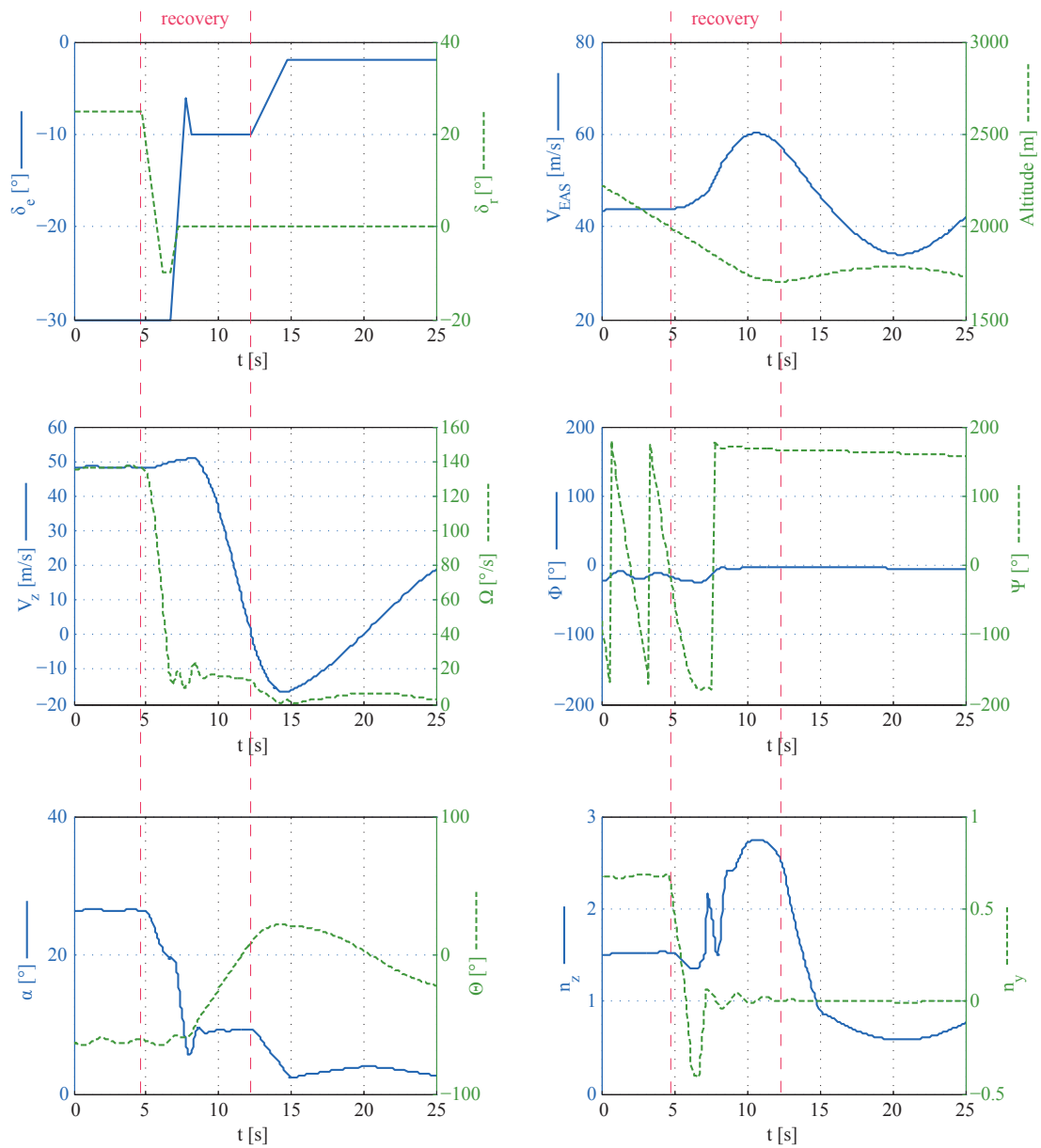


Figure 7.7: Time histories of the Standard recovery procedure

7.3.2 Modified recovery

The second recovery maneuver that was simulated is denominated NASA Modified and is an alteration of the Standard maneuver. It requires the pilot to deflect the rudder fully against the spin as before, and simultaneously neutralize the elevator. When the rotation is stopped the rudder is centralized.

Since the elevator does not shield part of the rudder, this maneuver should be better suited for the aircraft under study. Again in the simulation the rudder is deflected only 10° against the spin.

In Table 7.5 and Figure 7.8 are presented the results obtained from the simulation of the NASA Modified recovery procedure. In comparison with the Standard procedure, the time to stop the rotation is lower, the altitude lost is smaller as well as the over-rotation, making the Modified maneuver achieve an overall better recovery performance.

The most probable cause for the better results of the Modified maneuver with respect to the Standard one is the fact that, as the elevator is neutralized, the angle of attack is quickly reduced allowing a larger portion of the rudder to be exposed to the free stream of air making it more effective in the stopping of the rotation. In fact by comparing the time histories of the angle of attack for the two maneuvers it can be seen how in the first case it remains above 20° before the rotation is arrested, while in the second case it quickly drops below 10° .

Table 7.5: Significant values for the Modified recovery procedure

t_{stop}	1.5 s	Time needed to stop rotation
$\Delta\Psi_{\text{rec}}$	174°	Additional rotation for recovery
Δz_{rec}	265 m	Loss of altitude for recovery
$n_{z \text{ max}}$	2.94	Maximum load factor during recovery
$V_{\text{EAS max}}$	62 m/s	Maximum flight speed during recovery

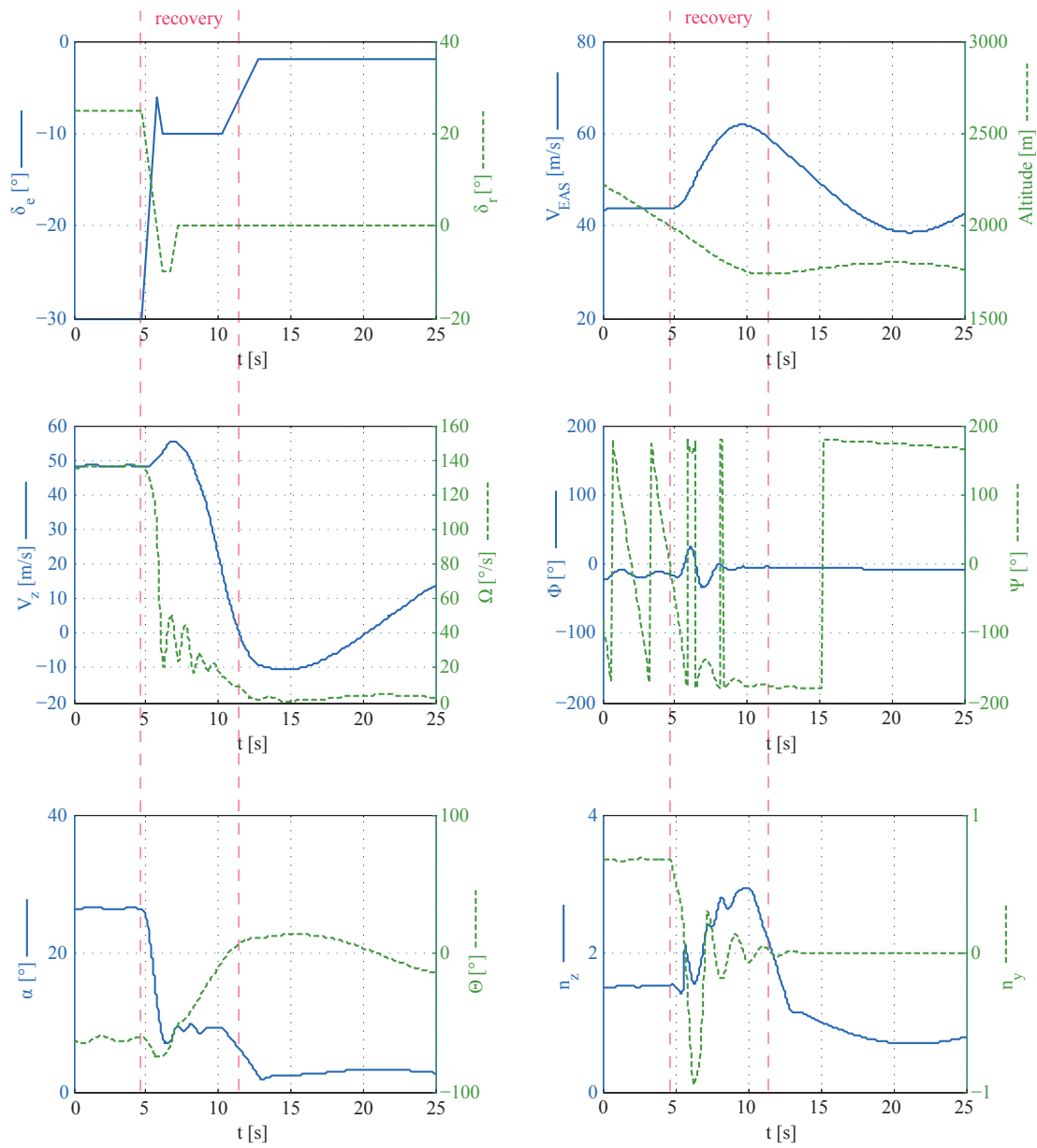


Figure 7.8: Time histories of the Modified recovery procedure

7.3.3 Neutral recovery

The last of the recovery procedures that was analyzed is denominated NASA Neutral. As the name implies it simply requires the simultaneous neutralization of all the controls until the rotation is stopped. The benefit of this maneuver is in its simplicity making it suited for difficult situations. The spin maneuver in fact can be very disorientating for the pilot, which in some cases can have difficulties in the determination of the direction of rotation (especially in inadvertent spins) in order to apply the correct recovery procedure. However not every aircraft is able to recover from a spin by simple centralization of all the controls and for this reason it is necessary to properly test this procedure.

The results of the simulation are shown in Table 7.6 and Figure 7.9 for the NASA Neutral recovery maneuver. It can be seen that the rotation is again quickly arrested, needing even less time and altitude than the NASA Standard procedure. Without the deflection of the rudder against the spin the over-rotation is greater but still very contained making this maneuver compliant with the certification requirements.

Even if the overall performance not optimal, this maneuver can be applied to be able to recover from inadvertent spins as described before without losing excessive altitude.

Table 7.6: Significant values for the Neutral recovery procedure

t_{stop}	1.8 s	Time needed to stop rotation
$\Delta\Psi_{\text{rec}}$	208°	Additional rotation for recovery
Δz_{rec}	271 m	Loss of altitude for recovery
$n_z \text{ max}$	2.97	Maximum load factor during recovery
$V_{\text{EAS max}}$	62 m/s	Maximum flight speed during recovery

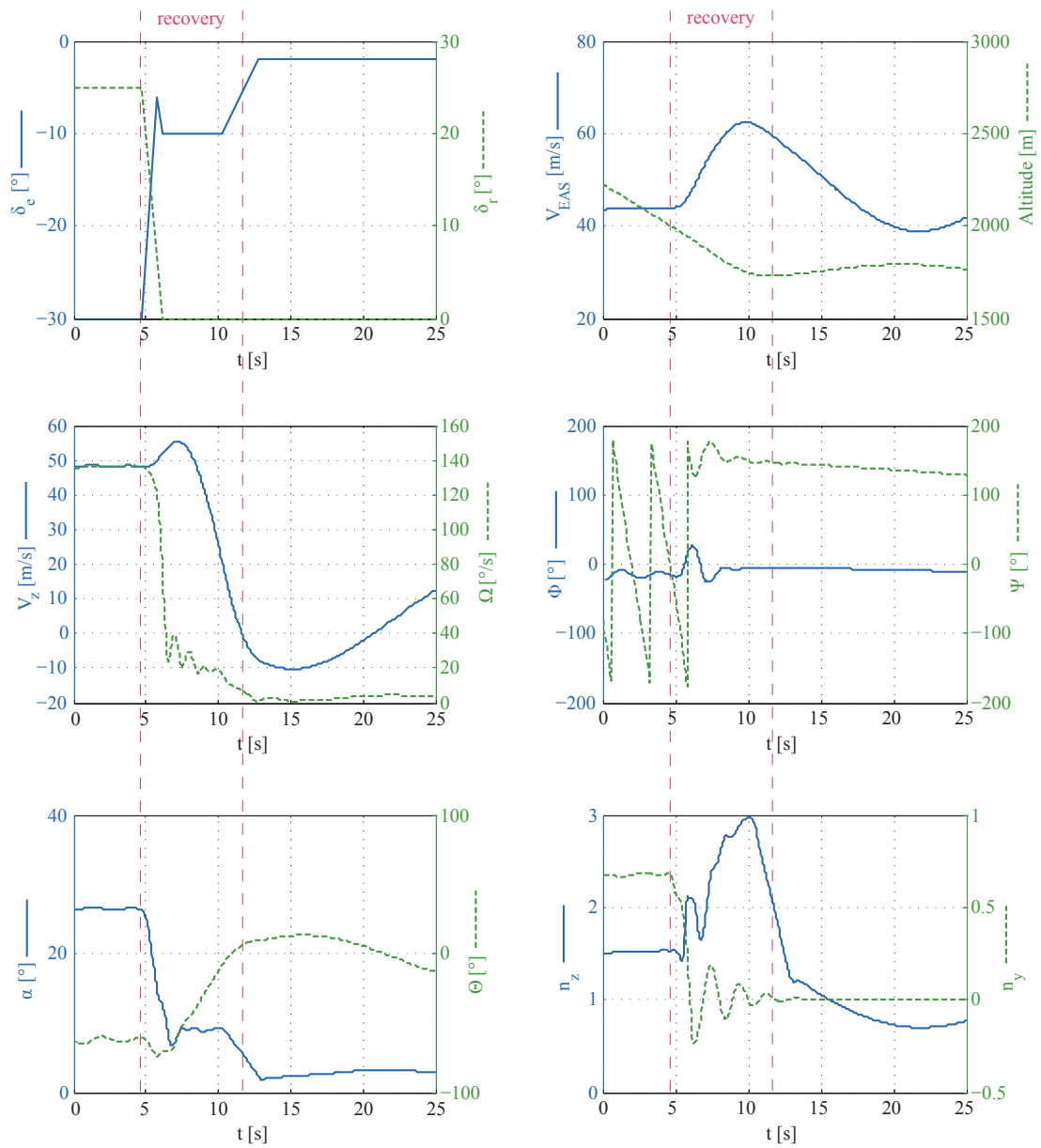


Figure 7.9: Time histories of the Neutral recovery procedure

7.4 Other parameters

In order to be able to study the spin maneuver in greater detail it was considered the possibility to perform additional simulations by changing some of the parameters that most affect the spinning characteristics of the aircraft [6]. In particular they were separately considered the effects of the increase in weight of the aircraft, the increase in yawing moment of inertia and the effect of a lower altitude.

To be able to better appreciate the consequences of such modifications, in the tables that summarize the most significant quantities of the entire maneuver, it was added a column with the relative percent difference with respect to the fully developed spin maneuver for the unaltered configuration, presented in a previous paragraph.

The maneuvers that were simulated are the fully developed spins, from stall and spin entry to the recovery procedure after the completion of the sixth turn.

7.4.1 Increased weight

The first modification to the basic aircraft configuration that was considered is the increase in weight of the aircraft by 20%, bringing it to 850 kg, while maintaining all the other inertial characteristics and initial condition unaltered. This modification has also been considered by the company that produces the aircraft in order to be able to carry a greater payload.

The results of the simulation are presented in Table 7.7 and Figure 7.10. From the comparison with the basic configuration it can be noted that some of the variables present a significant change while others remain practically the same.

As expected, due to the increase in weight the stall speed had also increased accordingly since there were no modifications to the aerodynamic characteristics.

The rate of rotation has increased as well, as indicated by the average time for one turn and by the stabilized spin rate.

There is a slight decrease in the average loss of altitude per turn, while the total altitude lost is slightly greater, which indicates that the recovery procedure required more altitude before regaining level flight.

There is almost no change to the angle of attack and only a minor change to the angle of sideslip, that even if presents a big relative difference (+50%) it only changed by 0.5°.

During the recovery phase the over-rotation and the maximum flight speed are increased while the maximum load factor remained unchanged.

Table 7.7: Significant values for the spin maneuver with increased weight

Symbol	Value	$\Delta\%$	Description
V_s	34 m/s	+9.7%	Stall speed
t_{turn}	3.0 s	-6.2%	Average time for one turn
$t_{\text{turn,stab}}$	2.4 s	-7.7%	Stabilized time for one turn
Δz_{turn}	120 m	-4.0%	Average loss of altitude per turn
$\Delta z_{\text{turn,stab}}$	128 m	-0.8%	Stabilized loss of altitude per turn
Δz_{tot}	1043 m	+2.2%	Total loss of altitude
$\Delta\Psi_{\text{rec}}$	194°	+11.5%	Additional rotation for recovery
α_{mean}	26.5°	~0%	Mean value of angle of attack
β_{mean}	-1.5°	+50%	Mean value of angle of sideslip
p_{stab}	-132°/s	+10%	Stabilized value of roll rate
q_{stab}	+16.6°/s	+0.6%	Stabilized value of pitch rate
r_{stab}	-67°/s	+10%	Stabilized value of yaw rate
Ω_{stab}	149°/s	+8.0%	Stabilized value of spin rate
$n_z \text{ max}$	2.95	~0%	Maximum load factor during recovery
$V_{\text{EAS max}}$	67 m/s	+8.0%	Maximum flight speed during recovery

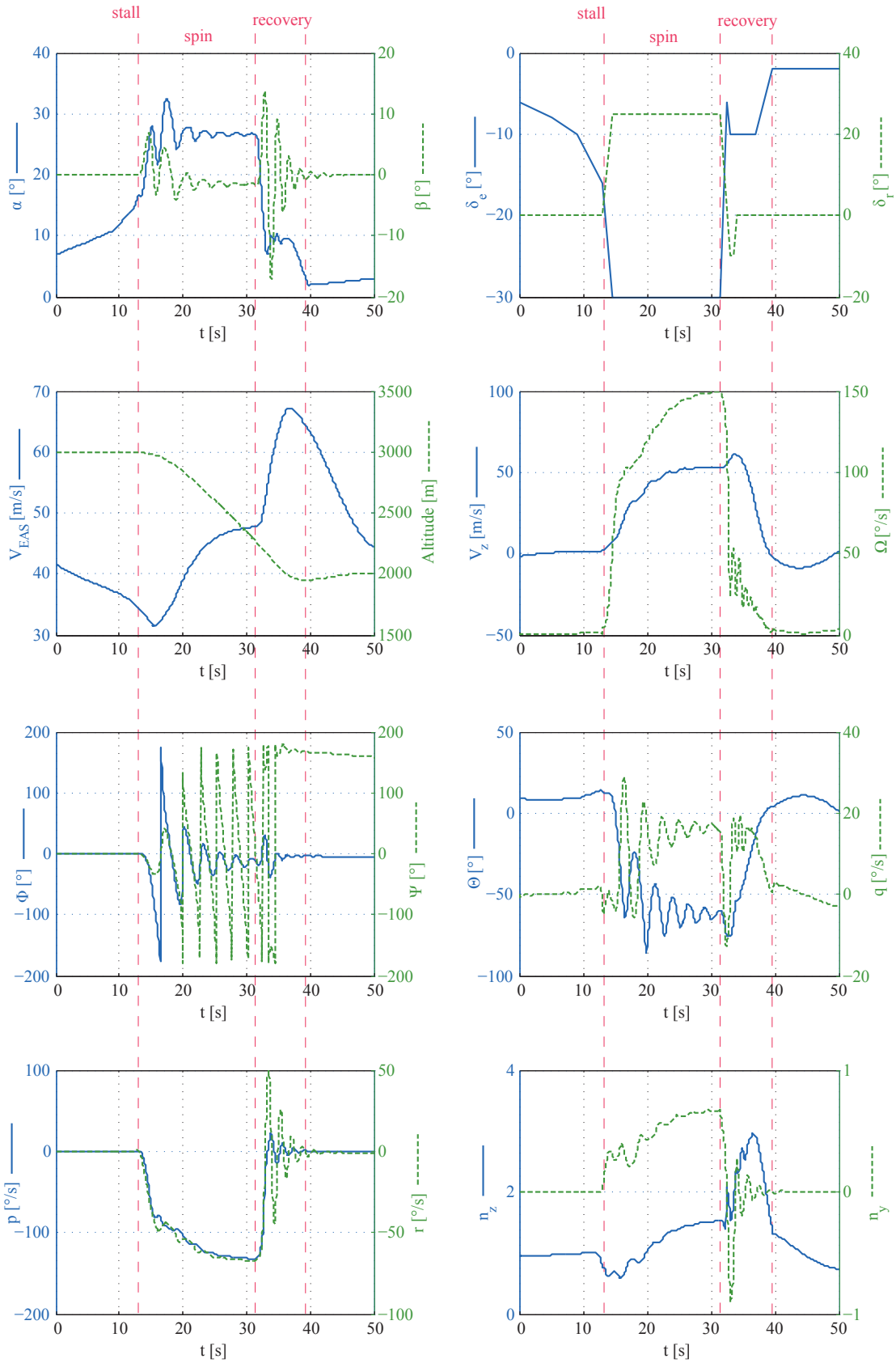


Figure 7.10: Time histories of the spin maneuver with increased weight

7.4.2 Increased yawing moment of inertia

The second modification to the basic load configuration that was tested is the increase of yawing moment of inertia by 20% while maintaining the weight and all the other initial conditions unaltered.

In Figure 7.11 are reported the time histories of the simulation and in Table 7.8 are presented the most significant values and the relative difference with respect to the basic configuration.

As expected, as a result of the increase of the yawing moment of inertia the overall spin rate decreased. The altitude loss increased as well, while the additional rotation for recovery decreased slightly.

There is only a minor change to the angle of attack and angle of sideslip, which both increased slightly.

The stall speed and the maximum speed remained both unchanged.

Table 7.8: Significant values for the spin maneuver with increased yawing moment of inertia

Symbol	Value	$\Delta\%$	Description
V_s	31 m/s	$\sim 0\%$	Stall speed
t_{turn}	3.5 s	+9.4%	Average time for one turn
$t_{\text{turn,stab}}$	2.9 s	+11.5%	Stabilized time for one turn
Δz_{turn}	138 m	+10.4%	Average loss of altitude per turn
$\Delta z_{\text{turn,stab}}$	141 m	+8.5%	Stabilized loss of altitude per turn
Δz_{tot}	1093 m	+7.1%	Total loss of altitude
$\Delta\Psi_{\text{rec}}$	164°	-5.7%	Additional rotation for recovery
α_{mean}	27.0°	+1.8%	Mean value of angle of attack
β_{mean}	-1.9°	+90%	Mean value of angle of sideslip
p_{stab}	-107°/s	-10.8%	Stabilized value of roll rate
q_{stab}	+17.5°/s	+6.0%	Stabilized value of pitch rate
r_{stab}	-56°/s	-8.2%	Stabilized value of yaw rate
Ω_{stab}	123°/s	-10.2%	Stabilized value of spin rate
$n_{z \text{ max}}$	2.89	-2.0%	Maximum load factor during recovery
$V_{\text{EAS max}}$	62 m/s	$\sim 0\%$	Maximum flight speed during recovery

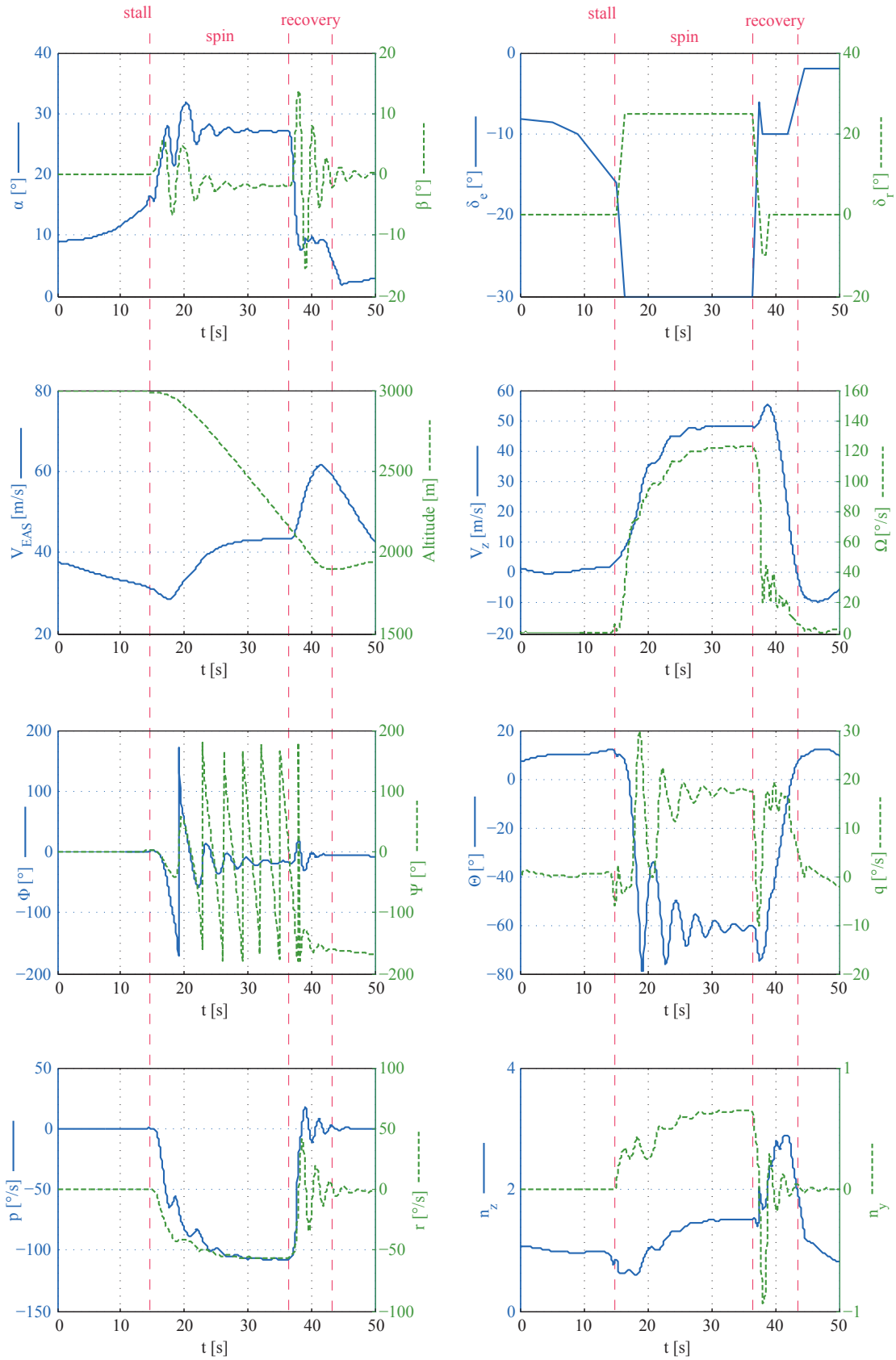


Figure 7.11: Time histories of the spin maneuver with increased yawing moment of inertia

7.4.3 Lower altitude

Another change in the flight conditions that was considered relevant for the spinning characteristics is the altitude. In particular it was modified the initial altitude from 3000 m to 2000 m (~6500 ft.).

The results of the simulation are shown in Table 7.9 and Figure 7.12.

It can be noted how the lower starting altitude did not affect particularly the overall spinning characteristics. The only significant changes are the smaller altitude lost and the smaller over-rotation for the recovery, both due to the increased air density at lower altitude.

Table 7.9: Significant values for the spin maneuver at lower altitude

Symbol	Value	$\Delta\%$	Description
V_s	31 m/s	~0%	Stall speed
t_{turn}	3.2 s	~0%	Average time for one turn
$t_{\text{turn,stab}}$	2.6 s	~0%	Stabilized time for one turn
Δz_{turn}	120 m	-4.0%	Average loss of altitude per turn
$\Delta z_{\text{turn,stab}}$	123 m	-4.6%	Stabilized loss of altitude per turn
Δz_{tot}	963 m	-5.6%	Total loss of altitude
$\Delta\Psi_{\text{rec}}$	162°	-6.8%	Additional rotation for recovery
α_{mean}	26.3°	-0.7%	Mean value of angle of attack
β_{mean}	-0.8°	-20%	Mean value of angle of sideslip
p_{stab}	-120°/s	~0%	Stabilized value of roll rate
q_{stab}	+16.0°/s	-3.0%	Stabilized value of pitch rate
r_{stab}	-61°/s	~0%	Stabilized value of yaw rate
Ω_{stab}	136°/s	-0.7%	Stabilized value of spin rate
$n_z \text{ max}$	2.93	-0.7%	Maximum load factor during recovery
$V_{\text{EAS max}}$	62 m/s	~0%	Maximum flight speed during recovery

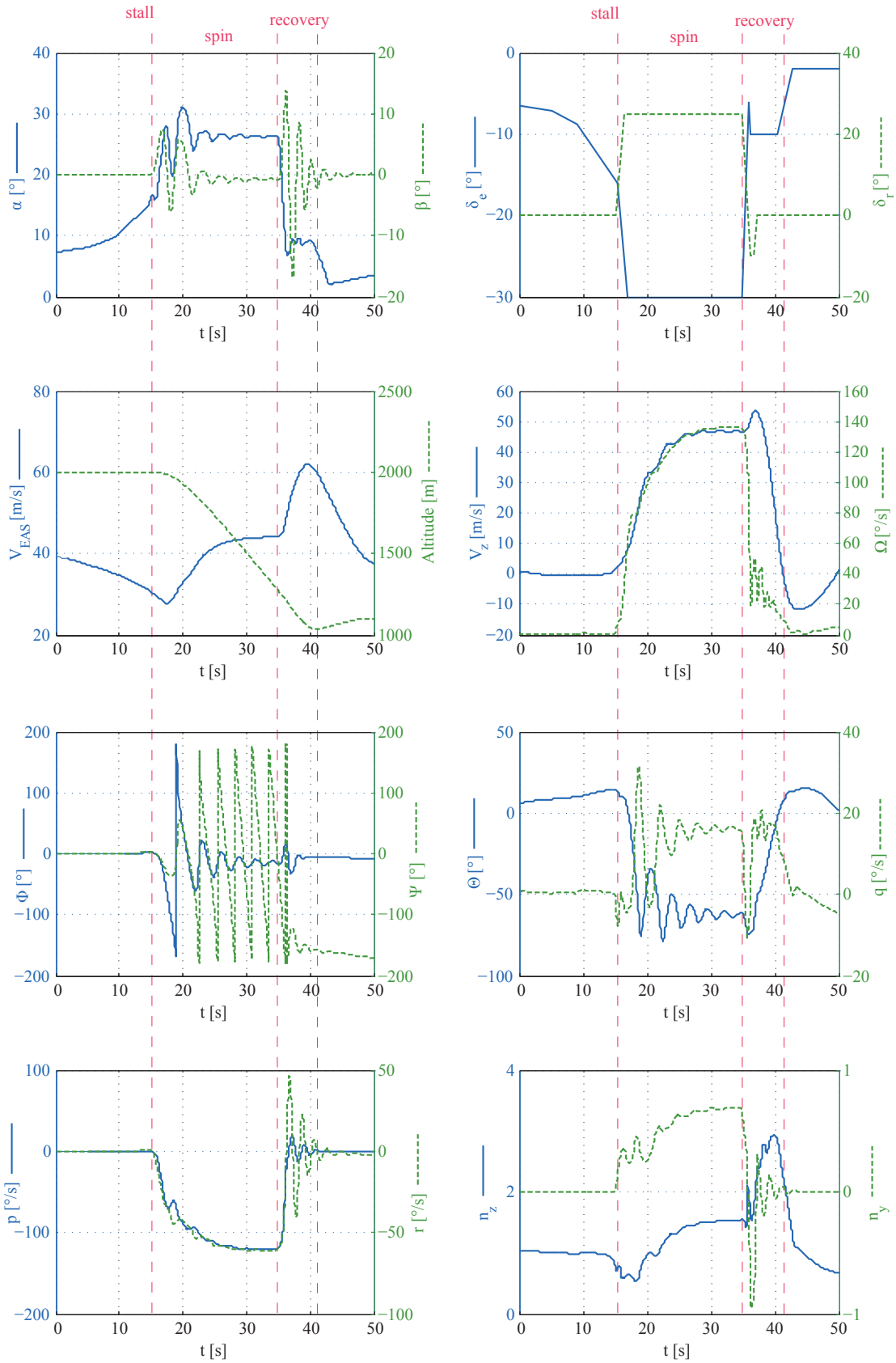


Figure 7.12: Time histories of the spin maneuver at lower altitude

8 Conclusions

For many years now the computer simulations have been applied in the study of the spin characteristics of new aircraft, especially for military application where the behaviors in the post-stall region are of great importance and can be rather difficult to predict. Conventionally the aerodynamic properties needed to perform such simulations are determined in wind-tunnel tests, which can be extremely expensive and time consuming, for the large amount of data needed to be gathered and analyzed.

On the other hand, in the previous chapters is presented a method that can be considered viable for the estimation of the aerodynamic coefficients up to high angle of attack and for the prediction of the spinning characteristics of an aircraft without the need for wind tunnel tests. In fact it mainly relies upon the data collected during conventional flight tests performed on the prototype aircraft and the incipient spin tests, to be able to predict its behavior in a stabilized spin and its recovery performance.

The comparison with the dynamically scaled model showed encouraging results and gave prove of the good accuracy of the simulated predictions. However the oscillatory behavior exhibited by the scaled model, which is not present in the simulation outputs, underlines one limitation of the analytical model that was developed. In fact the inability to reach a stable equilibrium in a spin, which results in periodic oscillations, is almost certainly caused by large non-linearities of the yawing-moment and rolling-moment coefficients due to the overall angular rotation characteristic of the spin. These non-linearities are almost impossible to predict without rotary balance measurements in wind tunnel tests, and for this reason were not implemented during the development of the analytical spin model.

Given this limitation however, it is believed that the oscillatory nature of a spin would not affect negatively the recovery maneuver for two main reasons: the overall balance between inertial and aerodynamic forces and moments is less stable and more prone to be broken by the recovery control actions; secondly an oscillatory behavior means that the angle of attack would periodically be at low values, at which point the rudder would have very good control effectiveness needed to stop the rotation.

8.1 Discussion of the results of the simulations

The simulations of the spin up to six turns showed a very promising behavior. All the values of angle of attack and angular rates are typical of a steep spin, with no noticeable signs of the possibility to develop into a flat spin.

After the third turn the condition of developed spin is reached, in which all the simulated quantities maintain a stable value. In this condition the altitude loss has a moderate value of about 129 m (~420 ft) for each additional turn.

The recovery after the sixth turn is very prompt, needing less than one-half additional turn to completely stop the rotation. Throughout the entire maneuver, the flight speed and the load factor remain well below their maximum limits, peaking respectively at 62 m/s and +3 during the final pull-up.

The altitude lost, from the spin entry to the completion of the sixth turn and the recovery procedure is 1025 m (~3360 ft).

The overall spin performance as a result of the simulations can be considered very good, and assuming it to be a good representation the behavior of the aircraft, all the spinning requirement needed for the certification would be met.

The simulation of the stall characteristics did not show any tendency to develop lateral or directional instability even after an accelerated turning stall. As a result, in the simulated conditions, it would be very unlikely for the aircraft to enter in a regime of autorotation, which could lead to an inadvertent spin.

In the spin simulations with increasing number of turns it can be noted how, after the first turn characterized by distinct oscillations, all the variables tend quickly towards a stabilized value, which is reached after the third turn, when the spin can be considered fully developed. In this phase there is no significant change in the spinning characteristics from one turn to the next and for this reason also the recovery performance would be mostly unchanged from the third rotation and on.

The three different recovery procedures tested would all be suitable and compliant with the CS-23 “Aerobatic” certification requirements, which denotes how the aircraft has no difficulty to recover from a fully developed spin. With the optimal recovery procedure the rotation is arrested in 1.5s and the total altitude lost needed to complete the maneuver is 265 m (~870 ft). However also the neutralization of all the controls results in a prompt spin recovery, which would be extremely helpful in case of pilot disorientation.

The simulations at different initial conditions did not show unexpected changes in the overall spin characteristics and recovery performance. The angle of attack remained mostly the same as the basic configuration, demonstrating that the spin mode achieved is very stable and has no tendency to develop into a flat attitude.

References

- [1] Pamadi, B.N., *Performance, stability, dynamics and control of airplanes*, American Institute of Aeronautics and Astronautics, 1998.
- [2] Abzug, M.J., and Larrabee, E.E., *Airplane stability and control*, 2nd edition, Cambridge University Press, 2002.
- [3] Calcara, M., *Elementi di dinamica del velivolo*, CUEN, 1988.
- [4] Martin, C., *The spinning of aircraft – A discussion of spin prediction techniques including a chronological bibliography*, Department of Defence, Aeronautical Research Laboratory, 1988.
- [5] Brinkworth, B.J., *On early history of spinning and spin research in the UK*, Journal of Aeronautical History, 2014.
- [6] Bowman, James S. Jr., *Summary of spin technology as related to light General-Aviation airplanes*, NASA Technical Note D-6575, 1971.
- [7] Kerr, T.H., *A criterion for the prediction of the recovery characteristics of spinning aircraft*, Royal Aircraft Establishment, Technical Note Aero 2251, 1953.
- [8] Stinton, D., *The design of the aeroplane*, BSP Professional Books, 1983.
- [9] Seidman, O., and Donlan, C.J., *An approximate spin design criterion for monoplanes*, NACA Technical Note No. 711, 1939.
- [10] Gale, L.J., and Jones, I.P., *Effects of antispin fillets and dorsal fins on the spin and recovery characteristics of airplane as determined from free-spinning-tunnel tests*, NACA Technical Note No. 1779, 1948.
- [11] Neihouse, A.I., Lichtenstein, J.H., and Pepoon, P.W., *Tail-design requirements for satisfactory spin recovery*, NACA Technical Note No. 1045, 1946.
- [12] Roskam, J., *Airplane design: Part VI, Preliminary calculations of aerodynamic, thrust and power characteristics*, Roskam Aviation and Engineering Corporation, 1987.
- [13] Etkin, B., *Dynamics of flight, stability and control*, Third edition, John Wiley and sons, Inc., 1959.
- [14] Guglieri, G., *Stabilità, controllo e qualità di volo*, Celid, 2008.
- [15] Adams, W.M. Jr., *Analytic prediction of airplane equilibrium spin characteristics*, NASA Technical Note D-6926, 1972.
- [16] Anglin, L.A., *Analytical study of effects of product of inertia on airplane spin entries, developed spins and spin recoveries*, NASA Technical Note D-2754, 1965.
- [17] Hill, S.D., and Martin, C.A., *A flight dynamic model of aircraft spinning*, Department of Defence, Aeronautical Research Laboratory, 1990.

- [18] Langham, T.F., *Correlation of experimental and theoretical steady-state spinning motion for a current fighter airplane using rotation-balance aerodynamic data*, ARO, Inc., AEDC-TR-77-126, 1978.
- [19] Various authors, *Stall/Spin Problems of Military Aircraft*, AGARD-CP-199, 1976.
- [20] Bazzocchi, E., *Stall behaviour and spin estimation method by use of rotating balance measurements*, Aermacchi, 1975.
- [21] Mason, V.H., *High angle of attack aerodynamics*, 2006.
- [22] Holleman, E.C., *Summary of flight tests to determine the spin and controllability characteristics of a remotely piloted, large-scale (3/8) fighter airplane*, NASA Technical Note D-8052, 1976.
- [23] Young, J.W., *Optimal and suboptimal control technique for aircraft spin recovery*, NASA Technical Note D-7714, 1974.
- [24] EASA, *Certification specifications and acceptable means of compliance for Normal, Utility, Aerobatic, and Commuter category airplanes, CS-23, Amd. 4*, 2015.
- [25] EASA, *Certification specifications for very light aeroplanes, CS-VLA, Amd. 1*, 2009.